DEPARTMENT OF PHYSICS

TECHNISCHE UNIVERSITÄT MÜNCHEN

Master's Thesis

Characterization of the Detector Response to Electrons and Test of a New Entrance Window Technology of Silicon Drift Detectors for the TRISTAN Project

Charakterisierung der Detektorantwort auf Elektronen und Test einer Neuen Eintrittsfenstertechnologie für Silizium Drift Detektoren für das TRISTAN Projekt

Author:	Manuel Lebert
Primary reviewer:	Prof. Dr. Susanne Mertens
Secondary reviewer:	Prof. Dr. Stefan Schönert
Supervisor:	Tim Brunst
Submission Date:	02.12.2019

Max-Planck-Institut für Physik
(Werner-Heisenberg-Institut)

Abstract

Neutrinos are the most abundant particles with mass in the universe and the lightest ones in the standard model of particle physics. One way to explain the lightness of neutrinos is the introduction of right-handed neutrinos. These would not interact at all and are hence called sterile neutrinos. These theoretical particles would only be a minimal extension of the standard model. If the corresponding additional neutrino mass eigenstate would have a mass in the keV range, they could potentially explain dark matter. A special feature of this type of dark matter is that is could be rather warm, which in turn may solve some tensions in the description of small-scale structures in the universe. An imprint of keV-sterile neutrinos could be observable in the spectrum of β-decay. The additional heavy mass eigenstate would lead to a very small kink-like structure in the spectrum. The TRISTAN project aims to upgrade the KATRIN experiment with an multi-pixel detector system. The prerequisites of this novel detector system are to: 1) handle high rate, 2) provide an excellent energy resolution, 3) to allow for a precise calibration and modeling of the detector response to electrons. An ideal technology for such applications are silicon drift detector. With this new detector KATRIN could be sensitive to those new particles.

The first objective of this thesis was the characterization of the entrance windows of the first seven-pixel silicon drift detector TRISTAN prototypes with conversion electrons from the metastable ^{83m}Kr decay. The second objective of this thesis was the investigation of a novel technique based on molecular beam epitaxy to produce silicon drift detectors with ultra-thin entrance windows.

The entrance window of a silicon drift detector alters the measured energy of incoming electrons and the shape of an electron peak. Therefore, this window has to be as thin as possible. Two detectors with different ion implanted entrance windows were characterized. To this end monoenergetic conversion electrons from ^{83m}Kr decay were used. By measuring the position of the electron peaks at different incident angles of the electrons, the entrance window thickness of the detector can be determined largely independent of the energy losses in the source itself.

Finally, the observerd shift of the electron's peak position can be related to an effective dead layer via Monte-Carlo simulations. The results of energy shift and dead layer are then compared to previous characterizations. The shifts of this work and the previous one's are compatible.

For the investigations of detectors fabricated with the novel molecular beam epitaxy, at first the leakage current of several hundred pin-diodes was evaluated. In general, epitaxy pin-diodes have a higher leakage current and therefore a higher failure rate compared to ion implanted ones. In a second step, four representative diodes were chosen and the efficiencies of those were measured with the help of an electron microscope. Of the chosen diodes two were produced using molecular beam epitaxy and two were produced using standard ion implantation techniques. At incoming electron energies above 10 keV hardly any difference is visible. In the energy range between 1 to 2 keV the efficiencies of epitaxy diodes are above 70 %, while the standard ion implantation technology show only efficiencies of 30 %. Hence, as a major result of this work, it could be shown that the epitaxy technique is superior over implantation for diodes. Based on Monte-Carlo simulations the observed detection efficiencies can again be related to a dead layer. It is found that the entrance window of the pin-diodes produced with the novel epitaxial technique can be described with a thin, approximately 5 nm thick, dead volume. The standard detectors, in contrast, are better described with thick transition layers of up to several hundred nm.

Contents

1. Introduction

The neutrino is the most abundant particle in the universe. It was proposed in 1930 by Wolfgang Pauli to explain the continuous β-spectrum. Roughly twenty-five years later it was discovered. They are the only particles in the Standard Model of particle physics, that interact only via the weak force. Therefore, the direct investigation of their properties is extremely difficult. In this chapter a short overview of the currently known properties of the neutrino is given. Afterwards, the hypothetical sterile neutrino is introduced. The cosmological and particle physics observations as motivation for the introduction of a new neutrino are then given. Finally, the KATRIN experiment, measuring the neutrino mass, and its detector upgrade, the TRISTAN, project are described.

1.1. Neutrino Physics

The Neutrino in the Standard Model: The Standard Model (SM) of particle physics describes the fundamental particles and their interaction via the electroweak and strong force, all particles are shown in figure 1.1. The neutrino in this model is a massless particle that comes in three flavors. Neutrinos have no electric charge and therefore, solely interact via the weak force, which couples only to left-handed particles. Thus, a right-handed neutrino would not interact in any way, which makes the neutrino the only particle that exists exclusively with left-handed chirality.

Neutrino Oscillations: Through several experiments it was shown that the neutrino is in fact not massless [6, 18]. This is proven by neutrino oscillation, in which neutrinos change their flavor. The flavor eigenstate of a neutrino $(\nu_e, \nu_\mu, \nu_\tau)$ is not the same as its mass eigenstate (ν_1, ν_2, ν_3). Each flavor is a superposition of the three mass eigenstates. The mixing between the masses for each flavor is described by the Pontecorvo-Maki-Nakagawa-Sakata (PMNS) matrix (see equation (1.1)).

$$\underbrace{\begin{pmatrix}\nu_e\\ \nu_\mu\\ \nu_\tau\end{pmatrix}}_{\text{Flavor Eigenstates}} = \underbrace{\begin{pmatrix}U_{e1} & U_{e2} & U_{e3}\\ U_{\nu 1} & U_{\nu 2} & U_{\nu 3}\\ U_{\tau 1} & U_{\tau 2} & U_{\tau 3}\end{pmatrix}}_{\text{PMNS Matrix}} \underbrace{\begin{pmatrix}\nu_1\\ \nu_2\\ \nu_3\end{pmatrix}}_{\text{Mass Eigenstates}} \tag{1.1}$$

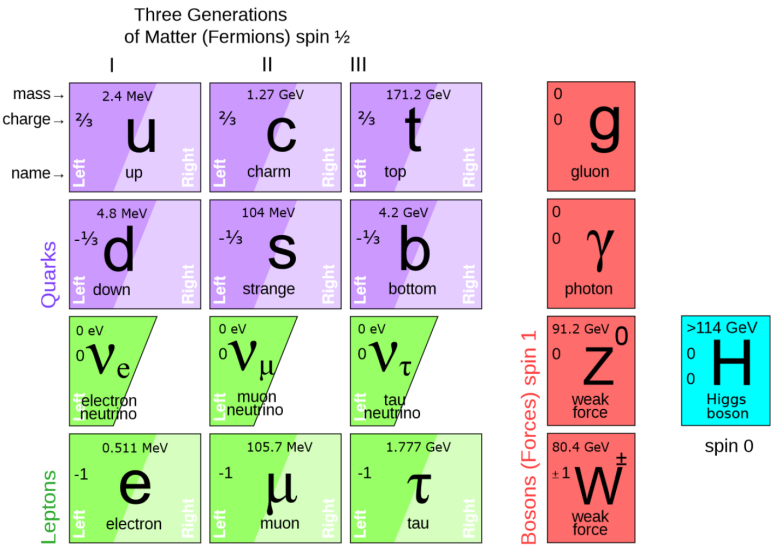

Figure 1.1.: The particles constituting the Standard Model of particle physics. The neutrinos are the only particles that interact exclusively via the weak force and thus are only left-handed. Taken from [19].

The mass eigenstate is the propagation state of neutrinos, which then leads to the mixing of the flavors. The probability to transition between flavor eigenstate i to another flavor eigenstate j is:

$$P_{i\to j} \propto \sin^2\left(\frac{\Delta m_{ij}^2 L}{4E}\right) \tag{1.2}$$

Here, E is the energy of the neutrino and L is the distance from the creation point. The mixing probability is only sensitive to the difference of the squared masses of two different mass states $\Delta m_{ij}^2 = m_i^2 - m_j^2$. If neutrinos were massless, the mass difference Δm_{ij}^2 would be zero and no oscillation would appear. Thus, the existence of neutrino oscillations between all three flavors prove that at least two mass eigenstates are non-zero and the SM is incomplete.

Neutrino Mass: Neutrino oscillations are sensitive to the mass difference of neutrinos. However, they cannot probe the absolute mass scale of neutrinos. For this three methods are currently explored:

The ΛCDM is a cosmological model that describes the evolution of the universe. Because of their vast abundance, neutrinos have an influence on the structure formation in the universe. They have a long free streaming length and thus wash out small scale structures, which influences the formation of large-scale structures (LSS). Therefore, by analyzing the LSS of the current universe and the anisotropies

of the cosmic microwave background an upper limit on the sum of neutrino masses can be determined. This lies between 0.12 and 0.9 eV [4, 15]. However, these limits are extremely model dependent because they differ by which data sample is used and which processes are taken into account during analysis.

The second method is the search for the neutrinoless double β-decay ($0\nu\beta\beta$):

$$2n \rightarrow 2p + 2e^- \tag{1.3}$$

This process is forbidden by lepton number conservation. It is only feasible if neutrinos are Majorana particles, meaning they are their own anti-particles. If this process is observed it would be possible to determine the effective mass of the Majorana neutrinos through the half-life of the decay. The currently best upper limit is 0.2 eV at 90 % C.L. [5].

The third method is by measuring the kinematics of the β-decay. For this, the spectrum of β-decay electrons is measured. The endpoint is lower, corresponding to the mass of the neutrino, than in a massless neutrino case. This has the advantages of well-known physics and it is hardly model dependent. Currently the resolution of such kinematics measurements is not precise enough to resolve the three different mass states. Therefore, a limit on the effective electron anti-neutrino mass is given:

$$m_{\nu e} = \sqrt{\sum_i m_i^2 \left|U_{ei}\right|^2} \tag{1.4}$$

The Karlsruhe Tritium Neutrino (KATRIN) experiment currently set the best upper limit for this effective mass to 1.1 eV at 90 % C.L. [7].

1.2. Sterile Neutrinos

As shown in section 1.1 the neutrino of the Standard Model is the only particle that has exclusively left-handed chirality. Therefore, a minimal, natural extension of the SM is the introduction of right-handed neutrinos, as shown in figure 1.2. These neutrinos would not interact at all, except for their mixing with the left-handed neutrinos. Hence, they are called sterile neutrinos.

Depending on the scale of the corresponding new neutrino mass eigenstate (which are mostly made of the right-handed type), sterile neutrinos could explain the small masses of active neutrinos through the seesaw mechanism ($\mathcal{O}$(MeV)) or would be viable dark matter candidates ($\mathcal{O}$(keV)).

1.2.1. Particle Physics Motivation

For the active neutrinos the mass creation mechanism is unknown. Mass creation via interaction with the Higgs field requires changing the chirality, therefore it is

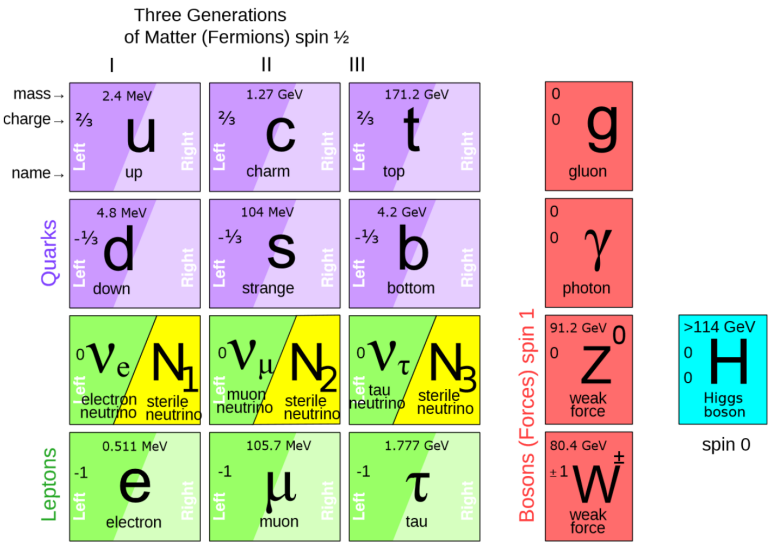

Figure 1.2.: Right-handed neutrinos are a minimal extension of the Standard Model of particle physics. These particles would not interact at all, except for their mixing to the left-handed neutrinos. Thus, they are called sterile neutrinos. Taken from [19].

not possible for only left-handed active neutrinos. By introducing a right-handed neutrino, the Higgs mechanism would be possible for neutrinos. To not exceed the current bounds on the neutrino mass the Yukawa coupling needed for the neutrinos is in the order of 10^{-12} [3]. This is five orders of magnitude smaller then the coupling for an electron.

Another way of introducing small neutrino masses is by the seesaw mechanism. For this a right-handed, Majorana neutrino with mass m_r is introduced. This can be done without the Higgs mechanism. Additionally, a Dirac mass m_D is assumed. Then the mass of one neutrino generation in matrix notation is:

$$M = \begin{pmatrix} 0 & m_D \\ m_D & m_r \end{pmatrix} \rightarrow m_1 = m_r,\ m_2 = \frac{-m_D^2}{m_r} \tag{1.5}$$

This leads to the eigenvalues m_1 and m_2. Assuming $m_r \gg m_D$ results in a heavy, right-handed Majorana state and a light active state [3].

1.2.2. Cosmological Motivation

Current observations of the composition of the universe show that only about 5 % consists of baryonic matter, 26 % of dark matter (DM) and 69 % of dark energy [2]. Not much is known about dark energy, but it is believed to be the reason of the

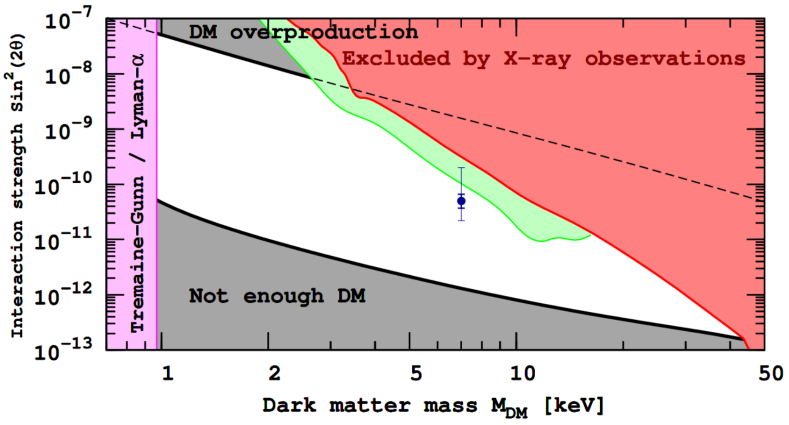

Figure 1.3.: Cosmological constraints on sterile neutrinos. The white space is the allowed parameter space for sterile neutrinos if they make up 100 % of dark matter. The upper/lower bound is given by the maximal/minimal amount of dark matter that is allowed within this model. Below masses of around 1 keV dwarf galaxies would not form. The blue point corresponds to an controversial 3.5 keV X-ray emission line in the spectra of galaxy M31 and the Perseus galaxy cluster. Taken from [13].

accelerated expansion of the universe. Dark matter is non-luminous matter that hardly interacts with baryonic matter but is affected by gravity [3]. The Standard Model has no particle candidate that could explain all DM. Only the active neutrinos could be considered as DM because they have no electric charge. Active neutrinos are, because of their small masses, nearly always ultra relativistic and can therefore not explain dark matter by themselves. Even for small kinetic energies they have a very long free streaming length. Thus, they hardly interact with the material around them after they are created, which removes energy from the system the neutrinos were created in. This washes out small scale structures. If only active neutrinos were responsible for dark matter, the structures observed today would not be possible. Active neutrinos act as so-called hot dark matter.

The best agreements between observation and simulation is obtained with weakly interacting, non-relativistic particles, so-called cold and warm dark matter [3]. A candidate for cold or warm dark matter would be a sterile neutrino with a mass of $\mathcal{O}$(keV). Constraints on the mass of the sterile neutrino and also the mixing with active neutrinos are set by cosmological observations. This is depicted in figure 1.3. The white space is the allowed parameter space for sterile neutrinos if these make up 100 % of dark matter. Over- or underproduction of dark matter constrain the mixing of sterile to active neutrinos. Non-observation of X-rays coming form the decay of sterile neutrinos into a photon and an active neutrino, set additional boundaries

[13]. The Tremaine-Gunn limit further constrains the mass to $\geq 1\,\mathrm{keV}$. This limit is set by the phase space distribution of sterile neutrinos that cannot exceed the distribution of the degenerate Fermi gas in a galaxy. This is due to the fact that sterile neutrinos are assumed to be fermions. Otherwise, small structures like dwarf galaxies would not form [3].

By combining these observations, model-dependent bounds can be obtained for the mass $1\,\mathrm{keV} < m_s < 50\,\mathrm{keV}$ and for the mixing $10^{-13} < \sin(2\Theta) < 10^{-7}$ [34]. This shows that right-handed sterile neutrinos could solve the question about the small scale of the active neutrino masses or could be a DM candidate.

1.3. KATRIN Experiment

The Karlsruhe Tritium Neutrino (KATRIN) experiment determines the effective electron anti-neutrino mass by measuring the electron energy of the β-decay. The effect of the anti-neutrino mass on the electron spectrum is shown in figure 1.4. The mass of the anti-neutrino shifts the endpoint energy of the spectrum to lower energies corresponding to the neutrino mass. Therefore, by measuring the region of the endpoint of the spectrum and comparing it to the expected spectrum without a neutrino mass, the effective neutrino mass of equation (1.4) can be determined. KATRIN is designed to have a sensitivity of 200 meV at 90 % C.L. This is one order of magnitude better than the limits predecessors of KATRIN achieved [9, 28]. Improving by this much is only possible because of the high-luminous tritium source and an electron energy filter with an energy resolution below 1 eV.

A keV-sterile neutrino would have a similar effect on the β-spectrum as active neutrinos have, but because of the much bigger mass, the imprint would be visible deeper in the spectrum. The mixing of sterile with active neutrinos is expected to be extremely small. Therefore, to detect this imprint a lot of data is needed. This makes the KATRIN setup with its high-luminous source very promising for the search for sterile neutrinos. For this reason KATRIN is explained in the first part of this section and afterwards it is shown how to detect a sterile neutrino in the β-decay spectrum.

1.3.1. Setup

KATRIN uses integral measurements of the β-spectrum. This means that the electrons, created in the source, are selected by their energy through a spectrometer. All electrons above a certain energy is counted in the detector. This is done for different energies in a region around the endpoint of the spectrum. The setup of KATRIN is shown in figure 1.5. The experiment consists of five main parts.

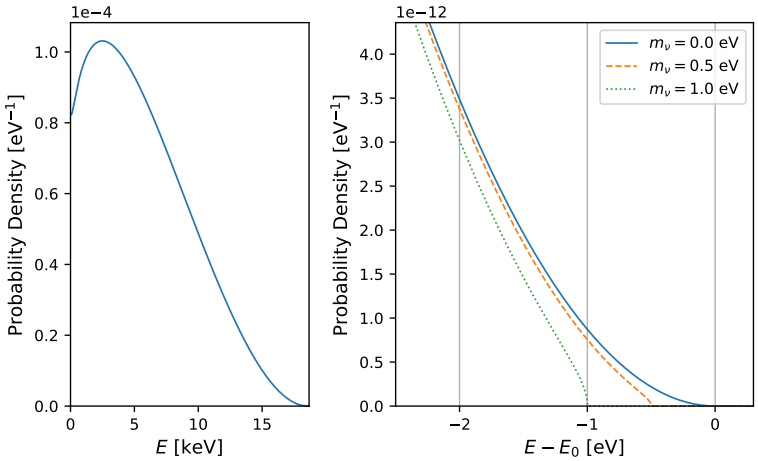

Figure 1.4.: Effect of the anti-neutrino mass on the β-spectrum endpoint. *Left:* Differential spectrum of the β-decay electrons. *Right:* The endpoint of the spectrum is shifted to lower energies according to the mass of the anti-neutrino. The endpoint without a neutrino mass is denoted by E_0. Adapted from [35].

a) Rear section
b) Windowless Gaseous Tritium Source (WGTS)
c) Transportation section
d) Spectrometer section
e) Focal Plane Detector (FPD)

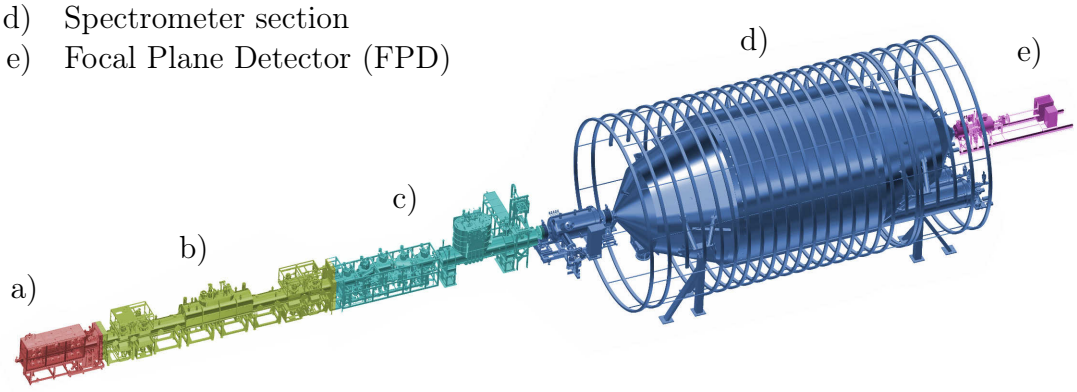

Figure 1.5.: KATRIN setup overview. Taken from [52].

Rear Section

The rear section's main purpose is to supply an electric potential to the tritium plasma in the source by providing a conducting surface. This is done by a gold plated stainless steel disk, the rear wall. Also, calibration tools and monitoring devices for the tritium in the source are located here [10].

Windowless Gaseous Tritium Source

Tritium gas is continuously injected into a 10 m long and 90 mm wide steel tube, the Windowless Gaseous Tritium Source (WGTS). Inside the source the gas streams freely to both ends. There it is pumped out of the tube to be refurbished and then reinjected into the source. This way a tritium purity above 95 % is achieved. The decay rate is stabilized to 10^{11} decays/s with a variation below 0.1 % [25].

Transport Section

In this section the residual tritium has to be reduced by 14 orders of magnitude. Mainly turbo-molecular pumps are used for the reduction, but also cryogenic pumps with a small argon frost layer that traps tritium molecules. Further reduction is achieved by the chicane shape of the transport section. Electrons are guided adiabatically by magnetic fields, while molecules hit the walls and are then pumped away.

Spectrometer Section

KATRIN uses two spectrometers to select the electrons that are counted in the detector. Both are built as Magnetic Adiabatic Colliminator and Electrostatic (MAC-E) high-pass filters, the principle is shown in figure 1.6. The electrons are guided by an magnetic field inside the spectrometer. Because of their momentum being not purely parallel to the field lines they perform cyclotron motion along the field lines. In the center of the spectrometer a high electric potential U is applied, the retarding potential. This field decelerates all electrons and rejects those with kinetic energies below qU. Because the cyclotron motion around the magnetic field lines, the energy of an electron E_e is split in a forward motion (parallel to the electric field lines) $E_\parallel$ and one perpendicular to the forward motion $E_\perp$:

$$E_e = E_\parallel + E_\perp \tag{1.6}$$

The rejection through the electric potential acts only on $E_\parallel$. To not falsely reject electrons which energy is mainly in the cyclotron motion, the magnetic field has its maximum strength at the beginning and the end of the spectrometer. The minimum

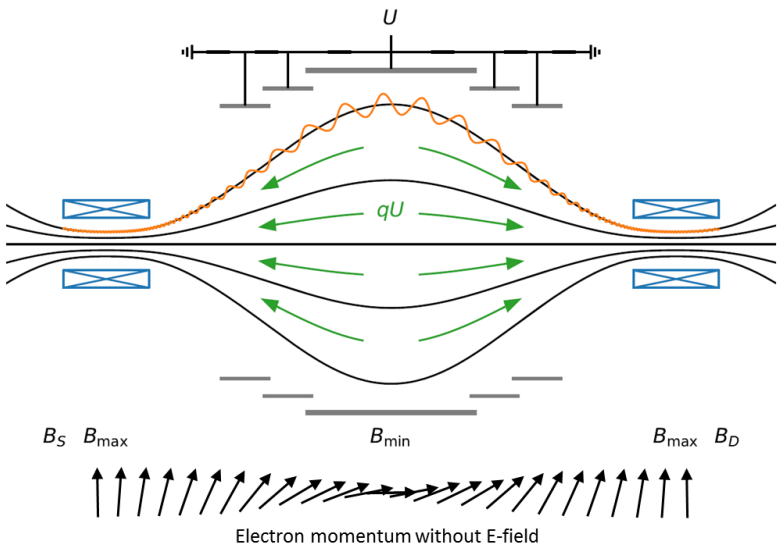

Figure 1.6.: Working principle of a MAC-E filter. Electrons are entering from the left. A magnetic field with a gradient (black) shifts the electron momentum to be parallel in the middle of the spectrometer. In the center, also a high retarding potential is applied (green) to reject all electrons with energies below qU. Taken from [47].

lies exactly in the center, corresponding to the point where the electric potential is applied. This magnetic gradient reduces the cyclotron motion adiabatically, so that the momentum of the electron is shifted to be parallel to the field lines, in the middle of the filter (see bottom of figure 1.6). This way all kinetic energy is parallel to the electric field lines and no electron is falsely rejected. The energy resolution of the spectrometer can be calculated with equation (1.7) and is below 1 eV.

$$\frac{\Delta E}{E} = \frac{B_{min}}{B_{max}} \tag{1.7}$$

After passing the filter, the electrons are accelerated and guided to the detector.

The KATRIN experiment uses an integral measurement technique. The retarding potential of the MAC-E filter is varied and all electrons above a set voltage are counted in the detector.

Focal Plane Detector

The Focal Plane Detector (FPD) is located at the end of the KATRIN beamline. It consists of 148 pixels with 44 mm^2 each, arranged in twelve concentric rings. The layout is shown in figure 1.7. Each pixel is a pin-diode which is explained in

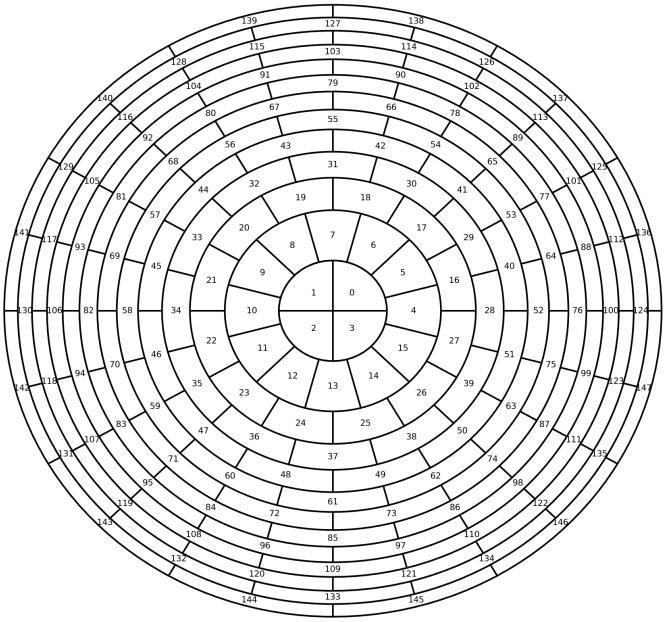

Figure 1.7.: Layout of the focal plane detector. It has 144 pixel and is segmented into twelve concentric rings. Each pixel has the same size. Taken from [47].

section 2.1 and records its own spectrum. The detector has a diameter of 90 mm. In front of the detector is an additional post-acceleration that increases the energy of the incoming electrons, because the detector efficiency is better for higher energies.

The energy resolution of the detector is about 1.5 keV, which is not of importance because resolution of the measurement is given by the MAC-E filter and the detector only serves as a counter. The maximum rate the detector and readout can handle is 62 kcps [25].

1.3.2. Sterile Neutrino in the β-Spectrum

The neutrino mass eigenstates (ν_1, ν_2, ν_3) reduce the endpoint of the β-spectrum. Another neutrino mass eigenstate ν_4 would have a similar effect. This is shown, largely exaggerated, in figure 1.8. The β-spectrum is a superposition of all four mass eigenstate spectra. Therefore, the endpoint of the sterile neutrino spectrum would manifest itself as a kink in the summed spectrum. This influence can by described by:

$$\frac{\mathrm{d}\Gamma}{\mathrm{d}E} = \underbrace{\cos^2 \left(\frac{\mathrm{d}\Gamma}{\mathrm{d}E}\right)_{m_{\nu_e}} \Theta(E_0 - E - m_{\nu_e})}_{\text{Active Neutrino}} + \underbrace{\sin^2 \left(\frac{\mathrm{d}\Gamma}{\mathrm{d}E}\right)_{m_s} \Theta(E_0 - E - m_s)}_{\text{Sterile Neutrino}} \quad (1.8)$$

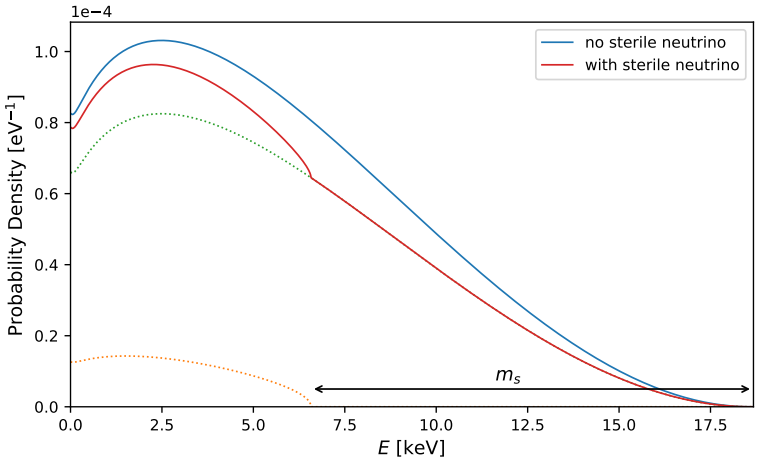

Figure 1.8.: Effect of a sterile neutrino mass on the β-spectrum. A kink appears at an energy below the endpoint of the β-spectrum corresponding the mass of the sterile neutrino. In this case a mass of 12 keV is shown. Taken from [35].

E is the energy of the electron and E_0 is the endpoint of the spectrum. Θ is the mixing angle between active and sterile neutrino and m_s the mass of the sterile neutrino. The position of the kink is therefore at an energy of $E_0 - m_s$.

The high-luminous tritium source of KATRIN is one of its main advantages which also makes it suitable for the search for sterile neutrinos. The tritium spectrum has an endpoint at 18.6 keV that would allow to look for sterile neutrinos up to this mass. With the source and spectrometer of the current KATRIN setup two measurement methods are possible. One is the integral method, that is also used in the search for the neutrino mass. Here, the spectrometer is set to different retarding potentials and the detector counts all incoming electrons. Another way could be a differential measurement in which the MAC-E filter is set to a very small retarding potential at all times. This way the entire part of interest of the spectrum reaches the detector. In both measurement methods the rate on the detector can increase up to around 10^{10} electrons/s, which is too high for the current detector system. A sensitivity study showed that the statistical sensitivity achievable with the KATRIN source, for the mixing angles are $\sin^2(\Theta) = 10^{-9}$ to 10^{-6} for sterile neutrinos [34]. This depends on the measurement method and can be seen in figure 1.9. The sensitivity study shows that the imprint of a sterile neutrino is stronger in the differential measurement method. With the WGTS of KATRIN up to 10^{20} decays are measurable in three years. This amount of data would lead to further improvements on currently existing laboratory limits [35]. To achieve this

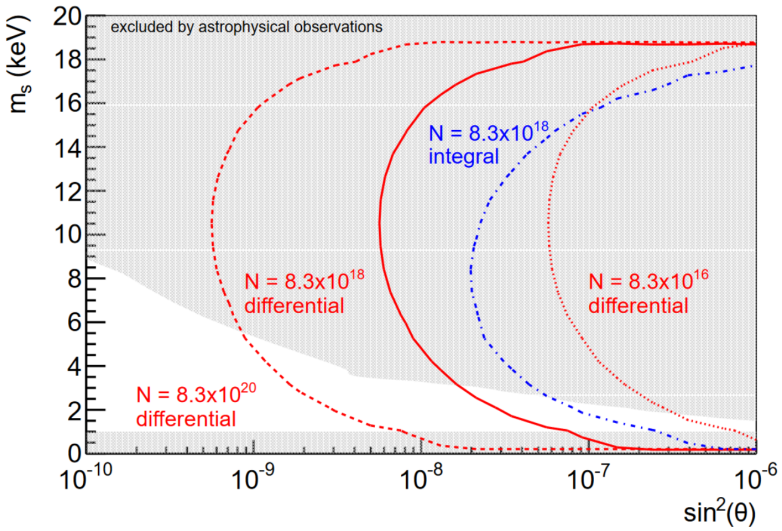

Figure 1.9.: Statistical sensitivity for a keV sterile neutrino using the KATRIN source. The differential and integral denote different measurement methods. N is the number of measured electrons. The gray area is excluded by astrophysical observations. Taken from [34].

sensitivity a new detector system has to be developed that can handle the high rates necessary for the investigations.

1.4. TRISTAN Project

The current KATRIN detector is not suited to search for keV-sterile neutrinos because it cannot handle the high electron flux. A new detector system is needed for this kind of search. To develop this detector is the aim of the Tritium Investigation on Sterile (A) Neutrinos (TRISTAN) project.

Requirements for the Sterile Neutrino Search

To achieve a statistical sensitivity for the mixing angle of $\sin^2(\Theta) < 10^{-6}$ and the mass $m_s < 18.6\,\mathrm{keV}$ at least 10^{16} electrons need to be analyzed [35]. Assuming a measurement period of three years, the electron rate will be around $10^8\,\mathrm{counts/s}$ on the detector. Handling such high rates requires the detector to have multiple pixels, which distributes the rate. Reducing the pile-up probability leads to a minimum of 1000 pixels. Furthermore, the read-out system of the detector has to be extremely fast to cope with the rates. Thus, the shaping time τ of the system has to be small.

Another requirement is the excellent understanding of the whole tritium β-decay

spectrum. Probing the parameter space in regions of cosmological interest, an understanding on the part-per-million level is needed [34]. Therefore, the detector needs an energy resolution of 300 keV at 30 keV and the detector response has to be precisely known. If the resolution is too big the kink-like structure is not visible in the obtained spectra.

The series noise of a detector system Q_{series} influences the energy resolution. Equation (1.9) shows that the noise is correlated to the shaping time τ [49]:

$$Q_{\text{series}} = \frac{C_d}{\sqrt{\tau}} \sqrt{4k_B T R_s + e_{\text{ampl}}^2} \tag{1.9}$$

The proportionality to the inverse of the shaping time shows that a balance between short shaping times and low series noise has to be found. All the other parameters: the capacitance of the detector C_d, the noise of the signal amplifier e_{ampl}, the series resistance of the detector R_s, and the temperature T need to be as small as possible. Here, k_B denotes the Boltzmann constant.

Finally, the entrance window of the detector needs to be extremely thin. Electrons lose a significant fraction of their energy shortly after entering the material. If some or all deposited energy in the entrance window is lost, the resolution is worsened and the entire spectrum is shifted to lower energies. With a thin entrance window this effect is smaller. Because it is important to know the influence of the entrance window of the detector on the tritium spectrum, in this thesis the entrance windows of the TRISTAN prototype detectors (described in chapter 2) are characterized. Also a new production technique for the detectors is investigated.

Final TRISTAN Detector

All of the requirements mentioned above can be achieved with a multi-pixel detector system of silicon drift detectors. Following a detailed Monte-Carlo simulation [27], the TRISTAN detector system will consist of around 3500 silicon drift detectors. The working principle of the detectors is explained in section 2.1.2. Silicon drift detectors allow for extremely small capacities of $C_d = 110\,\text{fF}$. Each pixel will have a diameter of 3 mm. They will be grouped into twenty-one modules with 166 pixels each, the design of one module is shown in figure 1.10. Each module consists of one silicon drift detector chip, one cooling block and the first electronics stage. The final system will have a diameter of around 18 cm, a drawing is shown in figure 1.11.

The current prototype detector with seven pixels will be discussed in more detail in chapter 2.

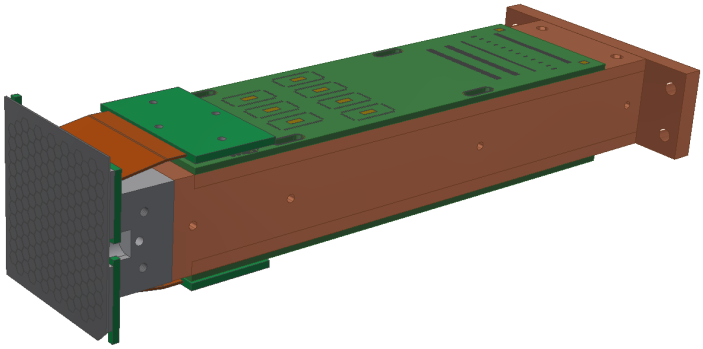

Figure 1.10.: Design of a TRISTAN module prototype. It consists of one 166 pixel silicon drift detector chip, a cooling block, and the first electronics stage. Taken from [46].

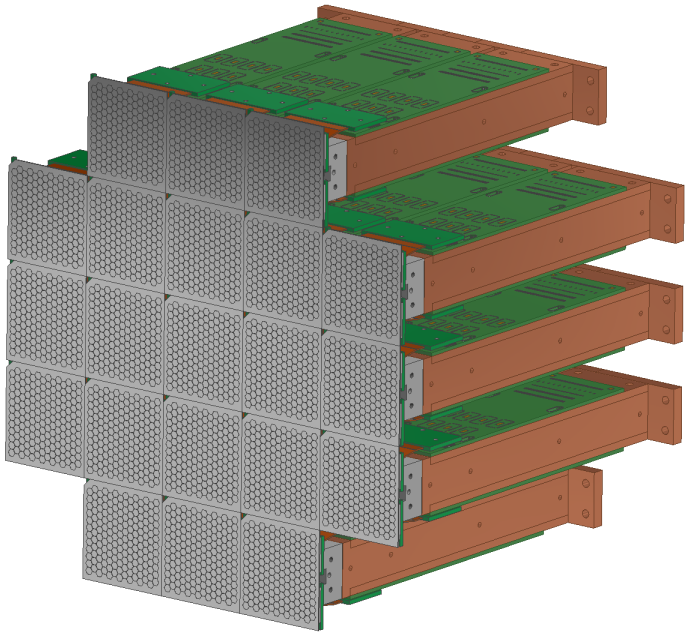

Figure 1.11.: Design of the final TRISTAN detector system made out of twenty-one modules. Taken from [46].

2. TRISTAN Prototype Setup

In this section, an overview of the current TRISTAN prototype detectors is given. The first part describes the working principle of semiconductor detectors. Afterwards, the silicon drift detector (SDD) is described as it is the type of detector used in the TRISTAN project. Following that, the current prototype detector setup is depicted. In the end, the readout chain of the experimental setup is explained.

2.1. Functional Principle of the TRISTAN Detector

2.1.1. Basic Principle of Semiconductor Detectors

The working principle of semiconductor detectors depends on the band structure of the used materials. In contrast to metals, in semiconductors there is an energy gap between the conductive band and the valence band but it is not as big as in insulators. This means that electrons in the valence band can be excited to cross the gap and enter the conductive band. Therefore, semiconductors are able to conduct electricity but not as well as metals do. The different band structures of metals, semiconductors, and insulators is shown in figure 2.1.

A semiconductor's conductivity is temperature dependent, as close to absolute zero nearly no electrons have enough energy to be in the conductive band. However, the higher the temperature of the material, the higher the chance to thermally excite electrons into the conductive band.

A widely used semiconductor detector material is silicon because it is one of the most abundant elements in the earth's crust [56], and has a band gap of about 1.1 eV at room temperature [22]. Thus, the energy to create one electron-hole pair $\omega = 3.64\,\text{eV}$ is fairly low [37]. Therefore, many electrons are created and able to enter the conductive band per deposited energy. This leads to a better energy resolution compared to other semiconductor materials.

To modify the conductive behavior of the semiconductor it is also possible to dope it with other materials, by adding other materials additional energy levels can be created inside the gap. Thus, the necessary energy for excitement is lowered. This process also creates free electrons or free holes. There are two ways to achieve this for silicon, a type IV element. The first is to dope the semiconductor with

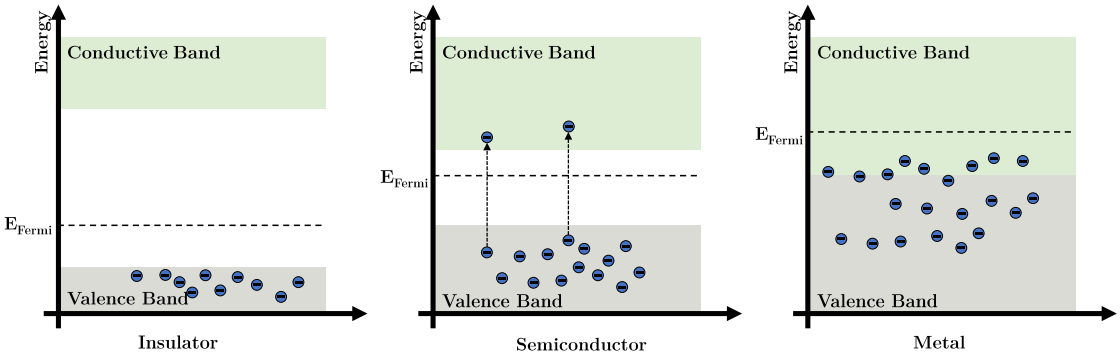

Figure 2.1.: Schematic drawing of the band differences of insulators, semiconductors and metals. The energy gap between valence and conductive band in insulators is too big for electrons to cross. In semiconductors the gap is small enough that some electrons may be excited, thermally or otherwise, to enter the conductive band. Metals do not have a gap and the bands can even overlap. Therefore, they are always conductive. The Fermi energy is shown to indicate the maximum energy non-excited electrons can have.

type V material, e.g. phosphorus. This creates an n-type semiconductor with an energy level close to the conductive band. Hence, even for low temperatures there are some electrons inside the conductive band. The other way is to add type III elements, e.g. boron. This leads to p-type semiconductors with an additional energy level close to the valence band. Consequently, free holes are created in the valence band, as electrons enter this new energy level. These two doping types are shown schematically in figure 2.2.

Incoming particles deposit energy and create electron-hole pairs. The number of those is usually several orders of magnitude lower than the number of free charge carriers at room temperature in an intrinsic silicon substrate. Thus, the signal would be lost in thermal noise. To prevent that and to be able to use a doped silicon substrate as a particle detector, the free charge carriers have to be reduced drastically [21].

To do so, the silicon volume is depleted of free charges by using a reversed-bias pn-junction. The operating principle of such a junction is shown in figure 2.3. A pn-junction is the combination of a p- and an n-type semiconductor. The excess electrons of the n-type material move to the p-type material while the surplus holes of the p-type move to the n-type. Therefore, recombination happens and charged dopant atoms are created until an equilibrium is established (figure 2.3b). This results in an electric potential, the so-called diffusion voltage $U_{\text{diffusion}}$. In the transition area of the two types no free charges exist. This area is called depletion

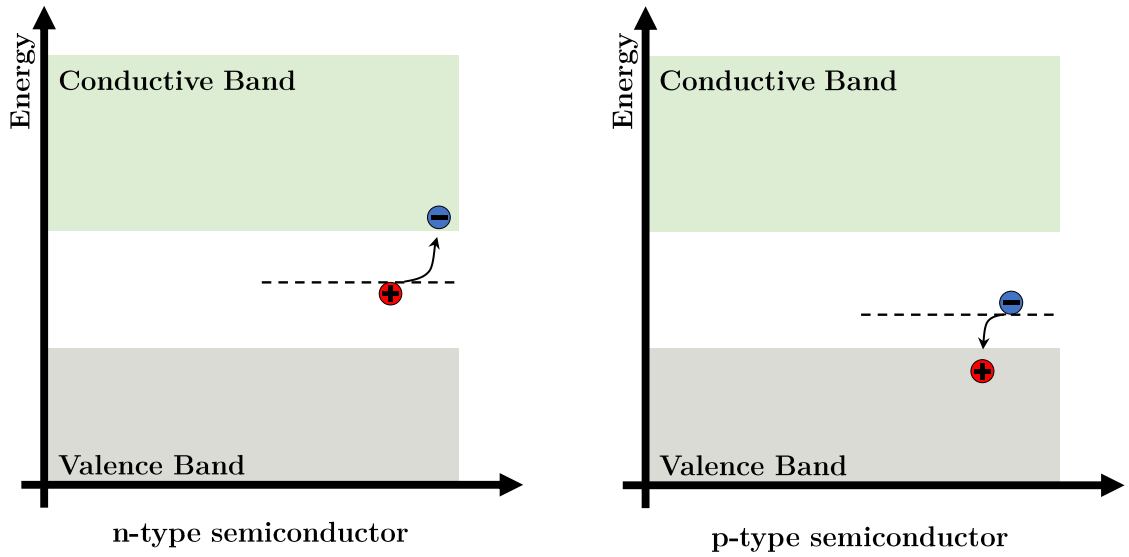

Figure 2.2.: Schematic drawing to illustrate n- and p-type doping mechanisms. *Left:* n-type semiconductors have additional energy levels close to the conductive band. Hence, even at low temperatures electrons enter the conductive band. *Right:* The p-type semiconductors have another energy level close to the valence band. Therefore, for every dopant atom, one or more electrons have this energy, which leaves free holes in the valence band.

zone, shown in figure 2.3c [21].

Applying an external voltage U_{bias}, which has the same polarity as $U_{\text{diffusion}}$, increases the depletion zone. Thus, the whole pn-junction becomes completely depleted (figure 2.3d).

Particles entering the material lose energy and create electron-hole pairs. If this happens in the depletion zone, recombination cannot happen. Hence, due to the electric field, all created electrons drift to the n-type part, the anode, where they are read out. The signal's amplitude is proportional to the deposited energy. The holes similarly move to the p-type part.
This detector type is called a positive-intrinsic-negative diode (pin-diode).

2.1.2. Working Principle of an SDD

The first working silicon drift detector was introduced by Rehak and Gatti [42]. It is based on the principle of sideward depletion and depends on a small anode capacitance [29]. It is most suitable for measurements of X-rays and charged particles.

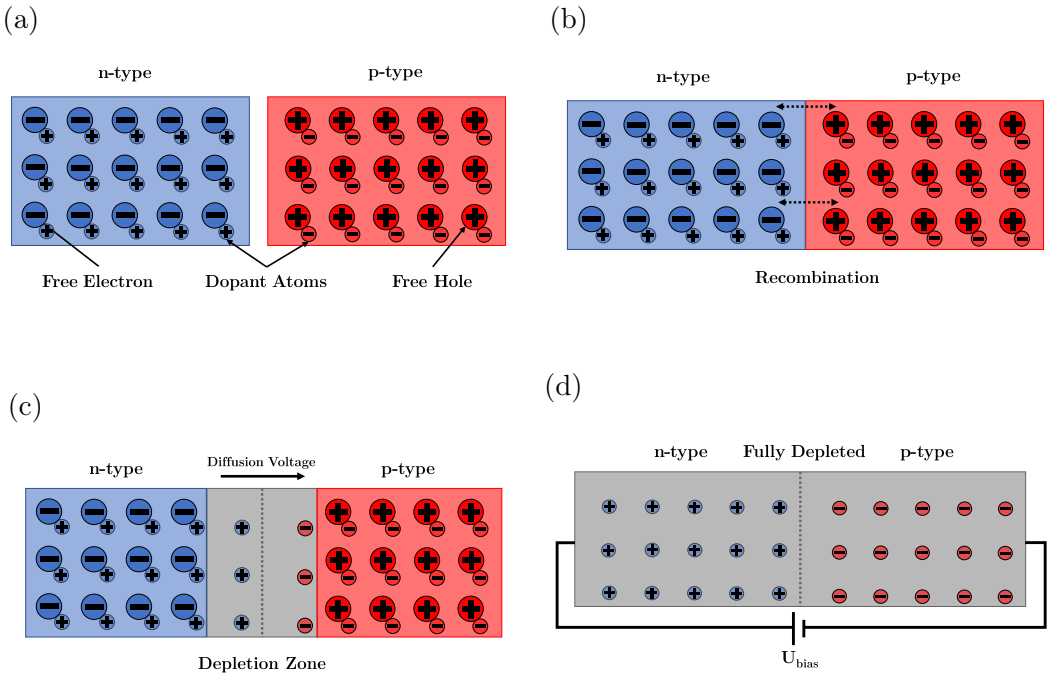

Figure 2.3.: The implementation of a pn-junction is illustrated by several steps. In figure (a), the n-type semiconductor with additional electrons is shown in blue and the p-type with additional holes is shown in red. When the two types are combined, figure (b), recombination happens at the contact area as electrons drift from the n-type part into the p-type one and vice versa for the holes. Therefore, the gray depletion zone of figure (c) is created, without free charges. This also builds the internal diffusion voltage which stops any further recombination. If an external potential in the direction of the diffusion voltage is applied to the junction, the complete detector can be depleted, as shown in figure (d).

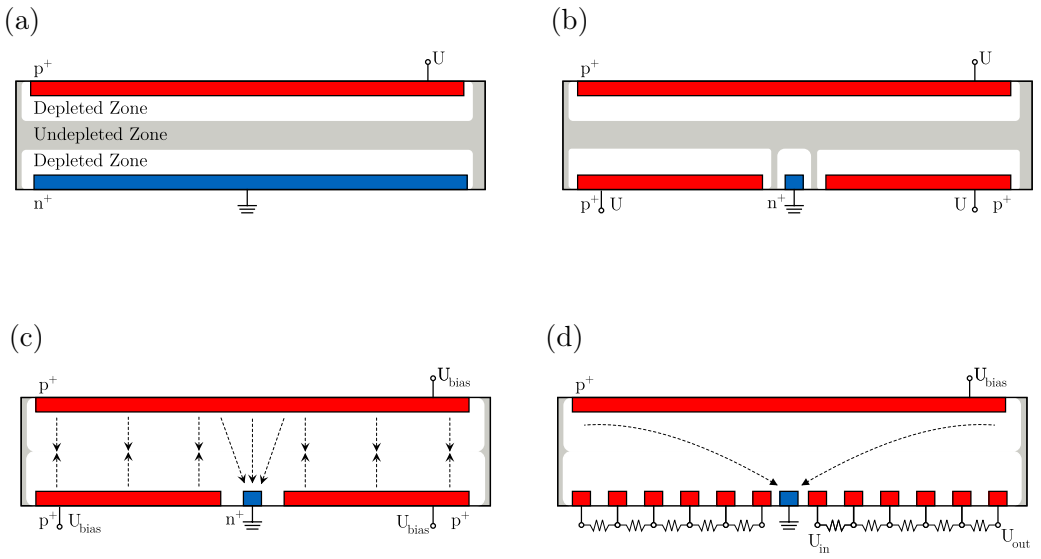

Figure 2.4.: The steps necessary to get from a pin-diode to an SDD are shown in figures (a) to (d). It starts with a pn-junction where the ohmic contacts for the n^+ anode (blue) and the electrode (red) cover the whole surface of a detector on each side and some voltage U is applied to the p^+ electrode . In this illustration, U is lower than the bias voltage U_{bias}, necessary to deplete the whole volume. The same result as in (a) can be achieved if the anode is mostly replaced by additional p^+ electrodes, which also have to be supplied by voltage U. Applying U_{bias} results in a nearly complete depletion of the detector, as shown in (c). But thereby only electrons close to the anode are directed towards it, as most electric field lines are perpendicular to the surface and do not point in the direction of the anode. An electric potential may be established in the detector which has its minimum at the position of the anode. To do so, the p^+ electrodes on the anode side need to be replaced with electrode strips, on which gradually decreasing voltages from U_{out} to U_{in} are applied. Thus, all electrons inside the depleted part of the SDD drift to the anode (d). Pictures adapted from [47].

The working principle of an SDD is explained in figure 2.4. In figure 2.4a the ohmic n^+ layer covers one side of the diode. By applying an external voltage U some area around the p^+ layer is depleted. A similar depletion can be achieved if the n^+ is, except for a small area, exchanged by p^+, which is shown in figure 2.4b. If now the voltage U is increased to the bias voltage U_{bias}, the whole detector volume is depleted. The n^+ takes the role of the anode and all p^+ layers are cathodes. In this configuration, only one fourth of the potential is needed compared to a pin-diode with the same area and volume [11].

With the design in figure 2.4c, the electric field is mostly perpendicular to the surface. Therefore, only electrons close to the area above the anode are guided to the latter. By replacing the p^+ areas on the anode side of the detector by an array of strips and applying decreasing voltages from U_{out} to U_{in} to each strip, a field parallel to the surface is established. The electrons drift to the n^+ due to the resulting electric field which has its minimum at the anode. This is illustrated in figure 2.4d. A simulation of such a field can be seen in figure 2.5. In this simulation, the equipotential of the area p^+ is shown in the back and the field strips with their step-like negative potential are shown in the front.

As practically no electrons are lost in an SDD, the whole charge cloud of an incoming particle can be measured. Therefore, the pulse height of the output signal is proportional to the deposited energy.

The most important advantage of SDDs over pin-diodes is the small capacitance of the anode. In SDDs it is in the order of 100 fF and practically independent of the active area of the detector. This is important as it reduces electronics noise and allows for small shaping times during signal processing [11].

Usually in particle physics, linear or matrix-like SDDs are used. But also radial designs exist as shown in figure 2.6. The radial design has the advantage that in this configuration it is much easier to terminate the field lines [29]. The potential is radial symmetric because the p^+-electrodes are circular and are called "drift rings". Therefore, the electron cloud is guided to the middle of the detector where the anode is located.

2.1.3. Influence of the Entrance Window on Particles

Unlike photons, electrons continuously lose energy when traveling through matter. Their high interaction rate with the material is due to their charge. Therefore, they create secondary electrons and holes on their way. Due to the spatial expansion of the p^+ doping, the electric potential inside the detector material, i.e. inside the bulk, is not the same as on its surface. This leads to a different behavior of electrons created on the surface compared to inside the bulk [31, 40]. Electrons do not drift towards the anode but diffuse in an uncontrolled way.

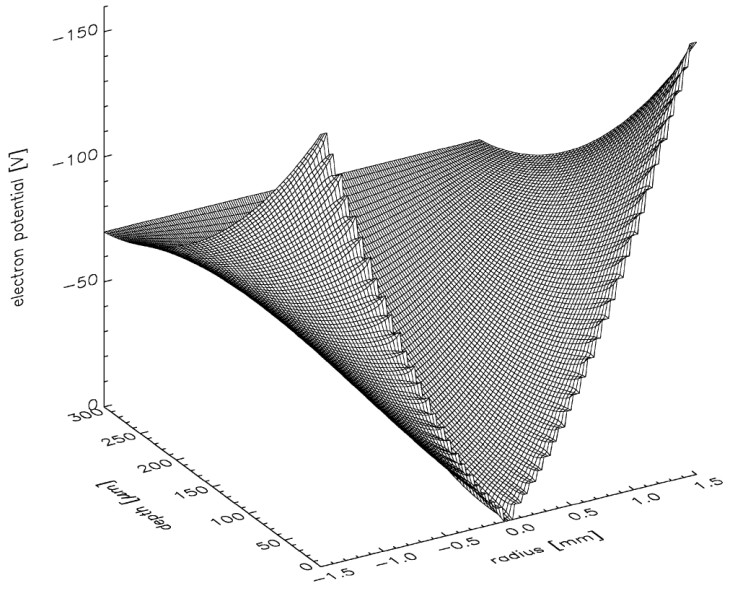

Figure 2.5.: Simulation of the resulting electric potential inside an SDD. In the back is the homogeneous potential of the entrance window. The front shows the step wise decreasing potential of the strip electrodes. Therefore, the anode is at the minimum potential. Taken from [29].

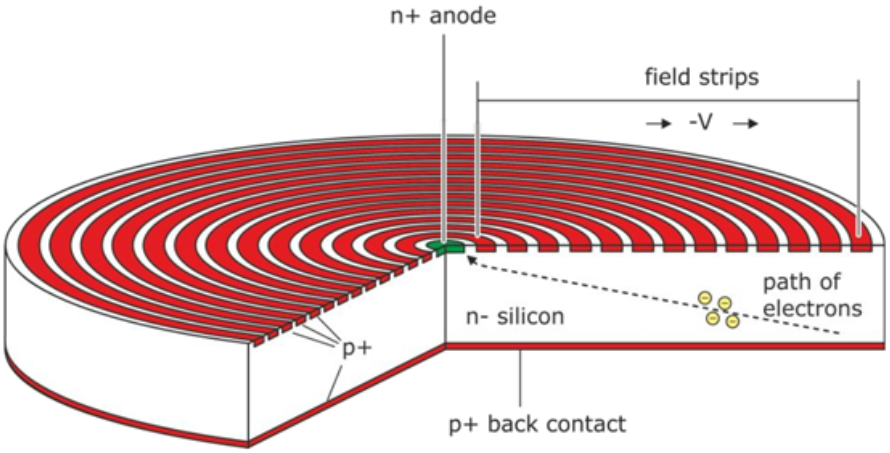

Figure 2.6.: Radial design of an SDD. The p^+ back contact is the entrance window of the detector and has the same doping as the drift rings in red. Taken from [47].

There are effects that also lead to charge losses. One contribution is the silicon oxide on the detector. In this layer no deposited energy is detected. This SiO_2 is always present as it results when silicon is exposed to air. By adding such a layer before it naturally grows, it can be created as homogeneously as possible and also protects the detector from further oxidation [47]. For the TRISTAN detectors this layer is usually 8 to 10 nm thick. Behind this is a volume of incomplete charge collection because of the expansion of p^+.

The easiest way to describe this behavior is the sharp edge dead layer model. For this it is assumed that the entrance window of the detector is completely insensitive followed by a complete charge collection. A slightly advanced version of this is by assuming the silicon oxide is completely dead and afterwards a "washed-out" step function with a position and a spread describes the shape of the charge collection efficiency (CCE). This takes into account that events that deposit energy close to the entrance of the detector create charges which are partly lost. Therefore, the energy cannot be measured completely. In this thesis both of these models are used. For the characterization of TRISTAN prototypes a sharp edge dead layer will be used. These detectors have been highly optimized for the detection of electrons and thus a thin dead layer is a reasonable assumption. In the second part of this thesis a washed-out step function will be used because the investigated pin-diodes are not optimized for electrons.

A common approach of testing if such models fit real experimental results is by using Monte-Carlo simulation software. Geant4 is a toolkit developed at CERN and widely applied in high energy, nuclear, medical, and accelerator physics. It is implemented in the C++ programming language [8]. With this a wide range of particles and materials can be simulated. Also different interaction mechanisms like electromagnetic or hadronic can be taken into account. Additionally, the properties to take into consideration and which to neglect can be chosen. Its variety of possible applications make it suitable to simulate the detector response of the TRISTAN prototypes to the emitted conversion electrons and photons of the ^{83m}Kr decay. The description of electrons in the silicon detectors for the KATRIN experiment with Geant4 was not precise enough. Therefore, a new software called KESS was developed. The aim was to model especially the energy loss of low-energy electrons, the energy deposition, and the production and tracking of secondary electrons in silicon very precisely [43]. For this reason it is used to simulate the response of pin-diodes to incoming electrons at different energies, especially in the range of 1 to 2 keV. This is used in chapter 4 of this thesis.

2.2. TRISTAN Prototype Detector

The prototype detectors of the TRISTAN project are silicon drift detectors with a thickness of 450 µm. The prototype's pixels are not circular (as described above) but hexagonally shaped. This gives all benefits of the radial design, but additionally allows for pixel arrays without gaps and therefore increases the maximum coverage area. The diameter of a pixel is 2 mm. The arrangement of pixels is shown in figure 2.7.
The bias voltage needed to fully deplete the detector is called back contact voltage. It is $U_{\text{bias}} = U_{\text{BackC}} = -90\,\text{V}$. This is applied to the p^+-doped side of the area on the entrance window. To prevent electrons created inside the pixel from leaving and guarding it from outside electrons, an additional p^+-guard-ring surrounds the detector. It is called back frame and is set to $U_{\text{backframe}} = -100\,\text{V}$. The entrance window and the contact points are shown in figure 2.8.

The electric field guiding the electrons to the anode in the center of each pixel is created by twelve drift rings on the electronic side of the detector. The gradient between each ring is given by the difference of potentials of the outermost ring $U_{\text{ringx}} = -110\,\text{V}$ and the inner most ring $U_{\text{ring1}} = -20\,\text{V}$. The anode, shown in figure 2.7, has a diameter of 90 µm and therefore a capacitance 110 fF. The connection to the first amplification stage is an aluminium bond with 18 µm diameter. With this, the capacitance is hardly increased and additional noise can be reduced. The first amplification is done by the low noise preamplifier application-specific integrated circuit (ASIC)-CUBE [12]. These ASICs are positioned close to the anode around the pixels. The setup of CUBEs can be seen in figure 2.7.

After the first amplification the signal is routed through the detector printed circuit board (PCB) to the output pins. The board also handles the rewired power supply for the ASICs and the detector.

For the TRISTAN project, several detectors with different entrance windows have been produced. To distinguish them the naming scheme of table 2.1 was developed. The first two letters describe the doping profile used for the detector. The number is an integer increasing with every new detector of a kind.

The standard entrance window doping profile is not TRISTAN specific [40] and highly optimized for photon detection. To further decrease the thickness of this ultra thin entrance window other doping profiles are tested. One technique is to lessen the dose of implants during the process. This reduces the p^+-doping and therefore the depth to which the dopant atoms enter the detector, as shown in figure 2.9. The advantage is that it shifts the electric fields maximum closer to the surface (figure 2.9). But it increases the risk of not fully depleting the detector. This is tried for the R0 detectors. An alternative is to implant n^+ behind the p^+ doping. This again has the risk of not fully depleting the detector if the dopings are not

Table 2.1.: Naming scheme to differentiate the different TRISTAN prototype chips. It represents the entrance window technology and how many detectors of this sort have been acquired.

Detector	Description of doping profile
S0-#	Standard implantation
SC-#	Standard implantation with Counter implantation
R0-#	Entrance window with Reduced dose
RC-#	Entrance window with Reduced dose and Counter implantation

perfectly balanced. This was applied on the SC detectors. Both approaches were used in the RC detectors. Unfortunately, these detectors had large inconsistencies and malfunctions [47].

For the investigations in this work, only S0 and R0 detectors were used.

2.3. Readout Chain

The layout of the complete readout chain can be seen in figure 2.10. After the first amplification on the detector board the signal enters the bias board, shown in figure 2.11. There it is amplified again to be transferred through a coaxial cable to the Data Acquisition (DAQ). The bias board sends a reset signal to the ASIC-CUBEs to discharge them. Additionally, it provides the routing of the voltage supplies for the SDD and the ASICs.

An exemplary signal from the bias board is shown in figure 2.12. Here, this so-called waveform is a ramp that is increasing because of the leakage current that constantly charges the input of the CUBEs. The sharp falling edge comes from the reset pulse that is necessary to discharge theASICs, otherwise these saturate and are not able to amplify the signal anymore. A photon or charged particle event appears as a step on the ramp. Particles inside the detector create a number of electrons corresponding to the deposited energy, which charge the ASIC in a short amount of time, much faster than the leakage current.

To identify and analyze events, the waveform is digitized by the DANTE DPP (Digital Pulse Processor) [55]. The DAQ system contains an Analog to Digital Converter (ADC) with a sampling rate of 125 MHz and a resolution of 16 bit. Two digital trapezoidal filters are applied to the waveform, the first of which triggers the second one. The maximum flat top and peaking time of the trigger filter is 248 ns. This first analyzing step removes all events that are below a set threshold. The remaining events are processed by the second trapezoidal filter the so-called

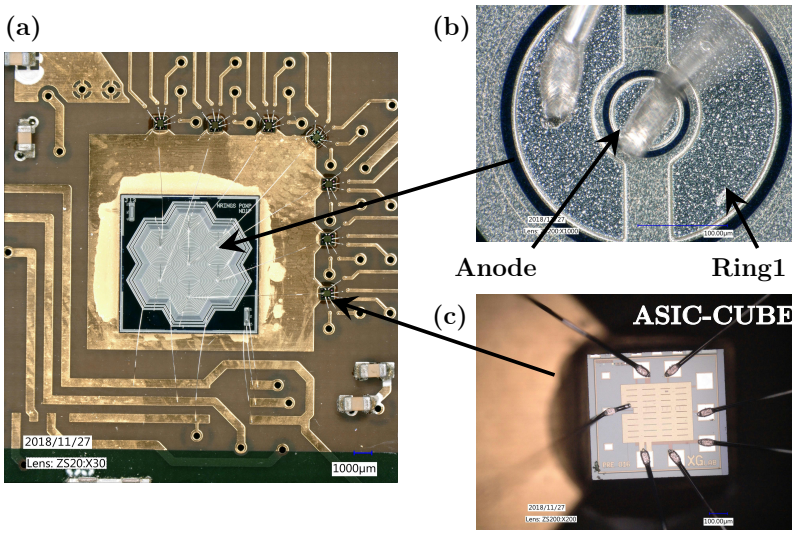

Figure 2.7.: Electronic's side of the detector. In (a) the whole detector is shown. In (b) the anode with the innermost ring and the bonds can be seen. (c) depicts the first amplification stage, the ASIC-CUBE.

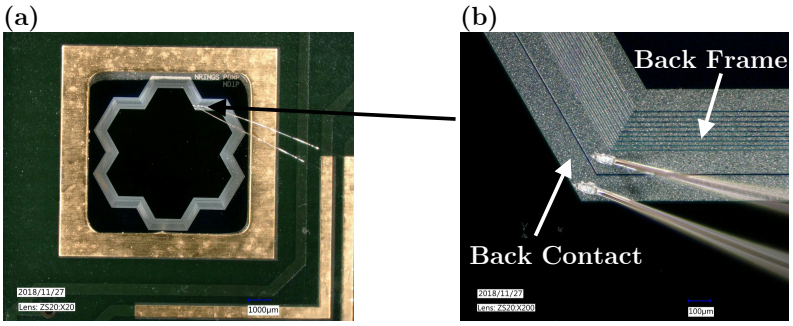

Figure 2.8.: Entrance window side of the detector. In (a) the detector's entrance window is shown. The voltage for the back contact and the back frame are provided via two bonds. The voltages applied via these bonds are responsible for both depleting the detector and guarding it from electron losses. The connection of the bonds is depicted in (b).

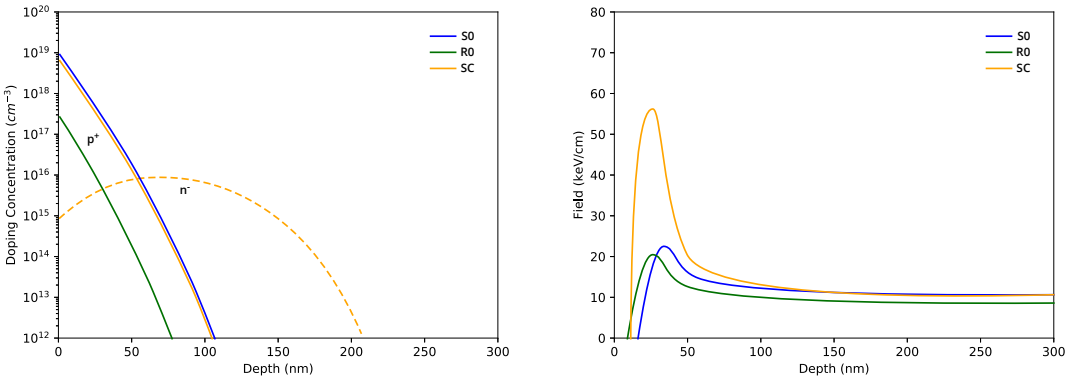

Figure 2.9.: Different doping profiles and their estimated resulting electric fields inside an SDD. S0 and R0 are produced by standard implantation and with reduced dose, respectively. SC has an additional n^+ counter implantation. Visualized profiles are taken from [47].

energy filter. The peaking time can be set up to 16 µs. The best values concerning the energy resolution are obtained with 800 ns with an equivalent noise charge (ENC) < 20 [35].

Pile-up of events happens if two particles enter the detector in a time window smaller than the filtering time. As the fast filter has a very small time window, it detects and rejects most pile-up events.

All these analyses are necessary to make precise and consistent energy measurements. They are performed by the Field Programmable Gate Arrays (FPGA) of the DANTE DPP. The results are either stored in histogram or in list mode. The advantage of the list mode is that through the additional time information effects like multiplicity can be investigated. Multiplicity events happen if the particle hits the detector close to the border of two or three pixels. Then charges of a single event drift to multiple anodes. The advantage of histograms is their much lower memory size.

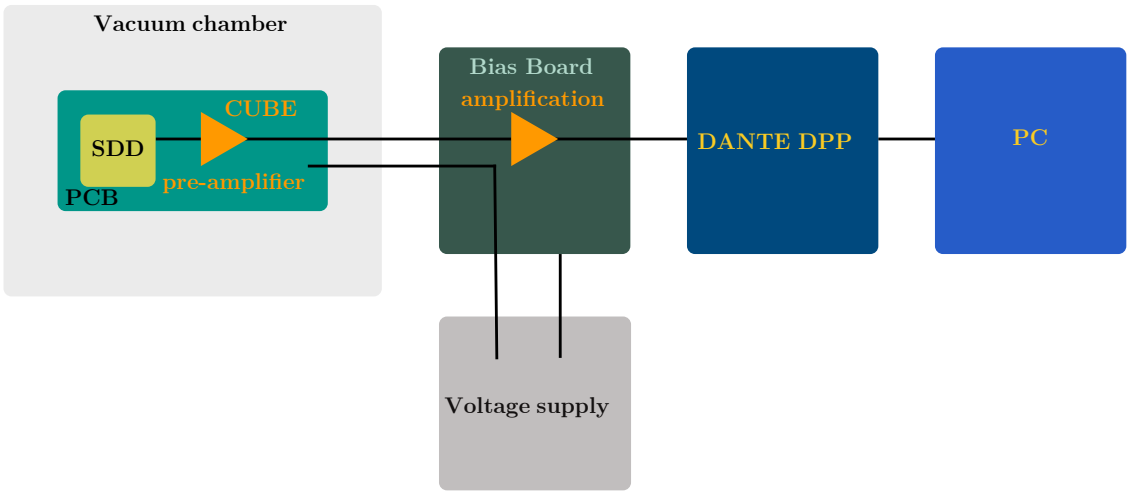

Figure 2.10.: Schematic drawing of the readout chain of the TRISTAN prototype setup. The signal from the SDD is amplified by the CUBE on the detector board. Afterwards it is again amplified on the bias board. Then, the DANTE DPP digitizes the waveform. It also analyses the signal with two digital trapezoidal filters to find events and their pulse height. The result is sent to the software on the computer.

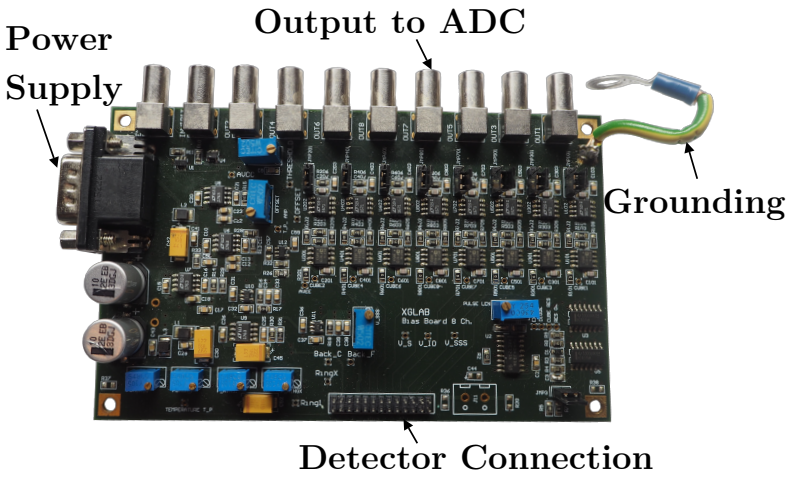

Figure 2.11.: Bias Board of the readout chain. It amplifies the signal a second time and takes care of the routing of the power supplies for the CUBEs and SDDs.

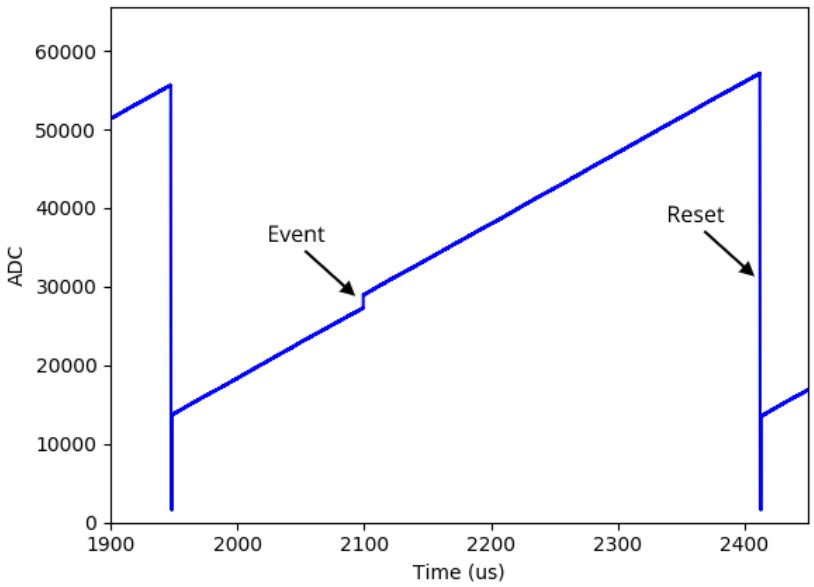

Figure 2.12.: Exemplaric digitized waveform from DANTE DPP. The ramp is created by the leakage current of the detector, continuously charging the CUBEs. An event creates a step on the ramp. At the reset, the ASIC-CUBEs are discharged through the ground. Therefore, the waveform has a sharp edge. Taken from [47].

.

3. Dead Layer Characterization with Conversion Electrons from Krypton

For TRISTAN the electron response of the detector needs to be understood precisely. The entrance window of a detector alters incoming electrons. Therefore, the influence of the entrance window on the measured electron energy is investigated here. For these investigations, the entrance window of the SDDs is assumed to be a sharp edge dead layer. The source of electrons is the decay of metastable ^{83m}Kr, which is described in the first part of this chapter. Afterwards, the principle and setup of the measurement are described. The analysis and results of the measurements are then shown. Simulations need to be performed to translate energy shifts into a dead layer thickness. This is shown in the fourth part of this chapter. Finally, a source influence on the conversion electrons is extracted from the measurements.

3.1. ^{83m}Kr Source

3.1.1. Decay of ^{83}Rb

The metastable state of ^{83m}Kr is used as electron source for the dead layer characterization. During decay it emits conversion electrons. ^{83m}Kr is created in the decay of ^{83}Rb through electron capture. The decay scheme is shown in figure 3.1. ^{83}Rb decays mostly into krypton states that have a lifetime of some ps and have energies of several hundred keV. Because of these energies, they are not suitable for the characterization of the TRISTAN detectors. The isomeric ^{83m}Kr state, which is on an energy level of around 41.6 keV, decays via a cascade of γ-transitions with energies of 32.2 keV and 9.4 keV [57].

A conversion electron is created when an excited nucleus interacts electromagnetically with its shell electrons. Thereby, the electrons get excited or leave the shell of the atom. If only one electron interacts with the core it is quasimonoenergetic. A rough estimation of the kinetic energy of such a conversion electron is given by:

$$E_{\mathrm{kin}}^{\mathrm{vac}} \approx E^{g} - E_{\mathrm{bind}}^{\mathrm{vac}} \tag{3.1}$$

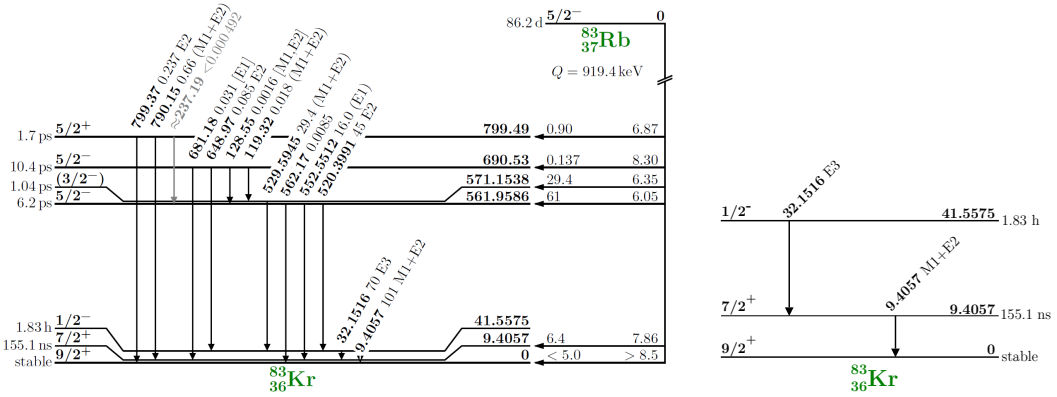

Figure 3.1.: Decay scheme of ^{83}Rb (left) and a zoom into the decay from ^{83m}Kr to ^{83}Kr (right). ^{83}Rb decays after electron capture into the metastable ^{83m}Kr with a branching ratio of 77.9 %. The details on the right show its 9.4 and 32.2 keV γ-transitions. The schemes are taken from [53].

Here, E^{γ} is the energy of the γ-transition and $E^{\mathrm{vac}}_{\mathrm{bind}}$ the binding energy of the shell atom with respect to vacuum.

Additionally to the conversion electrons, X-rays and Auger electrons also are produced during the transitions. These are created after the conversion electron left the atomic shell and the hole is filled by another electron from a higher shell. Because of its now lower ground state it releases a photon, corresponding to the energy difference of the outer and inner shell. This photon can either leave the source unhindered (X-rays) or transfer its energy to another electron in an outer shell, which then has enough energy to leave the atom (Auger electron).

The sources used in this thesis are implanted on graphite. One source is evaporated onto Highly Oriented Pyrolithic Graphite (HOPG), while the other's backing is rigid graphite. Solid ^{83}Rb on HOPG has been extensively used and investigated by the KATRIN collaboration [36, 53, 57, 58]. Thus, it is well understood. The rigid graphite is only an experimental backing and not as well understood as HOPG. The solid form also has the advantages of much easier handling and storage than gaseous rubidium.

The usage of bound ^{83m}Kr changes the kinetic energy of the conversion electrons. This is because in a bound state the electrical potential at the atom is changed. Therefore, equation (3.1) must be rewritten [1]:

$$E^{\mathrm{impl}}_{\mathrm{kin}}(i) = E^{\gamma} + E^{\gamma}_{\mathrm{recoil}} - E^{e}_{\mathrm{recoil}}(i) - E^{\mathrm{vac,impl}}_{\mathrm{bind}}(i) \tag{3.2}$$

Here, $E^{\mathrm{vac,impl}}_{\mathrm{bind}}$ is the electron binding energy of a bound krypton, related to the vacuum level of an atomic shell i. $E^{e}_{\mathrm{recoil}}(i)$ is the recoil energy of the atom after an electron of shell i has been emitted. This recoil energy is up to 63 meV and 220 meV

for the 9.4 keV and 32.2 keV transition, respectively [53]. The recoil energies after the γ-emissions $E^{\gamma}_{\text{recoil}}$ are equal to 0.6 meV and 7 meV and therefore negligible. The electron binding energy can also be represented as:

$$E^{\text{vac,impl}}_{\text{bind}} = E^{\text{vac,gas}}_{\text{bind}} - \Delta E^{\text{vac}}_{\text{bind}} \tag{3.3}$$

where $\Delta E^{\text{vac}}_{\text{bind}} > 0$ is the solid state correction [57]. Therefore, equation (3.2) can be rewritten to:

$$E^{\text{impl}}_{\text{kin}}(i) = E^{\gamma} + E^{\gamma}_{\text{recoil}} - E^{e}_{\text{recoil}}(i) - (E^{\text{vac,gas}}_{\text{bind}} - \Delta E^{\text{vac}}_{\text{bind}}) \tag{3.4}$$

The correction of $^{83\text{m}}$Kr on HOPG are estimated to (2.4 ± 0.2) eV for the K-32, L-32, and M-32 conversion electrons and (1.9 ± 0.2) eV for N-32 conversions electrons [38]. These corrections are small enough to not expect a significant impact on the electron response measurement.

Another influence on the conversion electron energy could be the binding energy of krypton to graphite. Graphite is build out of layers of a carbon atom hexagons, a so-called honeycomb lattice [36]. The layers have a distance of 3.4 Å [51]. If a neutral noble gas condensates on graphite it is not bound by chemical bonds but only by Van-der-Waals-bonding [36]. Also krypton is mostly in the middle of a carbon hexagon. Therefore, the distance to the graphite's surface is 3.4 Å. The binding energy in this configuration is only 160 meV [14], which is also negligible for the purposes of this work.

Therefore, rubidium evaporated onto graphite is a viable source for non-disturbed conversion electrons from $^{83\text{m}}$Kr [36]. It should be noted, however that even though it is likely that ^{83}Rb will remain in its origin position because of its high reactivity, some diffusion into the graphite might still happen. This could lead to a measurable impact on the energy of the electrons.

The theoretically expected spectrum from $^{83\text{m}}$Kr is shown in figure 3.2. X-ray and conversion electron peaks should not be considered as monoenergetic Gaussian distributed lines. Only γ-ray and conversion electron K-32 peak come from monoenergetic events. The other ones are a superposition of several lines. The energies and intensities of all considered peaks and the contributing lines are given in table 3.1.

3.1.2. Production of Sources

The sources used in this work were produced at the Nuclear Physics Institute Řež/Prague. The ^{83}Rb is created by bombarding a compressed krypton gas with protons. The created rubidium is washed out by water. The elusion efficiency is $\backsimeq 95\,\%$ for ^{83}Rb. Through chemical treatment several tens of µL of a purified

Table 3.1.: Electron and photon lines of the ^{83m}Kr decay. The peaks mostly consist of several lines that are too close to each other and can therefore not be resolved as single lines by the detector. The values are taken from [53].

Peak	Line	Energy [eV]	Intensity per decay [%]
γ	γ	9405.7 ± 0.6	5.5 ± 0.6
K_α	$KX_{\alpha 2}$	$12\,595.424 \pm 0.056$	4.70 ± 0.19
	$KX_{\alpha 1}$	$12\,648.002 \pm 0.052$	9.1 ± 0.3
K_β	$KX_{\beta 3}$	$14\,104.96 \pm 0.11$	0.65 ± 0.03
	$KX_{\beta 2}$	$14\,112.815 \pm 0.080$	1.27 ± 0.05
	$KX_{\beta 1}$	$14\,315.00 \pm 0.24$	0.167 ± 0.006
K-32	K	$17\,824.2 \pm 0.5$	24.8 ± 0.5
L-32	L_1-32	$30\,226.8 \pm 0.9$	1.56 ± 0.20
	L_2-32	$30\,419.5 \pm 0.5$	24.3 ± 0.3
	L_3-32	$30\,472.2 \pm 0.5$	37.8 ± 0.5
M-32	M_1-32	$31\,858.7 \pm 0.6$	0.249 ± 0.004
	M_2-32	$31\,929.3 \pm 0.5$	4.02 ± 0.06
	M_3-32	$31\,936.9 \pm 0.5$	6.24 ± 0.09
	N_2-32	$32\,136.7 \pm 0.5$	0.300 ± 0.004
	N_3-32	$32\,137.4 \pm 0.5$	0.457 ± 0.006

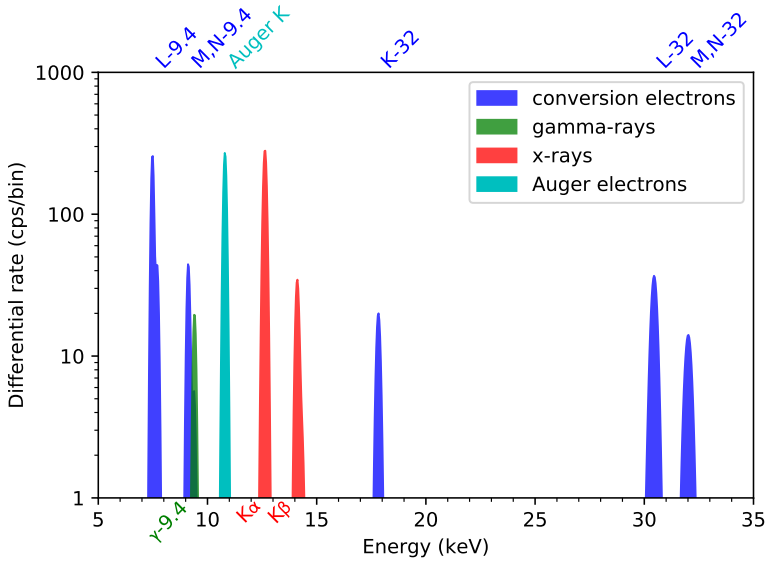

Figure 3.2.: Theoretical spectrum of the photons and electrons created by the ^{83}Rb and consequent ^{83m}Kr decay. Most peaks consist of several electron or photon lines. Taken from [48].

and concentrated ^{83}Rb water solution is obtained. The solution is at first dried and then heated to 200 °C in a vacuum chamber with a pressure of 10^{-5} mbar so that impurities evaporate. After the gaseous impurities are removed, the residual ^{83}Rb is then evaporated by heating it to 800 °C for about one minute. Through a suitable mask the rubidium forms a circle with 12 mm diameter [58]. In this work the backing of the rubidium is either Highly Oriented Pyrolithic Graphite (HOPG) or rigid graphite. The vacuum-evaporation efficiency of rubidium is around $5-30$ %. The retention factors are different for the two backings. It is 7.3 % for HOPG and 30 % for rigid graphite. This factor describes how much of the weakly bound noble gas ^{83m}Kr stays inside the source before decay. The rest is spontaneously released from the source into the vacuum which is then lost due to constant pumping.

The ^{83}Rb activities of the sources were 6.7 MBq for HOPG and 7.9 MBq for rigid graphite on the date of production. This corresponds to about 0.5 monolayers of radioactive rubidium [58]. Both sources are inside an aluminium holder.

3.2. Description of Experiment

3.2.1. Measurement Idea: Tilt-method

To probe the influence of the entrance window on electrons the peak position is examined. Electrons interact nearly continuously with matter and lose energy. Therefore, the energy of the conversion electrons is shifted to lower values with respect to the theoretical values. The position of a peak can be broken down to:

$$\bar{E}^i(\Theta) = \bar{E}^i_{th} - \Delta DL^i(\Theta) - \Phi^{BC} - \delta \tag{3.5}$$

$\bar{E}^i(\Theta)$ is the measured energy position of electron peak i, $\bar{E}^i_{th}$ the theoretical energy, Φ^{BC} the voltage applied to the entrance window of the detector and δ other non-dead layer influences. $\Delta DL^i(\Theta)$ is the energy shift induced by the entrance window. For this characterization the entrance window is assumed to be a sharp edge dead layer. As shown in figure 3.3 the influence of the dead layer is angle dependent. Hence, Θ in equation (3.5) is the angle between the source and the detector. The path electrons travel inside the dead layer increases for larger angles. Therefore, a difference between peak positions of different angles Δ^i_{DL} exists. With equation (3.5) it is shown that the difference Δ^i_{DL} is independent from anything but the dead layer:

$$\Delta^i_{DL} = \bar{E}^i(\Theta_0) - \bar{E}^i(\Theta_1) \tag{3.6}$$

$$= \Delta DL^i(\Theta_1) - \Delta DL^i(\Theta_0) \tag{3.7}$$

$$\text{with:} \quad \Theta_0 < \Theta_1$$

In order to maximize the dead layer effect while not losing too many electrons, due to backscattering, $\Theta_0 = 0°$ and $\Theta_1 = 60°$ were chosen.

3.2.2. Experimental Setup

The general setup of the whole system is the same as described in section 2.3. The detector is placed inside a vacuum chamber onto the holding structure seen in figure 3.4. This structure is attached to a copper plate inside the vacuum chamber. This plate is cooled, using a cooling machine. This feature enables to control the temperature of the detector and therefore to reduce fluctuation coming from temperature dependencies of the SDDs or the ASIC-CUBEs as described in appendix A. The source is fixed on the detector holding structure to ensure the same position relative to the detector in all measurements. Additionally, the detector on the structure can be tilted relative to the source.

In all measurements performed, the detector is maintained at 15 °C and the pressure inside the vacuum chamber is below 5×10^{-5} mbar. The measurement time was about 48 h.

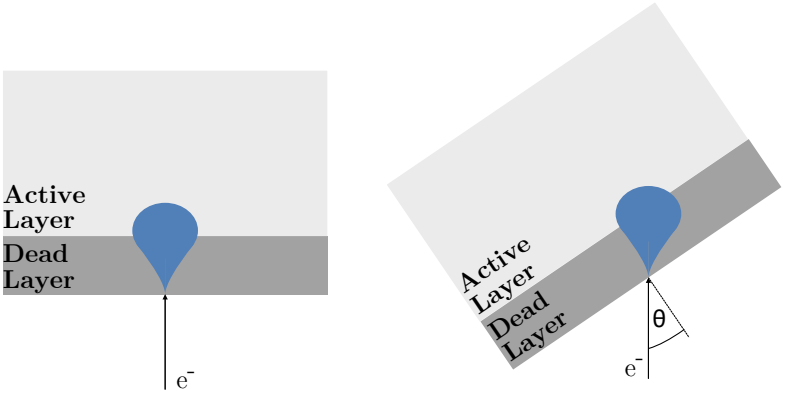

Figure 3.3.: Schematic drawing of a monoenergetic electron beam hitting the detector. Inside the detector the paths of the electrons form a drop like shape. By tilting the detector the effective path length inside the dead layer increases. Thus, less energy is deposited inside the active volume of the detector and the peak position is different.

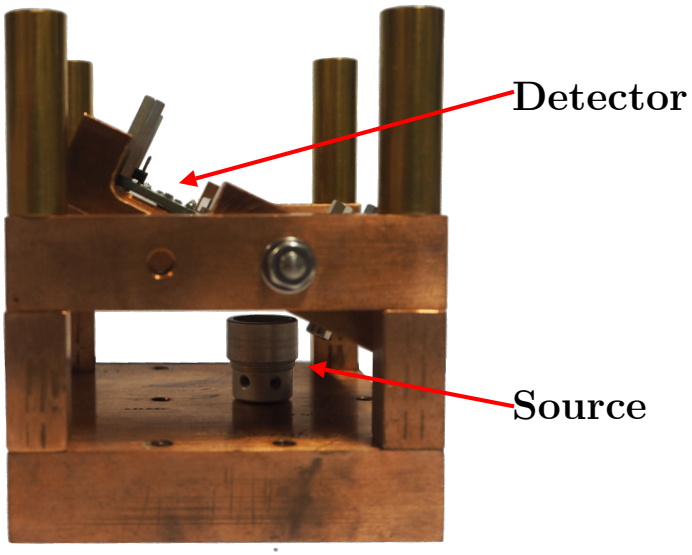

Figure 3.4.: Tiltable holding structure for the detector. Below the SDD chip the source is located.

Table 3.2.: The peaks of ^{241}Am used for calibration of the detectors. Values taken from [32].

Line Name	Energy [keV]
$L_{\alpha 1}$	13.95
$L_{\beta 2}$	16.84
$L_{\beta 1}$	17.75
$L_{\gamma 1}$	20.78
$L_{\gamma 6}$	21.49
XR_1	26.34
γ	59.95

3.2.3. Calibration of the Detector

Before any measurements of the krypton decay are performed the detector is calibrated. This is needed to confirm the proper functionality of the setup and to convert the output of the ADC from channels to units of energy. This is done by using the photon peaks of the ^{241}Am decay. When inside the detector, photons, unlike electrons, interact only once. They deposit all their energy nearly point like. This means, if the interaction happens inside the active volume of the detector, the energy is measured without any losses due to the dead layer. Below the peaks an influence by the dead layer might be seen. This is due to events happening inside the dead layer or very close to it. Then parts of the created charge cloud can be lost [40]. The dead layer is in the order of 100 nm and photons with an energy of 10 keV have a mean free path of roughly 130 µm [45]. Thus, it is much more likely that the interaction happens inside the active volume and the partial events can be neglected for the means of this calibration. Therefore, X-ray peaks can be approximated by Gaussian distributions.

^{241}Am was chosen as calibration source for several reasons. First, it is a radioactive standard, which means that the peak positions are well known. Second, photon peaks with relatively high intensities appear in the range from 13 to 60 keV, which corresponds to our region of interest (see table 3.1). The calibration does not have to be extrapolated which would increase the uncertainty on the calibration.

The ^{241}Am transition lines used in the calibration are shown in table 3.2. The L_β and L_γ lines were fitted with two Gaussian functions because their energies overlap. The other lines were fitted by single Gaussians. The result is depicted in figure 3.5. The correlation of ADC channel to energy is a linear function. The result of one calibration is shown in figure 3.6.

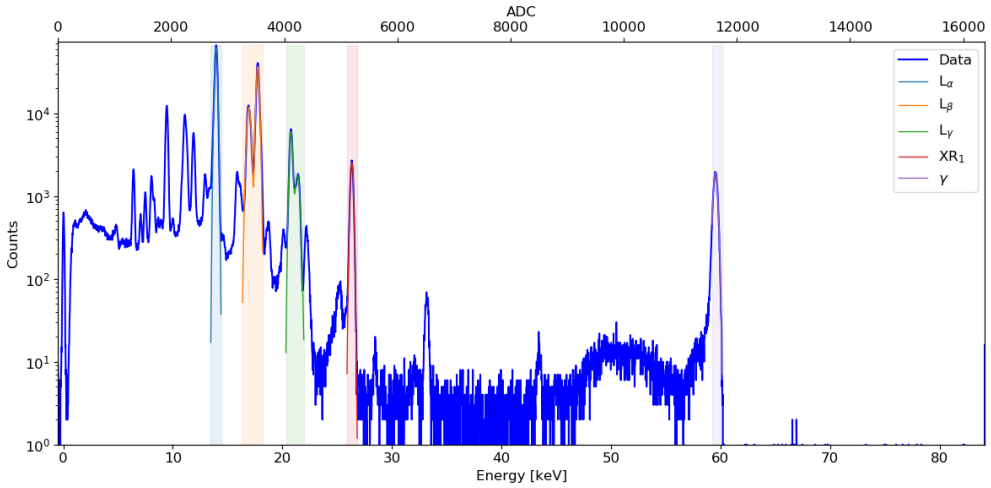

Figure 3.5.: Measured spectrum used for calibration of a detector. The X-ray peaks used for calibration are highlighted by color and their position is fitted by one or two Gaussians.

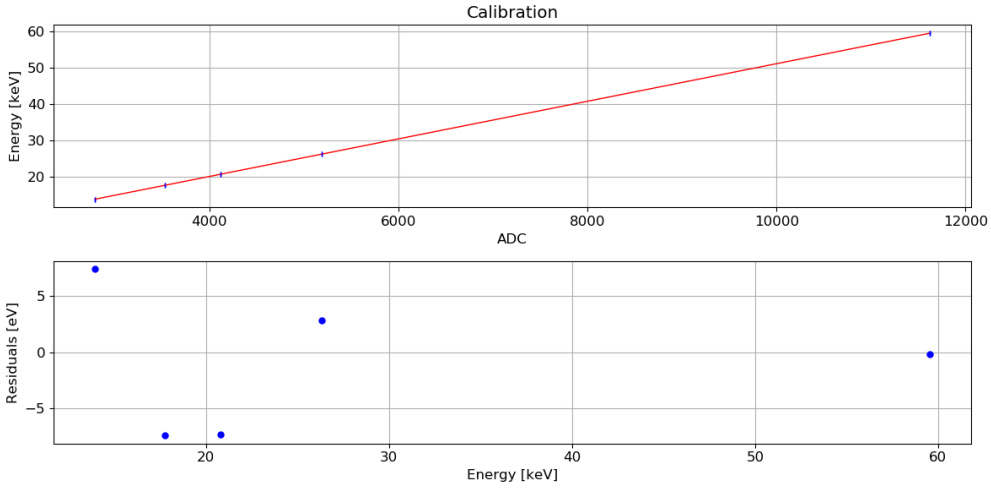

Figure 3.6.: The obtained calibration curve is shown with the estimated peak positions and fit residuals. This measurement was performed with detector S0-1. The slope of the calibration is $(5.1649 \pm 0.0006)\,\mathrm{eV/ADC}$ and the offset is $(-479 \pm 5)\,\mathrm{eV}$.

3.3. Detector Dead Layer Characterization

3.3.1. Analytic Detector Response Function

The analysis of the energy peak positions of photons and electrons of the ^{83m}Kr decay is crucial for the characterization of the dead layer. Therefore, the detector response is an analytical model that is then fitted to data. As photons and electrons behave differently in matter different models had to be used. Only the lines corresponding to the γ-9.4, K_α, K_β, K-32, L-32, and M-32 peaks are used in the analysis.

Photon Response

The analyzed photon can be described as a combination of a Gaussian, a linear function, and a step function as described in equations (3.8) to (3.10). The model is then adjusted to the peaks.

$$G(E) = A_G \exp\left(-\frac{(E-E_0)^2}{2\sigma^2}\right) \tag{3.8}$$

$$L(E) = mE + t \tag{3.9}$$

$$S(E) = A_S\left(1 - \mathrm{erf}\left(\frac{E-E_0}{\sqrt{2\sigma^2}}\right)\right) \tag{3.10}$$

$G(E)$ is a Gaussian with amplitude A_G, mean E_0 and width σ. $L(E)$ is a linear function with slope m and offset t and $S(E)$ is a step function with amplitude A_S, mean E_0 and width σ.

The γ-9.4 peak is the easiest to describe. It is only a single photon line. Therefore, the model of this peak consists of a Gaussian for the photon distribution and a linear function for the background (see equation (3.11)). An example is shown in figure 3.7.

$$P_\gamma(E) = G(E) + L(E) \tag{3.11}$$

The K_α and K_β X-ray peaks consist of two and three photon lines, respectively. Thus, equation (3.12) is used for modeling the response. Whereby i stands for the lines in one peak. I_i is the relative intensity of line i and I_{tot} is the sum of all intensities in a peak. The step function is needed because of the slight asymmetry in the peak coming from events that deposit energy close to the entrance window and are therefore partially lost. The models are depicted in figure 3.8.

$$P_{K_{\alpha/\beta}}(E) = \sum_i \frac{I_i}{I_{tot}} G(E - \Delta E_i) + S(E) \tag{3.12}$$

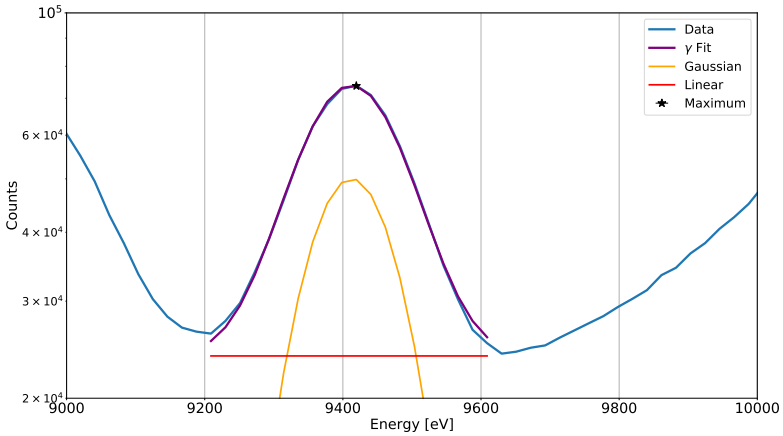

Figure 3.7.: Fit of a γ-9.4 peak with the model described in equation (3.11). The peak consists of one γ-photon line.

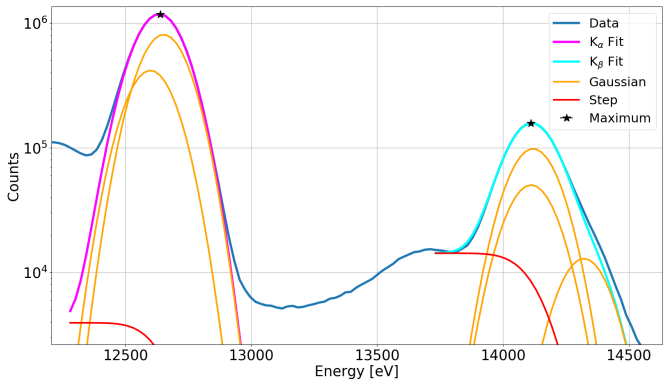

Figure 3.8.: K_α and K_β X-ray peaks fitted with the model described in equation (3.12). The peaks are superpositions of two and three photon lines that are too close together to be resolved by the detector.

Electron Response

The electron response model used in this thesis is shown in equation (3.14) [16].

$$\lambda_i(E_i) = G(E_i) + S(E_i) + D(E_i) \tag{3.13}$$

$$P_{e^-}(E) = \sum_i \frac{I_i}{I_{tot}} \lambda_i(E) + C \tag{3.14}$$

$$D(E) = A_D \exp\left(\frac{E - E_0}{\beta}\right)\left(1 - \mathrm{erf}\left(\frac{E - E_0}{\sqrt{2\sigma^2}} + \frac{\sigma}{\sqrt{2}\beta}\right)\right) \tag{3.15}$$

$\lambda_i(E_i)$ describes one conversion electron line i consisting of one Gaussian (equation (3.8)), a step function $S(E_i)$ (equation (3.10)) for the slight asymmetry of the peaks and a diffusion term $D(E_i)$ (equation (3.15)) for the low energy tail. I_i is the relative intensity of line i and I_{tot} is the sum of the intensities.

Also a constant background C is assumed in the model. The L-32 and M-32 peaks consist of several electron lines $\lambda_i(E_i)$. Finally the result of these fits are shown in figure 3.9.

3.3.2. Analysis of Measurements

For fitting the model to the data the python function *scipy.optimize.minimize* [54] was used. It utilizes the least square method to find the best fit values. To reduce the number of free parameters, the relative position between the lines and the intensities were taken from theoretical values in table 3.1, when necessary. Also a constant line width within one peak is assumed. The resulting free fit parameters for each peak are given in table 3.3.

For every energy bin a Poissonian error is assumed. The position of a peak is defined by the maximum of the peak's fitted function. The maximum of the fitted peak function is assumed to be less model dependent than the mean of the Gaussians. The uncertainties were calculated following the procedure shown in appendix B.1.

The photon peaks were only fitted within their Full Width Half Maximum (FWHM).

For the different measurements, the peak positions are given in tables 3.4 and 3.5. One possible way of estimating the goodness of a fit is the reduced χ^2, which is shown in table 3.6. It is defined as the χ^2 per degree of freedom. The χ^2 is a sum of squared deviations weighted by the data's uncertainty σ. The degrees of freedom is

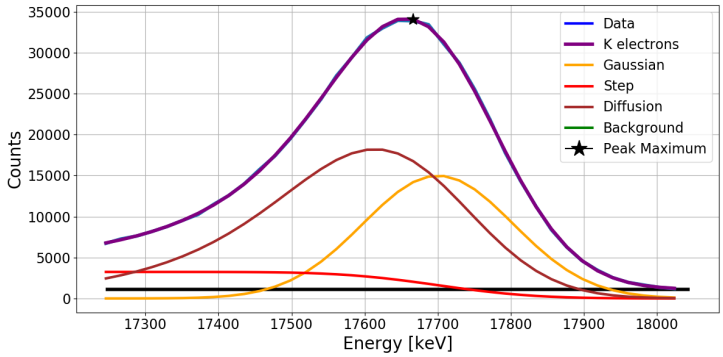

(a) Fit of the electron K line.

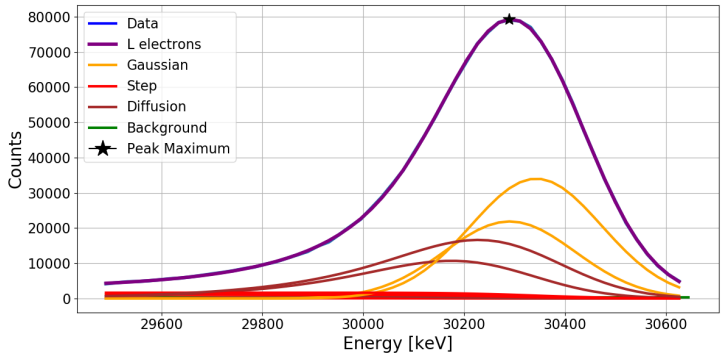

(b) Fit of the electron L lines.

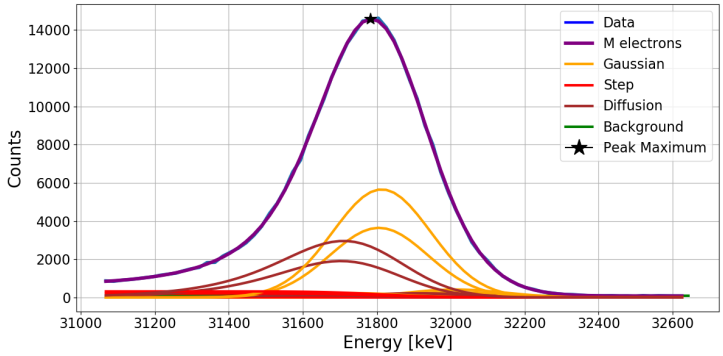

(c) Fit of the electron M lines.

Figure 3.9.: Fit of the response model for electron peaks to data. The measurement was performed with detector R0-2 without tilting. The K-32 peak consists only of one conversion electron line, while the L-32 and M-32 peaks consist of several lines that are too close to be resolved by the detector.

Table 3.3.: Free parameters depending on the nature of the entering particle.

Peak	Fit Parameters
Photon γ	One Gaussian mean μ and width σ Background slope m and offset t
Photon $K_{\alpha/\beta}$	One Gaussian mean μ and width σ
Electron K-32, L-32, M-32	One Gaussian mean μ and width σ Diffusion term β Constant background C

the number of data points n reduced by the number of free parameters in the fit m:

$$\chi^2 = \sum_i \left(\frac{\text{data}_i - \text{model}_i}{\sigma_i} \right)^2 \tag{3.16}$$

$$red.\,\chi^2 = \frac{\chi^2}{dof}, \quad dof = n - m \tag{3.17}$$

As a rule of thumb, the model fits the data well if the reduced χ^2 is around 1.

For the photon peaks the reduced χ^2 is, in general, larger than one. In the case of the γ-9.4 peak, this could be because it is between two electron peaks that distort the peak. This distortion might not be described by a simple linear function, but if a more complex function was used as background the fit would not converge. In the K_α and K_β peak models the background was neglected. This would then also result in a worse fit. The theoretical energy of the peaks are $(9405.7 \pm 0.6)\,\text{eV}$ for γ-9.4, $(12\,630.1 \pm 0.6)\,\text{eV}$ for K_α, and $(14\,126.5 \pm 0.7)\,\text{eV}$ for K_β. The discrepancies between the measured values and the theoretical ones is most likely due to the binning. One energy bin is about 20 eV wide. Therefore, the binning could distort the peak slightly

The positions of the electron peaks are lower than the theoretical values. For detector R0-2 the reduced χ^2 values are all around one. This shows that here the model fits the data very well. In the case of S0-1 the value is between 1.8 and 2.6. This could be due to a stronger electron tail in this detector. The model is designed for a peak that is mainly described by a Gaussian function and a step function as tail correction. If the tail is too pronounced the model's transition between tail and Gaussian might not describe the data accurately.

The results of the fit show that the model described in section 3.3.1 is capable of accurately describing the electron peaks.

Table 3.4.: Maximum of the photon peaks. The measured peak positions are compatible with the theoretical values.

Detector/ Tilting	γ-9.4 [eV]	K_α [eV]	K_β [eV]
S0-1 0°	9420.5 ± 0.1	$12\,638.0 \pm 0.1$	$14\,118.2 \pm 0.1$
S0-1 60°	9419 ± 4	$12\,634.6 \pm 0.1$	$14\,113.8 \pm 0.1$
R0-2 0°	9413.1 ± 0.2	$12\,636.9 \pm 0.1$	$14\,114.8 \pm 0.1$
R0-2 60°	9413.2 ± 0.7	$12\,637.8 \pm 0.1$	$14\,116.6 \pm 0.1$

Table 3.5.: Maximum of the conversion electrons peaks for the different detectors at different tilting angles.

Detector/ Tilting	K-32 [eV]	L-32 [eV]	M-32 [eV]
S0-1 0°	$17\,588.3 \pm 0.2$	$30\,255.9 \pm 0.1$	$31\,747.0 \pm 0.1$
S0-1 60°	$17\,456.6 \pm 0.7$	$30\,165.6 \pm 0.5$	$31\,663.6 \pm 0.8$
R0-2 0°	$17\,656.6 \pm 0.3$	$30\,292.8 \pm 0.2$	$31\,785.4 \pm 0.1$
R0-2 60°	$17\,611.1 \pm 0.7$	$30\,260.8 \pm 0.2$	$31\,757 \pm 2$

Table 3.6.: The reduced χ^2 value for the fits of the ^{83m}Kr decay peaks.

Detector/ Tilting	γ-9.4 [eV]	K_α [eV]	K_β [eV]	K-32 [eV]	L-32 [eV]	M-32 [eV]
S0-1 0°	8	4.6	2.3	2.4	1.8	2.5
S0-1 60°	6.7	2.1	1.8	2.6	2.2	2.1
R0-2 0°	2.9	2.4	1.8	1.0	1.1	1.0
R0-2 60°	1.1	1.7	1.1	1.2	1.1	1.0

3.3.3. Analysis of Results

With the obtained peak positions the dead layer of the detectors can be analyzed. For this the dead layer shifts Δ^i_{DL}, described in section 3.2.1, are calculated by equation (3.7) for both detectors and all three electron peaks. Δ^i_{DL} is shown in table 3.7 and figure 3.10. The shift decreases with increasing electron energies, which results from the longer mean free path for higher energy electrons.

Table 3.7.: Dead layer shifts Δ^i_{DL} for detectors S0-1 and R0-2.

Shift	S0-1 [eV]	R0-2 [eV]
Δ^K_{DL}	131.4 ± 0.9	45.2 ± 0.8
Δ^L_{DL}	90.9 ± 0.2	32.6 ± 0.3
Δ^M_{DL}	84.2 ± 0.8	29 ± 2

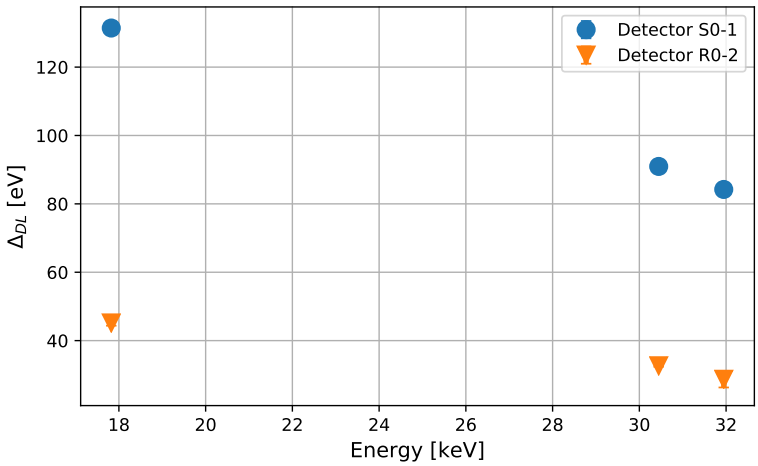

Figure 3.10.: Dead layer shifts Δ^i_{DL} for detectors S0-1 and R0-2. The decreasing shifts are due to the increase of the mean free path for higher energies. The uncertainties are too small to see.

3.3.4. Conclusion

The dead layer shifts obtained with the conversion electrons of ^{83m}Kr can be compared to the shifts measured previously using a scanning electron microscope as monoenergetic electron source [47]. The electron beam energy used there was 14 keV. This is comparable to the 17.8 keV of the conversion electron K-32 peak

of the metastable krypton decay. The shifts measured there were (45 ± 1) eV for the R0-2 and (108 ± 4) eV for the S0-1 detector. Both measurement techniques, krypton and electron microscope, give compatible results. This shows that the energy shift measurement with krypton is a viable method to measure these shifts. Both methods can therefore be used to crosscheck each other.

3.4. Dead Layer Thickness Determination

3.4.1. Simulation Setup

To translate the observed shift in the line position into an effective dead layer, a GEANT4 simulation was performed. For the determination of the thickness of a sharp edge dead layer Monte-Carlo-simulations of particle transport and interactions with Geant4 are used. The setup of the simulations consist of a source and a detector. The placing and composition of the components is similar to the measurements (see figure 3.11). The source is composed of a 10 nm layer of ^{83}Rb on top of graphite. This is inside an aluminium holder and is placed at a distance of 1 cm to the detector. The detector consists of a silicon cylinder with a diameter of 2 mm and a thickness of 400 µm. On the side facing the source the detector has a 10 nm thick layer of SiO_2. In the first simulation the source and the detector are parallel. In the second simulation the source is tilted 60° to the detector. In this tilted configuration electrons might enter the silicon directly at the side of the detector in a much higher rate than in the 0° configuration. This would alter the peak positions. An additional ring of silicon and silicon oxide of 1 mm is set around the actual detector to prevent this undesired effect.

For the 0° simulation 10^8 rubidium decays were simulated. For 60° twice as many decays were generated to compensate the reduced rate on the detector. A real detector has an energy resolution. This needs to be added before analyzing the peaks. To take this into account the energy spectrum is convoluted with a Gaussian distribution. The width of this distribution is given by:

$$\sigma = \sqrt{F \cdot \omega E + \sigma_{el}^2} \tag{3.18}$$

F is the Fano factor which is equal to 0.125 in silicon [37]. $\omega = 3.64$ eV is the energy needed to create electron-hole-pairs in silicon at 20 °C [37]. $\sigma_{el} = 33$ eV is the electronic noise of the system [47].

During the simulations no dead layer apart from the silicon oxide was added to the entrance window of the detector. A sharp edge dead layer is added in later analysis. The thickness of the whole dead layer was varied from 20 to 200 nm in steps of 10 nm.

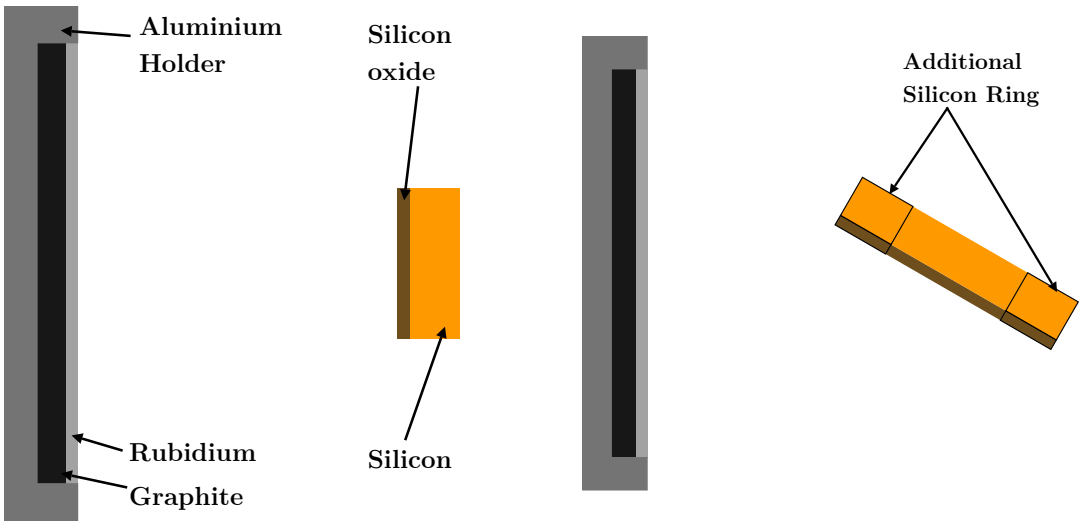

Figure 3.11.: Setup of the Geant4 simulations. *Left:* Simulation at 0°. *Right:* Simulation at 60° with additional ring to prevent direct hits of the detector.

3.4.2. Simulation Results

In figure 3.12 the spectrum of the untilted simulation and a dead layer thickness of 50 nm is compared to the spectrum obtained with detector R0-2. The counts have been normalized to the amplitude of the K_α peak. The different peak heights come from different retention factors. The electron peaks K-32, L-32, and M-32 have similar shapes in simulation and measurement. One crucial point is that photon peaks do not align. This comes from outdated transition energies inside the used Geant4 libraries. The values for the conversion electrons inside the libraries are similar to the ones shown in table 3.1.

The energy shifts Δ^i_{DL} of the simulations are shown in figures 3.13 to 3.15. The shifts are calculated with equation (3.7). The energy shift as a function of the dead layer is described by a polynomial of first degree.

3.4.3. Dead Layer Thickness Conclusion

The dead layers of the two detectors can be determined by comparing the simulation with the measurements. The results are shown in table 3.8. As expected from the energy shift measurements, detector S0-1 has a much larger dead layer than R0-2. However, such a dead layer thickness is not expected for S0-1. Similar simulations performed using KESS instead of Geant4 showed different results [47]. In this case, for similar observed energy shifts, a dead layer of (94 ± 7) nm was found for S0-1 and (46 ± 6) nm for R0-2 which is not in agreement to the simulations results of

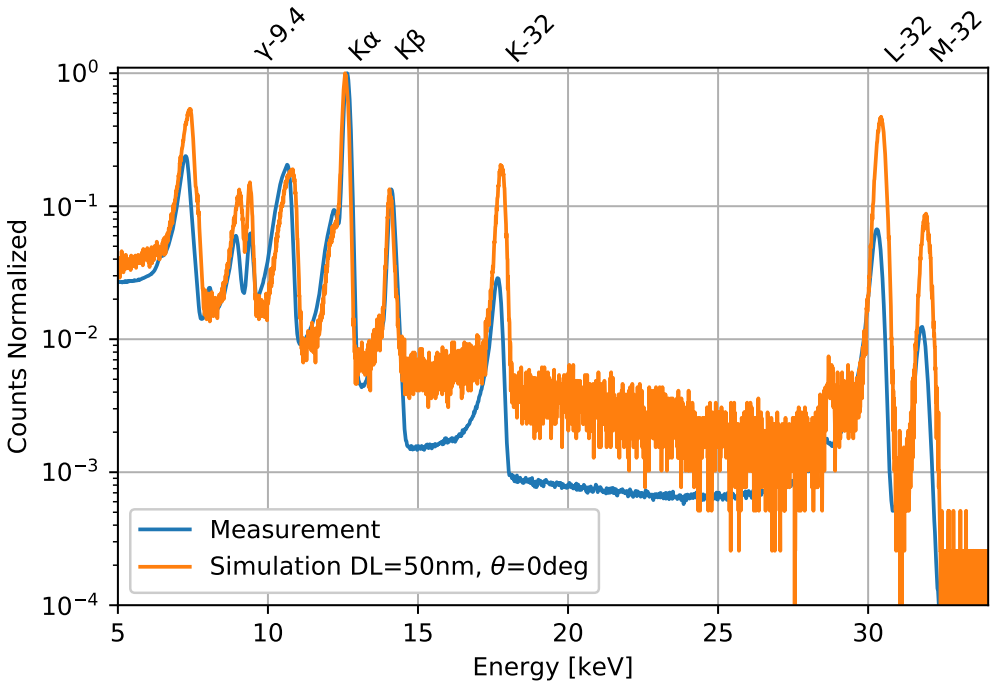

Figure 3.12.: The spectra from ^{83m}Kr decay of the untilted simulation with a 50 nm dead layer and of detector R0-2. The counts are normalized to the amplitude of the K_α peak.

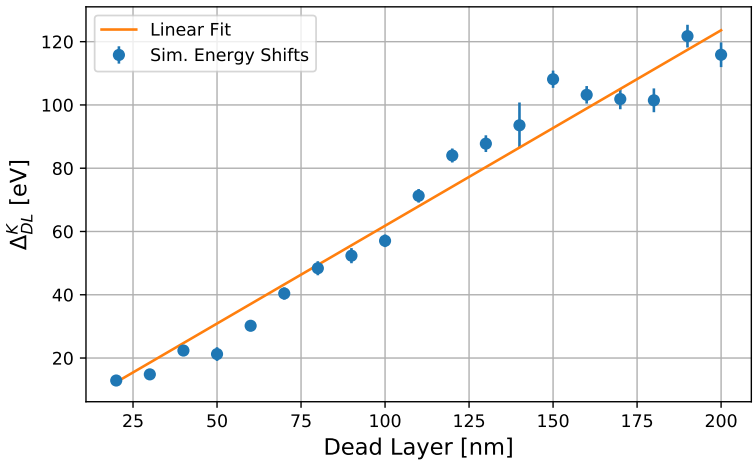

Figure 3.13.: Shift in energy between tilted and untilted simulation as a function of the dead layer for the K-32 conversion electrons. A linear function is used to approximate the energy shift increase for increasing dead layer thicknesses. The slope is $(0.618 \pm 0.004)\,\mathrm{eV\,nm^{-1}}$ and the offset $(0 \pm 8) \times 10^{-5}\,\mathrm{nm}$.

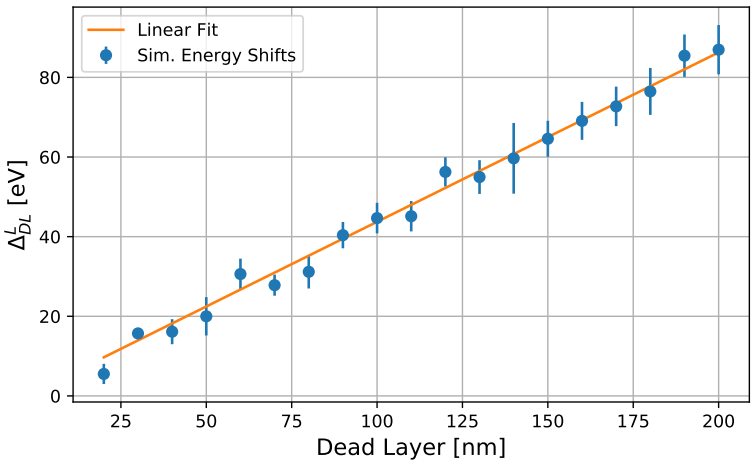

Figure 3.14.: Shift in energy between tilted and untilted simulation as a function of the dead layer for the L-32 conversion electrons. A linear function is used to approximate the energy shift increase for increasing dead layer thicknesses. The slope is $(0.43 \pm 0.01)\,\mathrm{eV\,nm^{-1}}$ and the offset $(1.2 \pm 0.9)\,\mathrm{nm}$.

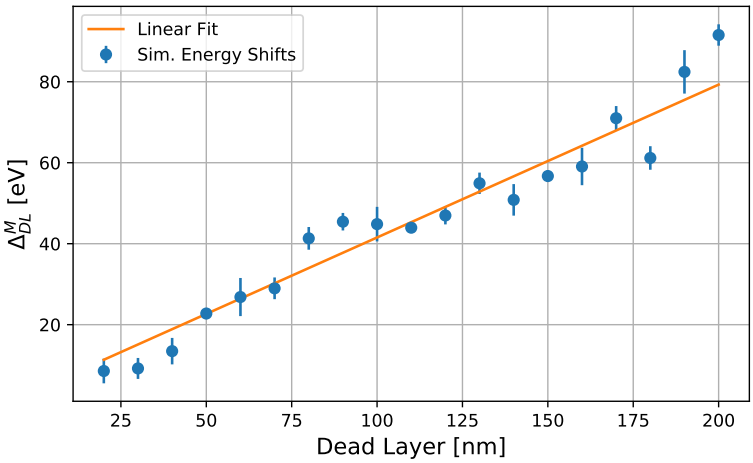

Figure 3.15.: Shift in energy between tilted and untilted simulation as a function of the dead layer for the M-32 conversion electrons. A linear function is used to approximate the energy shift increase for increasing dead layer thicknesses. The slope is $(0.378 \pm 0.006)\,\mathrm{eV\,nm^{-1}}$ and the offset $(3.8 \pm 0.4)\,\mathrm{nm}$.

GEANT4 obtained in this work. This highlights the need of further investigations into both simulation software.

Table 3.8.: Results of dead layer measurement by comparing data and simulation. The dead layer is given for both detectors for each of the three conversion electron peaks. The uncertainty propagation is described in appendix B.1.

Peak	Energy	S0-1	R0-2
K-32	17.8 keV	(212 ± 2) nm	(73 ± 2) nm
L-32	30.4 keV	(210 ± 4) nm	(74 ± 2) nm
M-32	31.9 keV	(213 ± 3) nm	(65 ± 4) nm

3.5. Source Influence on the Energy Shift

In this chapter, the absolute measured line position to the theoretical prediction for an untilted detector is compared. The information on the dead layer (section 3.3), allows to make a statement on the energy loss of the electrons in the source. Two sources were available for performing measurements. The first is rubidium evaporated onto HOPG and the second rubidium evaporated onto rigid graphite. The spectra for both sources shown in figure 3.16 are obtained with an untilted detector. Both spectra are normalized to the amplitude of the X-ray K_α peak. The different spectra show that the rigid graphite source has a clearly visible source effect. In HOPG the electron peaks are much more pronounced and much less electron background is present. This can be seen in the energy range of 18 to 30 keV. A measurable source effect on the electrons might also be possible for the HOPG source.

To examine this, the results from section 3.3 and equations (3.5) and (3.7) are used. For extracting the source effect δ, it is assumed that the effective dead layer at a tilting angle Θ increases for electrons by a factor of $\frac{1}{\cos\Theta}$. Therefore, at a tilting angle of 60° the dead layer shift is doubled compared to 0°. δ can then be determined using equation (3.5):

$$\Delta^i_{DL} = \Delta DL^i(60°) - \Delta DL^i(0°) \tag{3.19}$$

$$\text{with:} \quad \Delta DL(60°) = 2\Delta DL^i(0°) \tag{3.20}$$

$$\Rightarrow \delta = \bar{E}^i_{th} - \bar{E}^i(\Theta) - \Delta^i_{DL} - \Phi^{BC} \tag{3.21}$$

The results for the source effect in the measurements of both detectors is shown in figure 3.17. By construction the same result is obtained for the tilted measurements. In both detectors the source shift is energy independent and not zero. The mean of

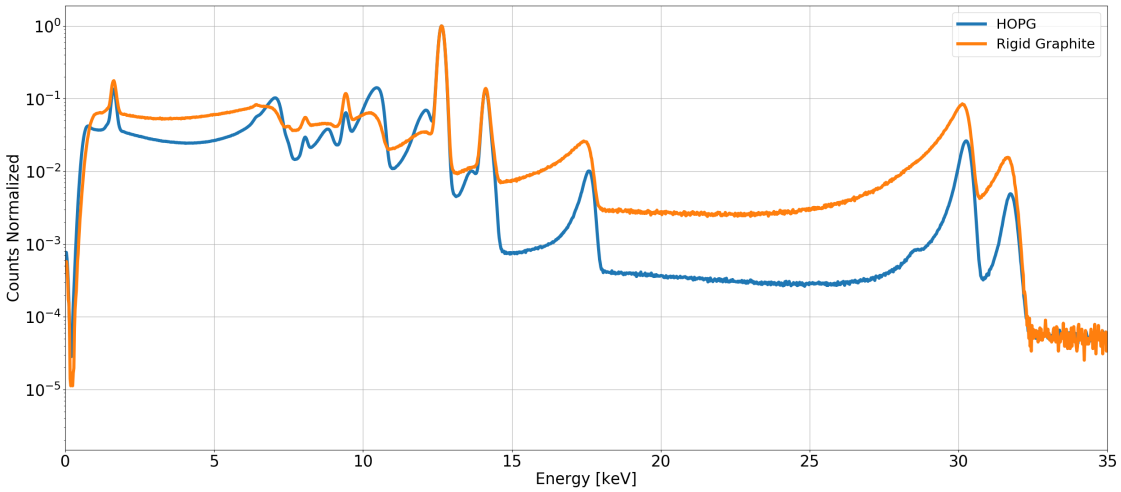

Figure 3.16.: Comparison of the spectra obtained from the decay of ^{83m}Kr in the HOPG and the rigid graphite source. It is visible that rigid graphite alters the electrons significantly.

the shift is (16.0 ± 0.6) eV for detector S0-1 and (35 ± 1) eV for R0-2. This should be the same as it is assumed to be a effect not coming from the detector. An explanation for the discrepancy might be the assumption that the dead layer effect increases by a factor $\frac{1}{\cos(\Theta)}$ is worse for S0-1 than for R0-2. In the detector S0-1 the dead layer is much bigger than in R0-2. Therefore, through random scattering in the material fewer electrons travel straight or nearly straight through the dead layer. At a certain point the assumption is not applicable anymore. For R0-2 this is less problematic as the dead layer shift is approximately one third of S0-1. Thus, more electrons can travel straight through the dead layer.

The dead layer and back contact potential were already taken into account for the extraction of δ. One possible explanation for this shift is that the back contact potential, which is set to -90 V at the bias board is not the same voltage at the detector. Another origin of the additional shift could be the source. Through unintentional mishandling or storing the source in air and not in vacuum the surface is altered which would lead to different working function. Further investigations need to be done to find the origin of this source effect.

3.6. Conclusion

In this work a dead layer characterization of the TRISTAN detectors was performed. Two TRISTAN prototype detectors, S0-1 and R0-2, were characterized. Tilting the detectors artificially increases the dead layer and a different energy shift can

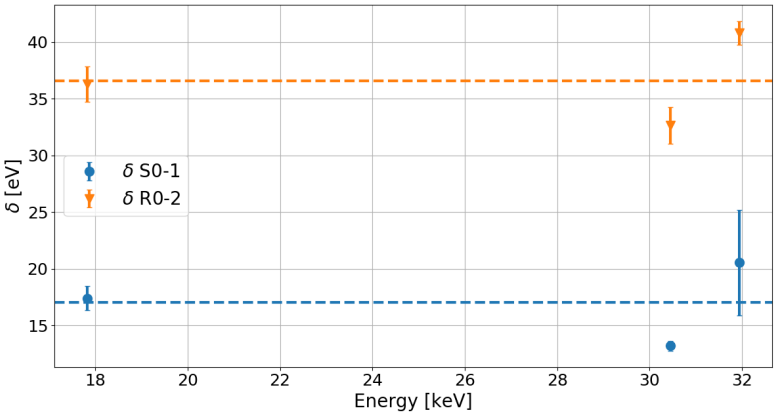

Figure 3.17.: Source effect δ for both detectors. This is obtained by assuming that the dead layer doubles at a tilting angle of 60° compared to no tilting.

be measured. The relative shift between two angles is independent of external potentials or theoretical values. The monoenergetic conversion electrons created in the 32 keV de-excitation of metastable ^{83m}Kr were used for the measurements. The origin of the isomeric krypton was the decay of ^{83}Rb through electron capture. Evaporated ^{83}Rb on Highly Oriented Pyrolithic Graphite was used as solid source. It has been demonstrated that this kind of source should not have an influence on the electron energy.

The shifts measured for a tilting of 60° compared to 0° are (130.0 ± 0.9) eV for S0-1 and (43.6 ± 0.8) eV at an electron energy of 17.8 keV. For higher energies these shifts are lower because of the longer mean free path.

After the shifts measurement, Geant4 simulations were performed to relate the shift to a dead layer thickness. For this, two simulations, with and without tilting the detector, were performed. Afterwards, the energy shifts of the electron peaks between the two simulation was determined for different dead layers thicknesses. Comparing these simulations with measurements the dead layer thicknesses were estimated to be (210 ± 2) nm for S0-1 and (70 ± 2) nm for R0-2 at 17.8 keV.

These can be compared to the dead layer results of KESS simulations estimating the dead layers to be (94 ± 7) nm for S0-1 and (46 ± 6) nm for R0-2 at 14 keV. This discrepancy can only result from the different simulation programs as the energy shifts in both measurements were similar. This demonstrates how complex it is to relate a dead layer shift to a thickness. Further investigations into the differences between Geant4 and KESS need to be done.

Finally, two krypton sources with different substrates (HOPG or rigid graphite) were compared - the spectrum coming from the rigid graphite source had higher electron background and thus much broader peaks than the spectrum obtained

with HOPG. This proves the need to extract a source influence on the absolute energy shifts from the theoretical value, measured with the detector tilting method. Taking the back contact potential into account and assuming that the dead layer shift increases with $\frac{1}{\cos(\Theta)}$ a source influence is extracted. This influence is energy independent in both detectors and was estimated to be $(16.0 \pm 0.6)\,\mathrm{eV}$ for detector S0-1 and $(35 \pm 1)\,\mathrm{eV}$ for R0-2. This discrepancy is most likely due to the assumption of the doubled shift at 60° tilting. Still it shows that a source effect exists. To find the origin of these shifts, a more detailed study needs to be conducted. One possible next step is to apply the back contact potential also to the $^{83\mathrm{m}}$Kr source. This would exclude a false assumption of the potential as possible explanation.

4. Epitaxy Entrance Window pin-Diodes

A major requirement for the TRISTAN detector is a thin entrance window. It improves the energy resolution, lowers the energy threshold and most importantly, make the experiment less sensitivity to uncertainties in the description of the entrance region of the detector. One of the most common ways to create a doped region in a semiconductor is via ion implantation. This method is applied in the production of the TRISTAN prototype chips at the Halbleiterlabor of the Max-Planck-Society (MPG HLL). Another way of creating a doped layer on the substrate is molecular beam epitaxy. The subject of this chapter is a first feasibility study to find out if molecular beam epitaxy might be a viable technology for future TRISTAN detectors. Several wafers with implanted and epitaxy pin-diodes were produced. In the first part of this chapter the two doping technologies are explained. Then, the prototype diodes' wafers are described. Afterwards, the measurements of two diode properties, leakage current and efficiency, are shown and discussed. In the end a conclusion is given about the viability of molecular beam epitaxy for the production of TRISTAN detectors.

4.1. Doping Technologies

4.1.1. Ion Implantation

Ion implantation is a technique for doping a semiconductor. It has been developed and refined for over thirty years [26]. Ion implantation is a standard way of creating semiconductor detectors at the MPG HLL. In this process, the semiconductor substrate is bombarded by dopant ions in the energy range of keV to MeV. After implanting, the substrate needs to be annealed. This incorporates the dopant atoms into the lattice [33]. With this technique, a doping profile is created inside the substrate that can be several µm thick.

This is a very delicate way of doping, but has several disadvantages. For one, the doping is introduced into the silicon bulk. This can influence the potential distribution inside the detector. It can also introduce impurities into the silicon

and create crystal defects, which increases the noise of the detector. An additional disadvantage is the diffusion during annealing, which makes it hard to control the distribution of dopants [26].

4.1.2. Molecular Beam Epitaxy

Epitaxy describes crystal growth techniques, in which thin films with crystalline structures are grown onto a crystalline substrate. These epitaxial layers have a well-defined orientation with respect to the substrate's crystal. This technique also allows to have different lattice parameter and composition in the layer than in the substrate [39]. Molecular beam epitaxy is a method developed in the 1960s and early 1970s [41]. It can be described as a form of vacuum evaporation where material purity, doping concentrations, interface formation and alloy compositions are controlled extremely well. A setup of molecular beam epitaxy (MBE) is shown in figure 4.1. The setup consists of vapor sources, a vacuum chamber, a substrate, and a Reflection High-Energy Electron Diffraction (RHEED) gun. The molecular beams are created inside the sources either by effusion or by electron sputtering. For effusion a crucible with ultra pure material is heated until the material sublimates and becomes gaseous. For electron sputtering, high energy electrons are to transfer kinetic energy to atoms bound in a solid. If the transferred energy is greater than the binding energy, the atom leaves the solid. Both source types create highly pure vapors. The gasses typically have pressures of 10^{-7} mbar. The pin-diode described here are produced with electron sputtering sources. The vapors enter the ultra high vacuum chamber and hit the substrate. Because of their low pressures the vapors' mean free paths are much longer than the 20 to 30 cm from source to substrate.

Epitaxial growth only happens if non-interacting molecular or atomic beams interact chemically with the substrate. For this an activation energy is needed. So, the substrate itself is heated to several hundred Kelvin. Factors like the doping concentration or the growth rate highly depend on the flux of the constituent species. To control this flux of the different vapors fast shutters are in front of every source. To reduce impurities from background gasses their partial pressures inside the chamber are reduced to 10^{-14} mbar. To increase the homogeneity and reduce any angular dependencies the substrate is rotated during the growth process.

To monitor growth in-situ Reflection High-Energy Electron Diffraction (RHEED) is used. Electrons with energies of up to 20 keV are directed at very low angles (1° to 3°) towards the substrate. There they are reflected and then detected on a screen. Because of the low angles the electrons scatter mostly elastically from the surface and are therefore very sensitive to surface changes. On the screen, a pattern changing with the growth of the epitaxial layers is created. Thus, the growth rate and surface structure can be determined [41].

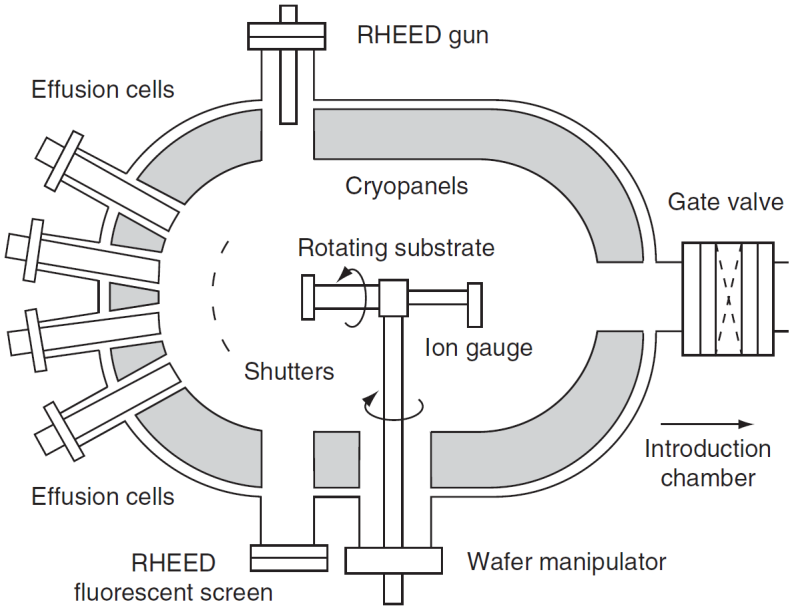

Figure 4.1.: Schematic diagram of MBE growth chamber. In the effusion cells an ultra-pure vapor is created. This enters the vacuum chamber and grows onto the heated substrate. The substrate is rotating to remove any angular dependencies. RHEED is used to monitor the growth of the layer in-situ. The concentration of the epitaxial layer is dependent on the composition and flux of the incoming vapors. Taken from [17].

This form of doping does not have the disadvantages of ion implantation, because here the dopants are grown onto the silicon and are not introduced into the bulk.

The epitaxy process is done by the Institute of Semiconductor Engineering of the University of Stuttgart.

4.2. Prototype Wafers

Twelve wafers featuring 133 pin-diode each were produced. Except for one wafer, all were treated mostly the same way. In the last wafer a different oxidation technique was used. The difference between the other wafers are different cleaning steps and tempering temperatures. The layout of diodes was the same on all wafers and is shown in appendix C. The whole wafer was at first n^+ doped using ion implantation to create the anode of the diode. On each wafer, both implanted and Epitaxy diodes were produced. The produced diodes have areas of 0.1, 1 and 5 cm^2. For the implanted ones, different production techniques have been used. For this thesis the following naming scheme for the relevant technologies and diodes is introduced:

- **Epitaxy**
  Diodes where the doping on the entrance window was done by MBE.
- **Standard thin**
  During ion implantation no silicon oxide layer was on the diodes and the beam hit the silicon directly.
- **Standard thick**
  During ion implantation a silicon oxide layer was on top of the diode, through which the implantation was done. This layer was not removed afterwards. Therefore, they have a thick layer of SiO_2.
- **-COV**
  This indicates that after doping an additional protective layer was put onto the diodes. This was done to shield them from damage during further production steps. This was removed in the end of wafer processing.

It is important to note that the Epitaxy and Standard thin diodes have a small SiO_2 layer as well, which grows when silicon reacts with oxygen in air. It is around 2 to 3 nm thick.

All diodes also have a guard ring that prevents electrons from leaving to or entering from the sides. The working principle is illustrated in figure 4.2. It is a p^+ doped region and thus works the same way as the diode. It depletes the volume of the wafer between itself and the anode. Thereby, it also creates an electrical field. Holes entering this field are attracted to the guard ring and electrons to the anode. At low voltages the ring's field does not cover the whole depth of the wafer. Hence, charges are still able to enter the diode. With increasing voltages the volume covered by the field gets bigger and fewer charges can enter the diode. At a certain potential the guard ring covers the whole depth and no external charges can enter the diode.

4.3. Leakage Current Investigations

A pin-diode is in principle a pn-junction as described in section 2.1.2. In reverse-bias configuration, no current should flow through the diode. In reality, a usually very small leakage current is flowing through the depletion region. It comes from the minority charge carriers. In the p-type part of the diode electrons are the minority and in the n-type the holes are. These minority charge carriers created by defects in the diode diffuse through the depletion region and create a current [24]. This

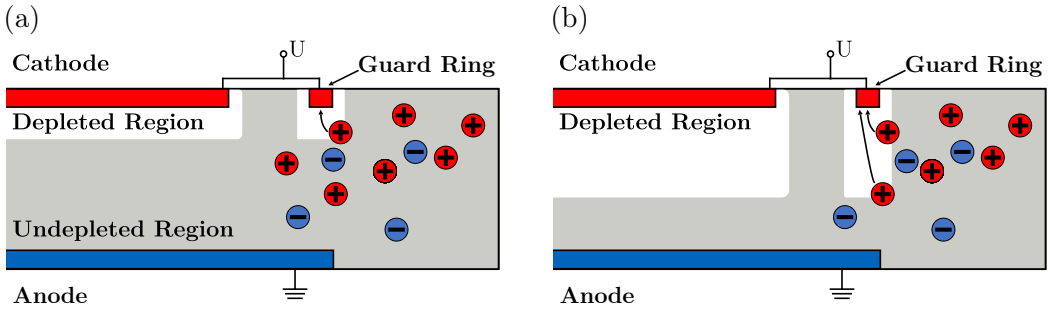

Figure 4.2.: Working principle of a guard ring. The ring depletes the area around it, thereby creating an electrical field. This accelerates holes coming from outside the diode and entering the ring's field. In figure (a) the voltage applied to the ring is too low and therefore the field only covers a small depth of the diode. Many charges can enter the diode beneath the field. Figure (b) shows the situation if the ring covers nearly the whole depth and hardly any charges from outside enter the diode.

is called the Shockley current for reverse bias pn-junctions. The leakage current grows with the volume of depleted material. Also, it is temperature dependent. At lower temperatures fewer minority charge carriers are present in the material. The current is a good parameter to access the diode's functionality. The setup for these investigations is shortly described in the first part of this section. Afterwards, the results are presented and discussed. Also a failure rate of the diodes is calculated.

4.3.1. Leakage Current Setup

Before the wafers were cut the leakage current was measured. For this external voltages were applied to each diode individually and the corresponding current measured. This way an I-V curve can be determined. The schematic of this measurement is shown in figure 4.3.

4.3.2. Measurement Results

The current as a function of the applied voltage was measured in the range of 0 to 150 V in steps of 2 V. Some examples for such curves are shown in figure 4.4.

Most of the diodes do not have the expected increase of leakage current for increasing voltages but decreasing slopes until they reach a plateau. This results from the wafers not being cut before the measurements [44]. On the wafer is a completely non-conductive SiO_2 layer. The crystalline structure of the silicon has a mismatched interface with the unordered oxide. Thus, additional transitions are possible here,

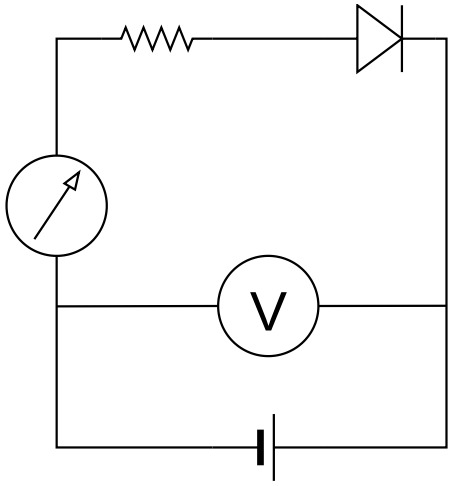

Figure 4.3.: Schematics for the leakage current measurements. By applying voltages the leakage current of the diode can be measured.

that are forbidden in the bulk of the silicon. Without an external voltage applied to the diode, the positively charged oxygen in the molecule accumulates electrons until the interface is saturated and therefore in equilibrium. During processing a wafer is exposed to deionized water and nitrogen gas. In this process electrons can be removed from the SiO_2. As silicon oxide is an insulator, the removal of negative charges leads to static charges across the wafer. Hence, the interface is not in equilibrium anymore and the production of charges is preferred. If a voltage is applied and the diode is depleted the generated electron-hole-pairs enter the silicon bulk. There, electrons diffuse to the anode and are either collected or recombine on the way. In the p^+ bulk close to the interface the excess of holes leads to a much longer life time of holes. This is because an electron has a higher probability to find a hole than vice versa. So, holes are able to travel several cm in the wafer before recombination. Therefore, holes generated somewhere on the wafer can be measured in the diode. This increases the measured current and is not the real leakage current of the diode.

To prevent this from happening each diode has a guard ring. This ring is set on the same potential as the diode. At low potentials the guard ring's field does not cover the whole detector and prevents all external charges from entering. By increasing the applied voltage fewer charges enter the diode and only the diode's own leakage current is measured.

These static charges are randomly distributed across the wafer. It is possible that these charges diminish over time. Therefore, some diodes, like wafer twelve in figure 4.4, show the expected behavior [44].

To compare the diodes the leakage current at 100 V are normalized to the area.

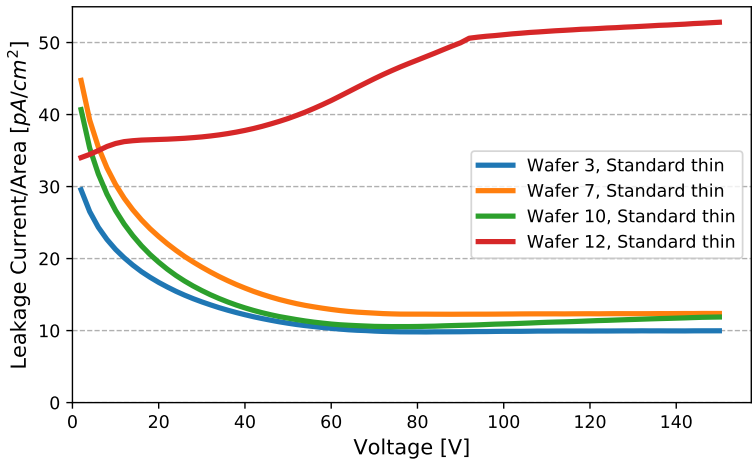

Figure 4.4.: Illustration of the I-V curves of some Standard thin diode on different wafers. Most diodes show a reverse of the expected behavior. Through the Shockley current an increase of leakage current is expected and not a decrease. The dominant effect of the current for low voltages are charge carriers that are produced somewhere in the wafer and diffuse into the diode. To prevent this, guard rings are put around the diodes. The rings and the diodes are on the same potential. By applying a voltage to a ring an electric field is established that prevents external charge carriers to enter. With increasing voltages the field has a wider range and fewer external charge carriers enter the diode. Therefore, the measured current decreases. At a certain voltage no external charges are able to enter the diode and only the internal leakage current is measurable. The disturbing external charges are mainly produced by random static charges of the silicon oxide layer. Therefore, some diodes might show the expected behavior.

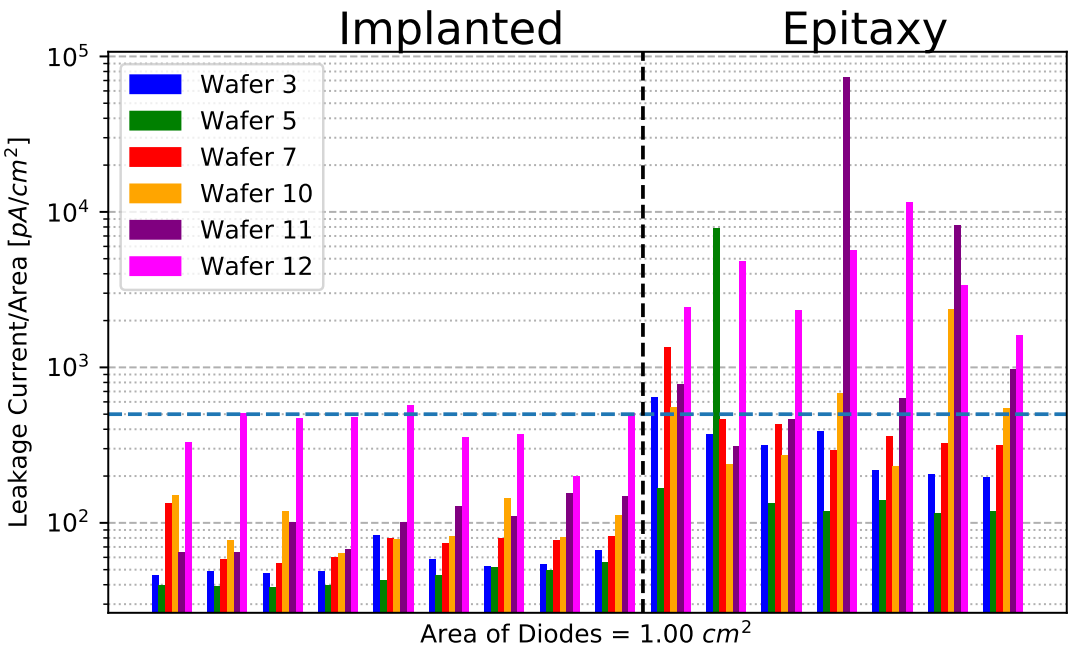

Figure 4.5.: Leakage current of some diodes at 100 V. On the left are implanted diodes and on the right Epitaxy ones. The current in Epitaxy diodes is generally higher compared to implanted diodes. The line at 500 pA cm^{-2} is the limit for the failure rate calculation.

Examples of this comparison are shown in figure 4.5. The epitaxy diodes show, in general, higher leakage currents than the implanted ones. Especially the wafer which was processed differently has higher currents. This is expected because the oxidation step during production was different for this wafer and this technique is known to produce higher leakage currents.

It is not completely understood why Epitaxy diodes have higher leakage currents. One possibility is small impurities like dust on the wafer to which MBE diodes are more sensitive than implanted ones. For use in TRISTAN a higher leakage current is not problematic as the detector system will eventually be cooled to −50 °C, which decreases leakage.

At a certain level of leakage even cooling cannot decrease the current far enough. The detectors are then unusable. One way of determining if a diode is unusable or not is by setting a limit on the leakage current per area. All diodes above this limit are considered broken. Here, this limit is set to 500 pA cm^{-2} at 100 V reverse-bias voltage. The rate of failed diodes is determined for Epitaxy and implanted diodes and are shown in table 4.1. The epitaxy diodes have for every diode area a higher

rate of failures. The increase with area supports the claim that these high leakage currents stem from impurities on the wafer during the growth process.

Table 4.1.: Failure rates of diodes. The failure rate is calculated by assuming that all diodes with leakage currents above $500\,\mathrm{pA\,cm^{-2}}$ at 100 V are broken. The number of diodes of one type and area is given in brackets.

Area [cm^2]	Epitaxy Diodes	Implanted Diodes
0.1	12.5 % (160)	1.6 % (320)
1.0	46.7 % (60)	1.0 % (100)
5.0	60 % (10)	0 % (15)

4.4. Electron Efficiency Determination

After the wafers were cut the diodes can be used as pin-diodes (see section 2.1.2). Incoming particles create electron-hole-pairs in the depleted region which are then accelerated to the anode and cathode. This creates an electric pulse. The height of this pulse depends on the deposited energy inside the diode. The entrance window of a diode alters the energy of incoming particles before they deposit energy inside the depleted region. Therefore, not all incoming energy can be deposited inside the depleted region. The efficiency ϵ describes how much energy is lost due to the entrance window. Different entrance windows lead to different efficiencies. This energy loss is especially relevant for charged particles, because of their constant interaction with matter they lose a significant amount of energy inside the entrance window. This can be used to characterize the diodes. By exposing the diode to a beam of monoenergetic particles the pulse of electron-hole-pairs becomes a continuous current I_{Diode}. This current is proportional to the flux and energy of the beam. Measuring this current and comparing it to the theoretically possible, the efficiency can be described by:

$$\epsilon = \frac{I_{\mathrm{Diode}} - I_{\mathrm{Leak}}}{I_{\mathrm{SEM}}} \cdot \left(\frac{E_{\mathrm{SEM}}}{\omega} \right)^{-1} \tag{4.1}$$

I_{Leak} is the leakage current. I_{SEM} and E_{SEM} are the current of the beam and energy per particle. ω is the energy needed to create one electron-hole-pair in silicon at room temperature and is equal to 3.64 eV [37].

The first part of this section describes the setup and results of the efficiency measurements. The second part depicts the efficiency simulations performed using KESS. This is used to determine a dead layer for the different diodes.

4.4.1. Description of Measurement

Working Principle of a scanning electron microscope

As beam particles electrons were chosen. The monoenergetic electron source used for the efficiency determination of the diodes is a scanning electron microscope (SEM) located at the MPG HLL. It is a JSM-IT300 from JEOL [23], shown in figure 4.6.

The electron microscope consists of three main elements: the electron beamline, the vacuum chamber, and the Everhart-Thornley detector.

Electron beamline: The working principle of the beamline is shown in figure 4.7. The electron source of the SEM is a tungsten filament heated up to 2000 °C. It is located inside a funnel-shaped cylinder to which an negative potential is applied. This is called Wehnelt cylinder. This way the electron emission is suppressed on the side on the filament and only the tip of the filament emits electrons. The negative voltage of the Wehnelt cylinder shapes the electrons into a beam. The acceleration voltage is applied between the anode and the filament. The energies are adjustable between 0.3 keV to 30 keV. The accuracy of the beam energy is about 2% whereas the resolution is smaller than 1 eV [47]. After the acceleration, the beam is focused through magnetic coils to an aperture. The electron's direction of movement is perpendicular to the magnetic fields. Therefore, the Lorentz force created by the fields only change the direction of the electron but not the energy. Directly behind the aperture sits a removable Faraday cup. This is used to measure the current of the electron beam. Shortly before entering the vacuum chamber the beam is deflected periodically by magnets. In this manner the beam scans over a specific area of the sample. An important feature of the microscope is its control over the electron beam current. Electrons hitting the target can charge the surface if its conductivity is low. These are so-called charging artifacts. They influence especially electrons with only a few hundred eV of energy as already small electric potentials can deflect or decelerate such electrons. At higher energies, electrons are hardly influenced by small electric fields. An artifact is shown in figure 4.8. It is only visible in the electron microscope because it also affects the secondary electrons created by the beam. To minimize the appearance of this effect a current below 100 pA was used in the measurements.

Vacuum chamber: The pressure in the vacuum chamber is 0.1 mbar [23]. The diodes are mounted on a five-axis movable table inside the chamber, as well as an infrared camera, and an Everhart-Thornley detector for taking pictures are located.

The infrared camera is only used to check the positioning of the samples in the beginning and then turned off. The light from the camera would induce a much

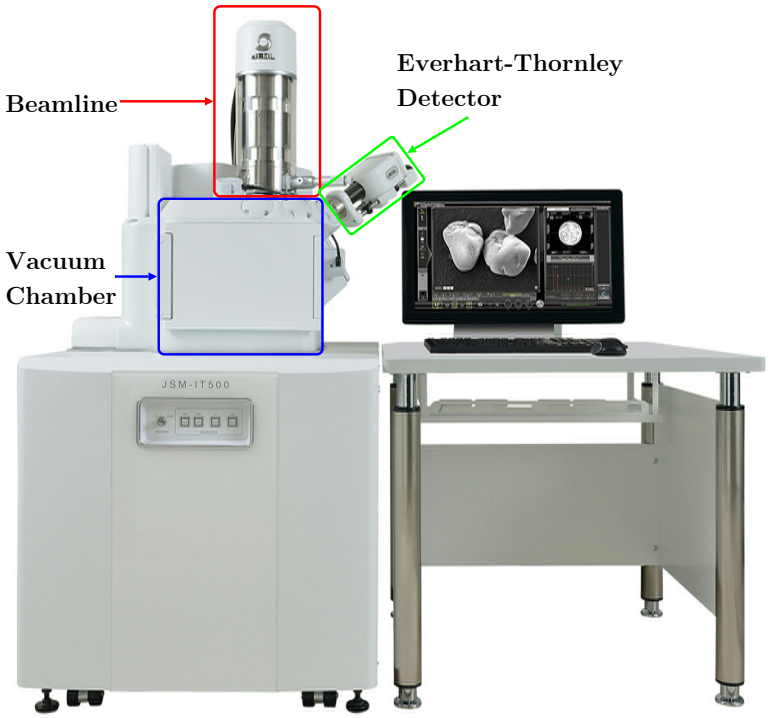

Figure 4.6.: Depiction of the scanning electron microscope used in this thesis. It consists mainly of three components: the beamline, the vacuum chamber and the Everhart-Thornley detector. In the beamline the electrons are created, accelerated and focused onto the sample. The sample sits inside the vacuum chamber on a movable table. By shooting high energy electrons onto the sample low energy secondary electrons are created. With these the Everhart-Thornley detector creates the pictures of the sample. Taken from [23].

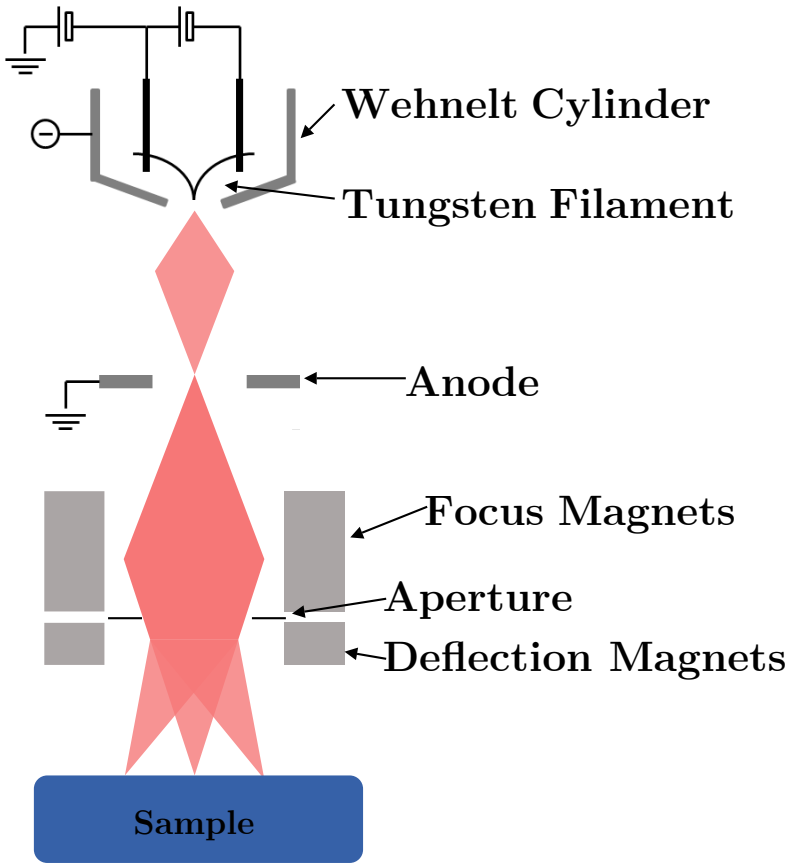

Figure 4.7.: Working principle of a SEM beamline. The tungsten filament is heated and emits electrons at its tip. These are accelerated through the negative potential applied to the Wehnelt cylinder towards the anode. Afterwards, the electron beam is focused by magnetic fields. Passing an aperture magnets deflect the beam periodically to scan over an area on the sample.

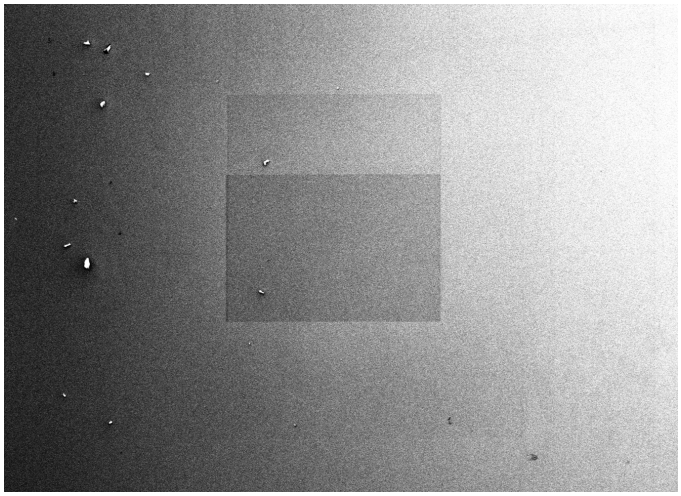

Figure 4.8.: SEM picture of a diode with charge artifacts. This happens when an sample inside a electron microscope is not perfectly electrically conductive. Electrons stick to this part of the sample and create a potential that affects the energy of incoming particles in this region. High energy electrons are hardly affected by this. The small crumbs are the rest of a protective layer on the wafer.

higher leakage current in the diodes if operated during measurement.

Everhart-Thornley Detector: This detector (figure 4.9) is used for the creation of pictures. It consists of a Faraday cage, a scintillator, a light guide and a photomultiplier. When the electron beam hits the sample, secondary electrons are created with several tens of electron volts of energy that escape the sample. These new electrons are then caught by the Faraday cage which is on a potential of 300 V. Inside the cage the electrons are accelerated towards the scintillator as its potential is 12 kV. There, the electrons convert their energy into photons which are guided through the light tube to a photomultiplier. Since the detector catches nearly all secondary electrons, the output of the photomultiplier is proportional to the production rate of secondary electrons of the spot at which the electron beam hits the target. Additionally, to attract all secondary electrons the detector's Faraday cage also shields the inside of the vacuum chamber from the scintillator's electric field. The electron beam could otherwise be deflected or distorted.

Setup

Measuring the efficiency of the diodes is done after the diodes have been cut, glued to an electrically conductive plate on a PCB, and bonded to the voltage supplies.

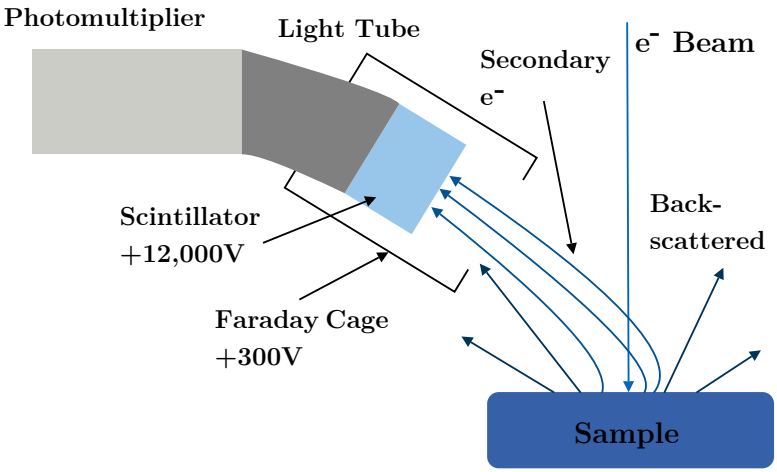

Figure 4.9.: Sketch of an Everhart-Thornley detector used in a SEM. The high energy electron beam creates low energy secondary and higher energy backscattered electrons. The 300 V potential of the Faraday cage attracts nearly all secondary electrons as their low energies allow for large deflection angles. Inside the cage sits a scintillator at a potential of 12 kV. The incoming electrons get accelerated towards the scintillator and create light inside of it. This light is then guided through a light tube to a photomultiplier for light detection.The amount of light is proportional to the number of secondary electrons created on the sample as backscattered primary electrons are negligible.

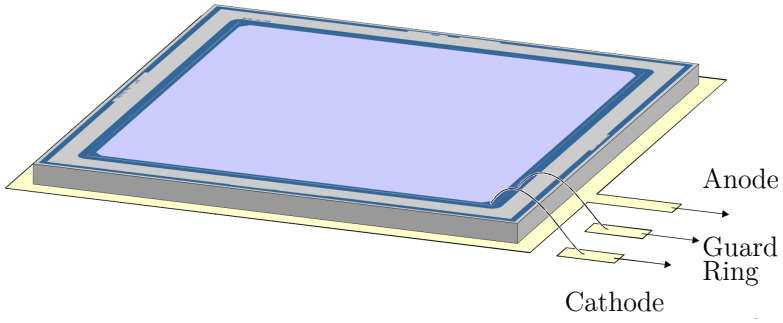

Figure 4.10.: Schematic drawing of the bonding scheme of the diodes for the efficiency measurement. The diode has a guard ring to prevent electrons entering or leaving from the sides. The entrance window is a p^+ cathode and the anode is n^+ doped. Both the entrance window and the guard ring are on ground potential. To the back of the detector 10 V are applied. Taken from [30].

The bonding scheme is shown in figure 4.10. Following this scheme the PCBs of figure 4.11 were designed. Figure 4.11a shows the PCB on which two diodes can be glued and bonded. The gold finished open connections are for gluing and the bonding of the diodes. These open connections are connected through tracks to a 3-pin male connector. With these connectors the diodes are mountable to the 3-pin female connectors of the PCB in figure 4.11b. The white space here indicates the positioning of the first PCBs. A 20-pin female connector allows connections through a ribbon cable to the power supply and the ammeters for readout. The second PCB is mountable on the table in the SEM. This setup allows for an easy preparation of the diodes and to test four diodes simultaneously which means fewer flushings of the vacuum chamber. Figure 4.12a shows the diodes glued to the PCBs. The prepared diodes are then mounted on the table of the electron microscope directly below the electron beam. The position of the mount is adjustable through the movable table. The ammeter that is used for the measurement of the diode current also provides the applied voltages, through the feedthroughs. Two similar ammeters were used, one for the leakage and diode currents, and one for the electron beam current. The p^+ entrance window and the guard ring are both on ground potential while 10 V are applied to the back. The complete setup is shown in figure 4.12.

4.4.2. Efficiency Measurement Results

Before the cutting of the wafers the diodes' leakage current was characterized. Some representative diodes of each kind were chosen to examine the measurement

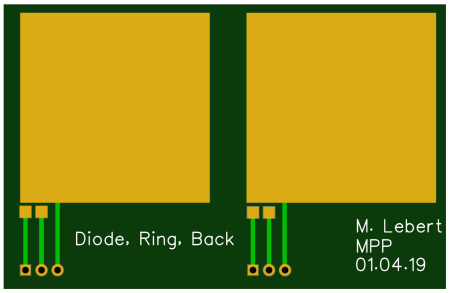

(a) PCB for mounting the the diodes.

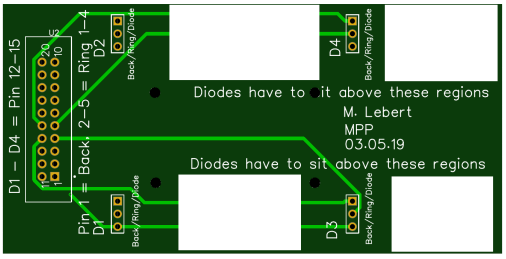

(b) PCB for mounting the diodes in the SEM.

Figure 4.11.: PCB design for mounting the diodes in the efficiency measurements. a) shows the PCB on which the diodes are glued and then bonded to the power supply and ground. b) shows the PCB on which the first PCBs are stacked. It is connected through a ribbon cable to the power supply and the ammeters. This PCB is mountable on the table in the SEM. The light green tracks are the copper lines, the golden regions are open gold finished connections.

(a)

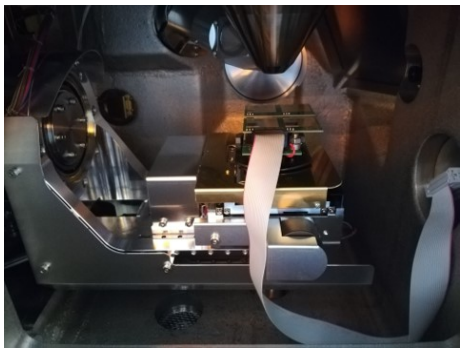

(b)

Figure 4.12.: Setup of the efficiency measurements. (a) shows the diodes glued to the PCB. In (b) the PCBs are mounted inside the electron microscope directly below the electron beam.

efficiency for electrons. From the wafers five, seven, ten, and twelve one Standard thin and thick, one Epitaxy, and one Epitaxy-COV were tested. It is expected that the efficiency of Epitaxy diodes is much higher than the implanted ones in the energy range of a few keV. Low energy electrons have a small mean free path inside silicon. Therefore, they lose a significant amount of energy shortly after entering the material. Higher energy electrons have a high mean free path, so that they pass the entrance window nearly undisturbed. So the energy range of 0.3 to 2 keV was probed more extensively than the higher energies. Due to charge artifacts, the correct measurement of low energy electrons is more difficult than for high energies. To minimize the effect of those build-up charges, the position of the diodes was slightly changed during measurements to hit the diode on charge free regions.

The results of these measurements are shown in figure 4.13. The four plots show a different wafer each. The uncertainties of the measured efficiencies are calculated as described in appendix B.3. The sharp edge below 1 keV that occurs in all measurements stems most probably from the electron microscope. It is likely that at such low energies the microscope is not working properly for this kind of measurement anymore. One reason for that might be the potential of the Everhart-Thornley detector. At these energies the potential of 300 V could be enough to deflect the beam which would reduce the electron flux on the diode. As this edge was only observed after the measurements were taken, the detector was not turned off. Another possibility is, because of the lower mean free path the electrons scatter on the residual gas inside the vacuum chamber. The chamber should be at a pressure of 0.1 mbar [23] but this cannot be checked, because there is no pressure gauge. For these reasons, energies below 1 keV are not considered in the comparison of the diodes.

The maximum efficiency of about 90 % is due to backscattering. Some electrons enter the diode and deposit some of their energy inside the material before leaving it through random scattering with some residual energy.

The two Epitaxy pin-diodes behave nearly identical across all wafers and also compared to each other. The non-epitaxy diodes are not as consistent but are always much less efficient than the epitaxy diodes in the low energy region. This already shows that the entrance windows grown with MBE are an improvement for detecting low energy electrons. This corresponds to a much thinner entrance window.

4.5. Efficiency Simulation

With MBE several monolayers of doped silicon are grown onto the substrate. Hardly any diffusion into the substrate is expected. Therefore, a dead layer model as

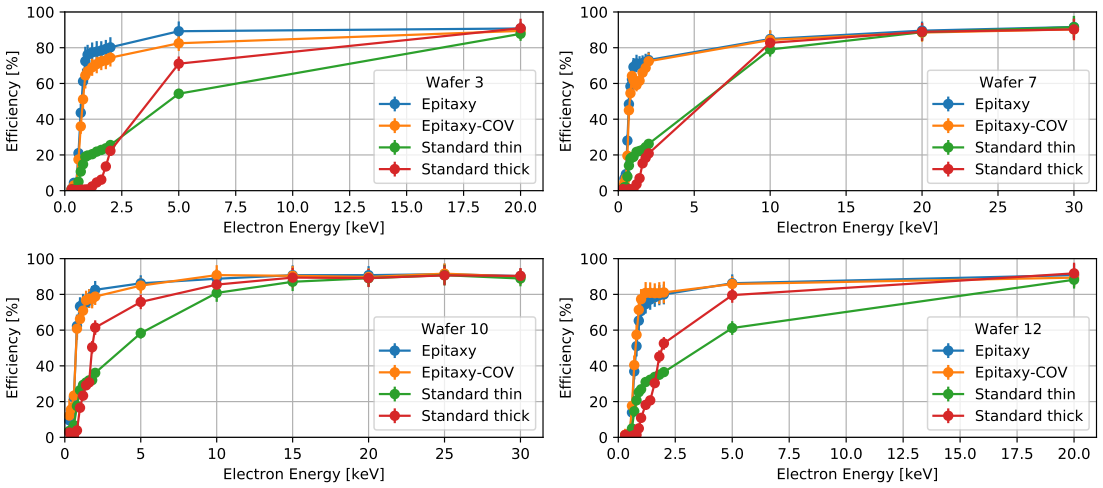

Figure 4.13.: Results for the efficiency measurements of the same type of diodes on different wafers. It is clearly visible that the efficiency for the Epitaxy technique is much higher in the low energy range. No significant difference between the two different Epitaxy diodes occurred.

described in section 2.1.3 is well suited to describe these diodes. For Epitaxy diodes even a sharp edge dead layer should be sufficient. For the standard diodes at low energies no correct description with this model is expected because the implanted dose is spread by diffusion during annealing. Also in the area of low implantation dose at the end of the implanted range, live time and diffusion length of signal charges are high. Therefore, a dead layer with a "washed-out" step function is used. KESS simulations are performed to extract the position and shape of the dead layer from an efficiency curve. In these simulations, 10^6 monoenergetic electrons hit a silicon target. This was simulated at different energies. As KESS is designed for pure silicon the SiO_2 layer could not be taken into account in the simulation but only during analysis. The silicon is divided into an active and an inactive part. The energy inside the active part $E_{\text{dep.active}}$ is the deposited energy weighted with a charge collection efficiency and summed up. Dividing this by the total energy E_{total} that is in the beam gives the efficiency of the simulated detector at a certain incoming energy:

$$\epsilon = \frac{\sum E_{\text{dep.active}}}{E_{\text{total}}} \tag{4.2}$$

The CCE is described by:

$$\text{CCE}_{\text{DL}}(z) = \begin{cases} 0 & \text{for:} \quad z < s \\ \frac{1}{2}\left(1 + \text{erf}\left(\frac{z-\mu}{\sqrt{2\sigma^2}}\right)\right) & \text{for:} \quad s \leq z \leq D \end{cases} \tag{4.3}$$

Table 4.2.: The results of the fit of the simulated CCE to the measured efficiency for wafer ten.

Diode	Dead Layer position μ [nm]	Spread of Step Function σ [nm]
Epitaxy	3.4 ± 0.6	0.0 ± 1.5
Epitaxy-COV	4.60 ± 0.01	0.00 ± 0.02
Standard thin	53 ± 9	105 ± 30
Standard thick	21.0 ± 0.4	0.0 ± 0.1

z is the position inside the silicon, measured from the side facing the electrons. D is the depth of the silicon and s the thickness of the silicon oxide layer. Because SiO_2 is an insulator all deposited energy in it is lost. Inside the silicon, the collection efficiency is described by a cumulative Gaussian function. This results in a "washed-out" step function. μ describes the position of the step function. With the spread σ of the cumulative function an influence of the different doping mechanisms and concentrations is taken into account. If σ approaches zero the cumulative Gaussian becomes a sharp edge step function. This is assumed for the diodes with epitaxial layers. Here, all doped boron atoms are in the thin epitaxial layer and thus no influence beyond a sharp edge layer is expected. For the implanted diodes the doping profile extends over a bigger volume (see section 2.1.2). Therefore, the electrical field and depletion is not as well defined close to the interface as for the Epitaxy diodes. Hence, an influence deeper into the detector is expected.

The simulated CCE with μ and σ as free parameters was fitted to the measured efficiency of the diodes in the energy range of 1 to 2 keV. This range was chosen because lower energy electrons lose a significant fraction of their energy in the dead layer. For higher energy electrons the dead layer is nearly negligible.

The result of this procedure is shown for one wafer. This is only an example and the results are applicable to all wafers. The simulation with the measured data is shown in figure 4.14. The diodes with their fitted simulated efficiency and corresponding charge collection efficiency are depicted in figure 4.15. The resulting dead layer position and width for the CCE are also given in table 4.2. The results for the other wafers is shown in appendix D.

The efficiencies of all diodes are reproduced by the simulation and show the expected result. Epitaxy diodes are described by a sharp edge charge collection efficiency which corresponds to a sharp edge dead layer. With (3.9 ± 0.6) nm and (4.60 ± 0.01) nm the dead layers are in the same order of magnitude as the natural grown silicon oxide. Therefore, these diodes have, already at low depths, an electrical

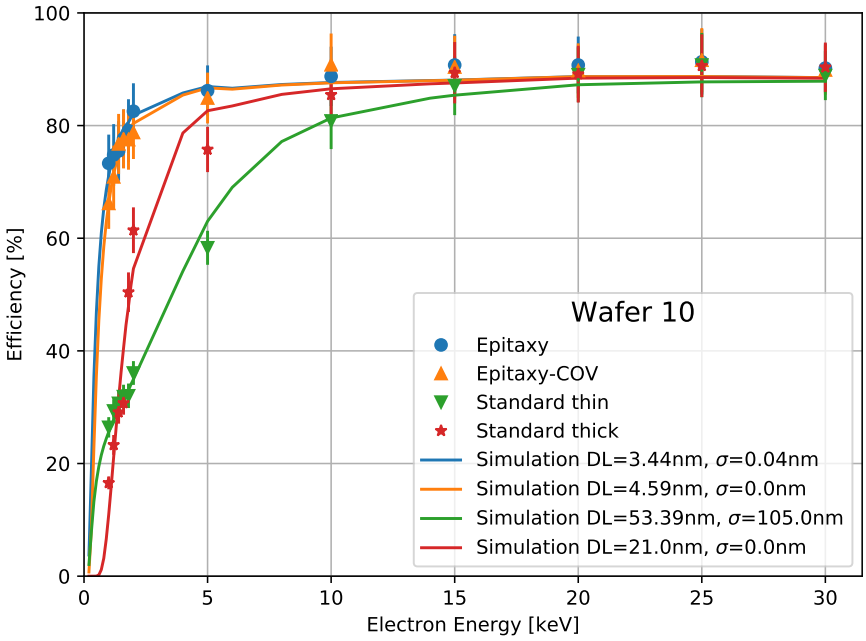

Figure 4.14.: Fit of the simulated to measured efficiencies. The efficiencies of the diodes are reproducible.

field high enough to collect nearly all created charges. The CCE of the Standard thin diode, on the other hand, is below 75 % in the first 100 nm of the diode. This corresponds to a lower doping concentrations at these depths and therefore a greater loss of charges. The pn-junction of this kind of diode is at about 200 nm. Even though, the junction is far away, the live time of the created electrons is long enough to diffuse to the anode. So the increase of efficiency is corresponding to the reduced distance to the junction. The CCE of the standard thick diode is also a sharp edge dead layer, but deeper inside the diode. This shows that the junction is closer to the surface of the diode and therefore a higher efficiency is achieved close to the silicon, silicon oxide interface.

4.6. Summary of Epitaxy Diodes

A comparison of diodes created by ion beam implantation and molecular beam epitaxy was performed in cooperation with the Halbleiterlabor of the Max-Planck-Society. Twelve wafers with implanted and epitaxial doped diodes were produced. The diodes have areas of 0.1, 1 and 5 cm^2. To compare the two technologies the leakage current of all diodes and the efficiency of some was measured.

The leakage current measurements were performed before cutting the wafer at

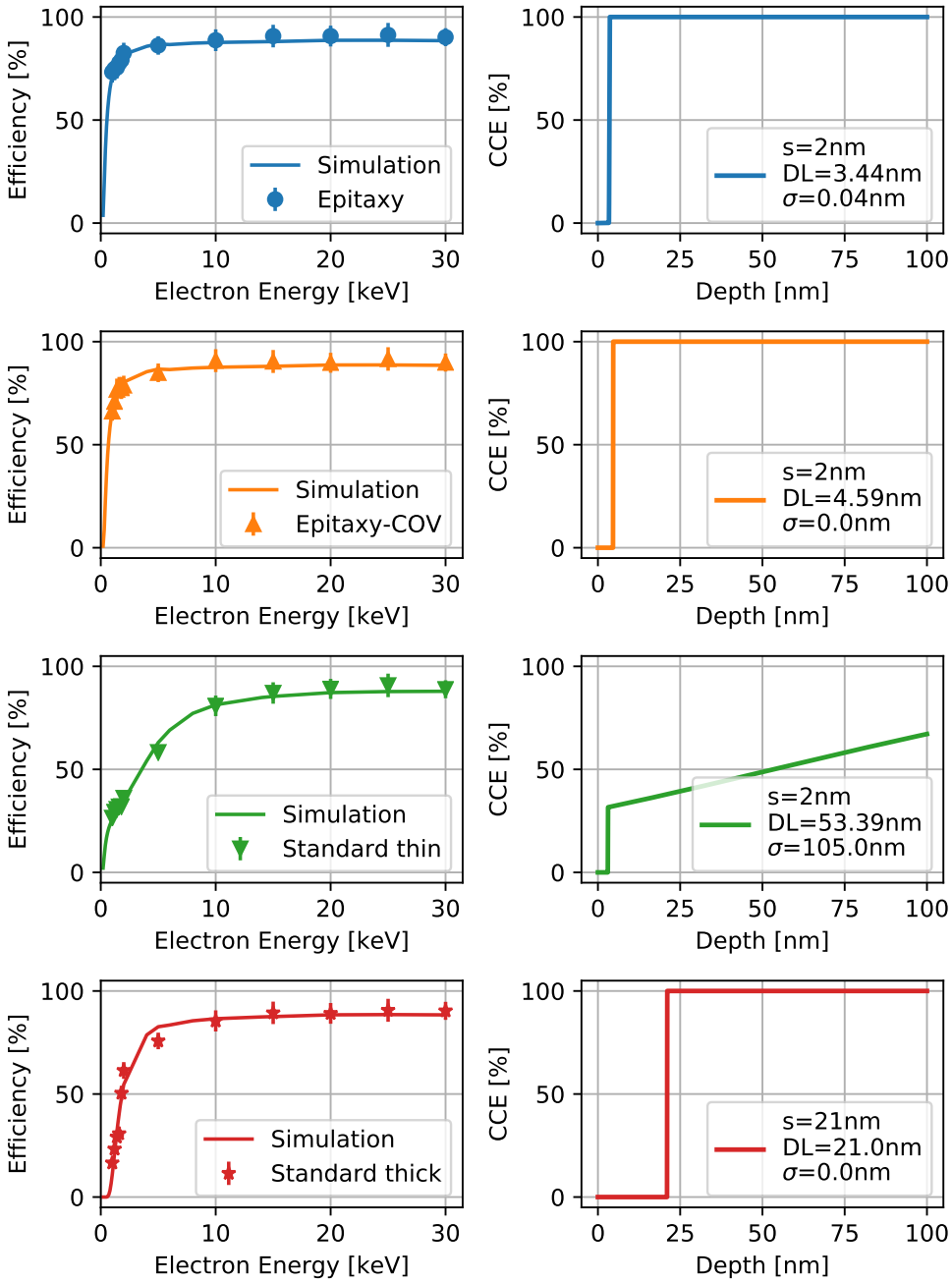

Figure 4.15.: Fit of the simulated to measured efficiencies and corresponding CCE. On the left are the measured and the simulated efficiencies for diodes on wafer ten. On the right, the charge collection efficiency corresponding to the simulation on the left are plotted. The Epitaxy diodes are described by a step function that are only a few nm into the silicon. The Standard thin has a long tail that reduces the efficiency. Standard thick diodes are also described by a sharp edge dead layer, but much deeper inside the diode.

room temperature. It shows that ion implanted diodes have in general a lower leakage current than those with an epitaxial layer. This is not problematic as cooling the diodes reduces the leakage current. Unfortunately, at a certain point the leakage current is too high and even cooling cannot reduce it far enough. This means that those diodes are unusable for application such as TRISTAN. Thus, a failure rate of the diodes is derived from the leakage currents. Implanted diodes show only low failures up to 1.6 % for an area of 0.1 cm^2. Epitaxy diodes have much higher failure rates, 12.5 % of the smallest ones are broken, bigger ones have even higher rates. This, most likely, stems from particles like dust on the wafer before doping. Ion implanting is much less sensitive to such small impurities than epitaxial growth.

As a major result of this thesis, the efficiency of some diodes was measured using a scanning electron microscope. The efficiency is determined by measuring the resulting current of a diode when an electron beam hits it. This is compared to the theoretical current the beam could produce in silicon. It shows that at energies above 10 keV hardly any difference is found between the measured Epitaxy and implanted diodes. But at low energies a clear difference is visible. Already at 1 keV the efficiency for Epitaxy diodes is at roughly 70 % while implanted ones are around 15 to 25 %. The efficiency was reproduced with KESS simulations to determine the dead layer of the diodes. This showed that the diodes with an epitaxial layer are best described with a sharp edge dead layer off only a few nm inside the diode. Also, the Standard thick diodes are best described by a sharp edge dead layer, but deeper inside the diode, directly behind their SiO_2 layer. On the other hand, Standard thin diodes have a very broad "washed-out" step function as charge collection efficiency that stretches beyond 100 nm until it reaches 100 %. This shows that the implanting through the SiO_2 layer is much shallower than the implanting without this layer. Therefore, the pn-junction is closer to the surface and the charge collection efficiency is better shortly after the silicon oxide layer.

These results show that molecular beam epitaxy is a viable production technology for pin-diodes and future SDDs. Especially in the low energy region the performance is superior to ion implanted diodes. But in order to use them in a complicated and expensive process like TRISTAN SDD production, the failure rates need to be reduced drastically.

5. Conclusion and Outlook

In this thesis the entrance windows of silicon drift detectors are investigated. In the first part of this work, conversion electrons from the ^{83m}Kr decay are used to characterize the entrance window thicknesses of the TRISTAN prototype detectors. In the second part, an assessment of molecular beam epitaxy as a possible doping process for future TRISTAN detector entrance windows was performed.

Charged particles have a high interaction rate while traversing matter and therefore lose energy. Consequently, the entrance window of a detector changes the energy of incoming particles before they can be measured. This makes it an important property of the detector which needs to be known precisely. Several silicon drift detectors with different entrance windows were fabricated. For two of those, S0-1 and R0-2, this entrance window was characterized. The model for the entrance window is a sharp edge dead layer. Through a tilting angle between detector and source the effective thickness of the dead layer increases for incoming particles. Thus, the measured peaks for the same incoming energy are shifted to lower energies at higher tilting angles. The relative shift between two angles is independent of any external influences and only depends on the dead layer of the detector. Two measurements were performed per detector, one untilted and one at 60° tilting. The charged particles chosen for this characterization are quasimonoenergetic conversion electrons from ^{83m}Kr decay. The source of this metastable state is ^{83}Rb evaporated onto Highly Oriented Pyrolithic Graphite. This kind of source is not expected to alter the electron energies significantly. The resulting shifts are in the range of 85 to 130 eV for detector S0-1 and 30 to 45 eV for R0-2. The shifts of the K-32 line at 17.8 keV are compatible with previous measurements performed with the same measurement technique at 14 keV using a scanning electron microscope as electron source.

Relating the measured energy shifts to dead layer thicknesses was achieved by Monte-Carlo simulations using Geant4. For these, a source of decaying ^{83}Rb was simulated in front of silicon. In one simulation the source was parallel to the silicon and in the other it was tilted at 60°. Different dead layer thicknesses were implemented during the analysis of the peak positions. With the resulting linear relations between energy shift and dead layer the thicknesses of the detectors' entrance windows were determined. As a result a dead layer of (210 ± 2) nm for S0-1

is found and (70 ± 2) nm for R0-2 at an electron energy of 17.8 keV. Comparing these results to previous measurements similar energy shifts are found. However, it is shown that the interpretation as dead layer depends on the Monte-Carlo simulation code. Significant differences in the dead layer thickness are found when using KESS instead of GEANT4. This discrepancy is currently under investigation.

Finally, the absolute measured peak position to the theoretical prediction are compared. Taking into account the dead layer measured with the above-mentioned tilt method and the electric potentials at the detector, the remaining energy shift can potentially be related to energy losses in the source. The comparison shows a remaining shift of the order of 30 eV for source HOPG. A small unexpected dependence of the remaining shift on the detector is still under investigation.

In the second part of this thesis, molecular beam epitaxy as a possible production technique for future TRISTAN detectors is investigated. A standard technology for creating doped layers on silicon is ion implantation. The silicon substrate is exposed to a high energy beam of dopant atoms. After implantation the substrate has to be annealed to incorporate the additional atoms into the lattice. This creates a doping profile that can stretch several µm into the silicon. Contrary to this, epitaxy describes crystal growth techniques, in which thin films of several nm are grown onto a crystalline substrate. Molecular beam epitaxy is a possible implementation of this technique. It can be described as a form of vacuum evaporation with high material purity and high control over doping concentrations. This reduces the thickness of the dead layer on the diodes drastically compared to ion implantation.

To test the viability of this technique, twelve wafers with epitaxy and ion implanted pin-diode of different areas were produced. The first investigated property is the leakage current of the diodes. This was measured before the wafers were cut. Generally the leakage current of epitaxy diodes at a bias voltage of 100 V was higher than for the implanted ones. The leakage current is temperature dependent and thus, is reduced by cooling. So an increased leakage current is mostly not a problem for TRISTAN as the detector system will be eventually cooled to $-50\,^{\circ}\mathrm{C}$. But at a certain level the cooling is not enough to make a diode usable for TRISTAN. Therefore, a failure rate of the diodes can be calculated by assuming that all diodes above a set limit are broken. This limit is set to $500\,\mathrm{pA\,cm^{-2}}$. The failure rate of ion implanted diodes is below 2 % for all areas. Epitaxy diodes have much higher rates, starting at 13 % for the smallest areas and even higher ones for bigger areas. The higher leakage current and the subsequent higher failure rate stems most likely from impurities on the wafer during doping. Because of the crystalline growth molecular beam epitaxy is much more sensitive to specs of dust or similar pollutants on the wafer than ion implantation is. This is currently investigated by applying molecular beam epitaxy to an unstructured wafer. There the whole area can be

investigated. Also, a reduction of the leakage current can be expected by optimizing the individual wafer processing steps for epitaxy.

The second property investigated was the efficiency of the diodes. Taking the leakage current results, four representative diodes from four wafers were chosen, two epitaxy and two implanted diodes. These were glued and bonded onto newly designed printed circuit boards. Those diodes, operated in reverse-bias configuration, were exposed to beams of monoenergetic electrons from a scanning electron microscope. In this setup the electrons create electron-hole-pairs inside the depleted region of the diodes. This results in a measurable current. The current is then compared to the current that would be theoretically possible if all energy would be deposited inside the active region and all created electrons were measured. This is defined as the efficiency of a diode. It shows that at energies above 10 keV hardly any difference between the pin-diode is visible. Between 1 and 2 keV the epitaxy diodes have a nearly 40 % higher efficiency than the implanted ones. This is a result of the much thinner entrance window.

To link this efficiency to a dead layer KESS simulations were performed. The dead layer model here is described by a "washed-out" step function after the silicon oxide of the diode. This model is then fitted to the measured efficiencies. The results of this procedure show that the epitaxy diodes can be described by a sharp edge dead layer that has a thickness of $\backsimeq 5$ nm. Ion implanted diodes, on the other hand, are described by much thicker dead layers.

These results show that epitaxy can create working pin-diodes with entrance window thicknesses of a few nm. This indicates that molecular beam epitaxy might be a viable option for the production of future TRISTAN silicon drift detectors. This would then reduce the effect of the entrance window and could improve the sensitivity to sterile neutrinos of TRISTAN. Reducing the failure rate is the first step in further development. An important challenge will be the production of first silicon drift detectors, because no silicon drift detector has been produced using molecular beam epitaxy as doping procedure for the entrance window, that resulted in such small dead layers. At the moment a new set of wafers has been produced and is now being tested.

A. Stability of Line Positions

Here it is tested whether measurements with the detector yield better results if the detector is maintained at a constant temperature. Without constant cooling temperature fluctuations through room temperature changes or direct exposure to sunlight may occur. This might lead to different measured energies at the same incoming energies. The CUBE amplifiers and also the leakage current of the SDDs are temperature dependent, therefore temperature fluctuations would change the output of the detector. These constantly changing energies that are then measured would lead to a broadening of a peak. To test this, two measurements were performed, one without temperature stabilization and one where the detector was maintained at 15 °C. The setup is explained in sections 2.3 and 3.2.2. Each measurement was segmented into slices of 20 min, then the peak position was determined as described in section 3.3. The peak width was determined by calculating the FWHM of the fitted function and then dividing by $2\sqrt{2\ln 2}$. The spread of the peak positions and the peak widths within one measurement are given in tables A.1 and A.2.

For photons the temperature stabilization makes hardly a difference. The electron peaks, on the other, hand have a slightly smaller spread in both peak position and peak width. It is unlikely that the smaller spreads come from a better performance of the detector as room temperature is regulated to be in the range of 20 to 23 °C and the photon peaks are not affected. Therefore, the detectors were maintained at 15 °C in all measurements.

Table A.1.: Spread of the peak positions with and without temperature stabilization.

Peak	No Stabilization [eV]	15 °C [eV]
γ-9.4	1.8	1.6
K_α	1.4	1.5
K_β	1.8	1.8
K-32	7.5	5.6
L-32	3.5	5.0
M-32	6.7	7.6

Table A.2.: Spread of the peak widths with and without temperature stabilization.

Peak	No Stabilization [eV]	at 15 °C [eV]
γ-9.4	1.5	1.3
K_α	0.4	0.4
K_β	1.2	1.2
K-32	9.3	8.8
L-32	5.4	3.0
M-32	5.5	7.4

B. Uncertainty Calculation

B.1. Bootstrap Method

The uncertainty of a value can be calculated using the Bootstrap method:
The function f depends on n parameters. The parameters have an uncertainty on themselves and can be correlated with each other. The covariance matrix $Cov(n)$ of the parameters n gives the squared uncertainties on the diagonal axis and a correlation factor (the covariances) of the parameters on the off-diagonal positions:

$$\text{Covariance Matrix Example for:} \quad n = a, b, c$$

$$Cov(a, b, c) = \begin{pmatrix} \sigma_a^2 & \sigma_{ab} & \sigma_{ac} \\ \sigma_{ba} & \sigma_b^2 & \sigma_{bc} \\ \sigma_{ca} & \sigma_{cb} & \sigma_c^2 \end{pmatrix}$$

To determine the uncertainty of f at a certain point $\bar{n}$, several thousand parameter pairs are drawn from a distribution following covariance matrix $Cov(\bar{n})$ around $\bar{n}$. Then f is evaluated at all drawn parameter points and the resulting function value is assumed to be Gaussian distributed. The width σ of the Gaussian is the 1σ uncertainty on $f(\bar{n})$.

B.2. Dead Layer Shift Uncertainty

The dead layer shift is calculated with equation equation (3.7). Equation (B.2) shows that this can be rewritten in a form that is independent of the offset of the calibration. Following that equation (B.3) describes the uncertainty of Δ_{DL} using Gaussian uncertainty propagation. Similar to that equation (B.4) describes the error of the relative peak position in ADCchannels. By assuming that the error on the calibration is much smaller than the uncertainty of the relative position it can be concluded that the error of Δ_{DL} is the quadratic addition of the peak position

uncertainty.

$$\begin{aligned}\Delta_{DL} &= E^{keV}_{\Theta_0} - E^{keV}_{\Theta_1} && \text{(B.1)}\\ &= \left(m \cdot E^{ADC}_{\Theta_0} + t\right) - \left(m \cdot E^{ADC}_{\Theta_1} + t\right)\\ &= m \cdot \left(E^{ADC}_{\Theta_0} - E^{ADC}_{\Theta_1}\right)\\ &= m \cdot \Delta E^{ADC} && \text{(B.2)}\end{aligned}$$

$$\Rightarrow \quad \sigma_{\Delta_{DL}} = \sqrt{(\sigma_m \cdot \Delta E^{ADC})^2 + (m \cdot \sigma_{\Delta E^{ADC}})^2} \qquad \text{(B.3)}$$

$$\text{with:} \quad \sigma^2_{\Delta E^{ADC}} = \sigma^2_{E^{ADC}_{\Theta_0}} + \sigma^2_{E^{ADC}_{\Theta_1}} \qquad \text{(B.4)}$$

$$\text{and:} \quad \sigma_m \cdot \Delta E^{ADC} << m \cdot \sigma_{\Delta E^{ADC}} \qquad \text{(B.5)}$$

$$\rightarrow \quad \sigma_{\Delta_{DL}} = \sqrt{\left(m \cdot \sigma_{E^{ADC}_{\Theta_0}}\right)^2 + \left(m \cdot \sigma_{E^{ADC}_{\Theta_1}}\right)^2} = \sqrt{\sigma^2_{E^{keV}_{\Theta_0}} + \sigma^2_{E^{keV}_{\Theta_1}}} \qquad \text{(B.6)}$$

B.3. Diode Efficiency Uncertainty

The uncertainty on the measured diode efficiency was calculated with linear error propagation for the statistical uncertainty and Taylor-expansion to the linear term for the systematic uncertainty. The equation for the efficiency is given by:

$$\epsilon = \frac{I_{\text{Diode}} - I_{\text{Leak}}}{I_{\text{SEM}}} \cdot \left(\frac{E_{\text{SEM}}}{\omega}\right)^{-1}$$

The systematic error is calculated by:

$$sys = \sum_i \frac{\partial \epsilon}{\partial x_i} \Delta x_i \quad \text{for} \quad x_i = I_{\text{Diode}}, I_{\text{Leak}}, I_{\text{SEM}}, E_{\text{SEM}}$$

and the statistical error by:

$$stat = \sqrt{\sum_i \left(\frac{\partial \epsilon}{\partial x_i} \Delta x_i\right)^2} \quad \text{for} \quad x_i = I_{\text{Diode}}, I_{\text{Leak}}, I_{\text{SEM}}, E_{\text{SEM}}$$

The values for the uncertainties of the parameters is given in table B.1.

Table B.1.: Uncertainties on the parameters for the diode efficiency. The systematic uncertainty of the currents depends on the value of the current [50].

Parameter	Δ_{stat}	Δ_{sys}
I_{Diode}	1 %	2 to 20×10^3 pA + 1 to 0.1 %
I_{Leak}	2 pA	2 to 20×10^3 pA + 1 to 0.1 %
I_{SEM}	0.5 pA	2 to 20×10^3 pA + 1 to 0.1 %
E_{SEM}	1 eV[47]	1 %[47]

C. Epitaxy Wafer Layout

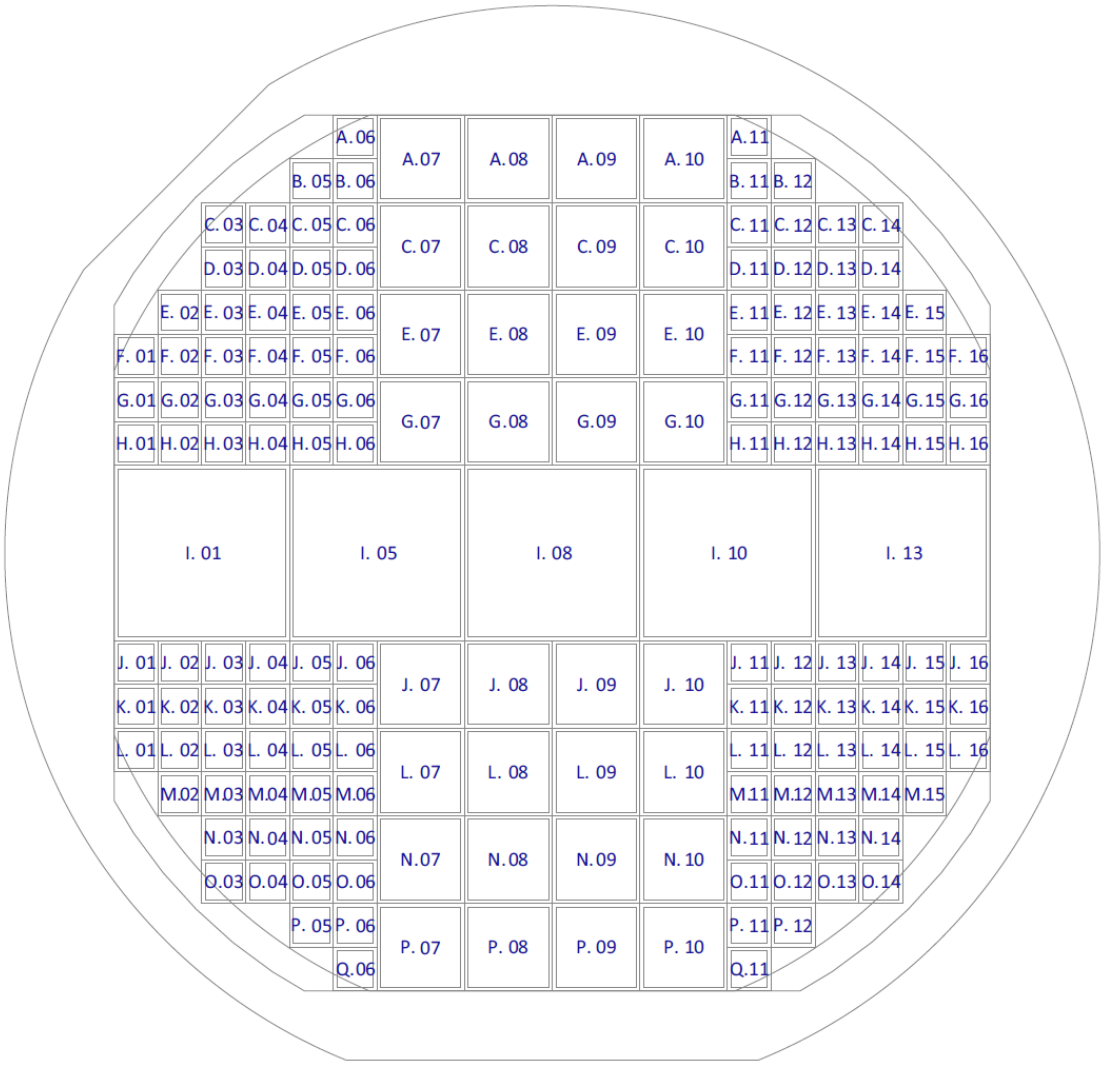

Figure C.1.: The layout of diodes on the wafers for the production of MBE and ion implanted diodes. The layout was the same on all twelve wavers.

Diode	Area [cm^2]	Technique	Diode	Area [cm^2]	Technique
A 07	1.0	Epitaxy	I 10	5.0	Epitaxy-COV
A 08	1.0	Epitaxy-COV	I 13	5.0	Standard thin
A 09	1.0	Epitaxy-COV	J 03	0.1	Epitaxy-COV
A 10	1.0	Standard thin	J 04	0.1	Epitaxy-COV
C 03	0.1	Epitaxy-COV	J 05	0.1	Epitaxy-COV
C 04	0.1	Epitaxy-COV	J 06	0.1	Epitaxy-COV
C 05	0.1	Epitaxy	J 07	1.0	Standard thin
C 06	0.1	Epitaxy	J 08	1.0	Epitaxy-COV
C 07	1.0	Epitaxy-COV	J 09	1.0	Epitaxy-COV
C 08	1.0	Epitaxy-COV	J 10	1.0	Epitaxy
C 09	1.0	Epitaxy-COV	J 11	0.1	Epitaxy-COV
C 10	1.0	Standard thin	J 12	0.1	Epitaxy-COV
C 11	0.1	Epitaxy-COV	J 13	0.1	Epitaxy
C 12	0.1	Epitaxy-COV	J 14	0.1	Epitaxy
C 13	0.1	Epitaxy-COV	K 03	0.1	Epitaxy-COV
C 14	0.1	Epitaxy-COV	K 04	0.1	Epitaxy-COV
D 03	0.1	Epitaxy-COV	K 05	0.1	Epitaxy-COV
D 04	0.1	Epitaxy-COV	K 06	0.1	Epitaxy-COV
D 05	0.1	Epitaxy	K 11	0.1	Epitaxy-COV
D 06	0.1	Epitaxy	K 12	0.1	Epitaxy-COV
D 11	0.1	Epitaxy-COV	K 13	0.1	Epitaxy
D 12	0.1	Epitaxy-COV	K 14	0.1	Epitaxy
D 13	0.1	Epitaxy-COV	L 03	0.1	Standard thick-COV
D 14	0.1	Epitaxy-COV	L 04	0.1	Standard thick-COV
E 03	0.1	Standard thick-COV	L 05	0.1	Standard thick-COV
E 04	0.1	Standard thick-COV	L 06	0.1	Standard thick-COV
E 05	0.1	Standard thick	L 07	1.0	Standard thin
E 06	0.1	Standard thick	L 08	1.0	Epitaxy-COV
E 07	1.0	Standard thick	L 09	1.0	Epitaxy-COV
E 08	1.0	Standard thick-COV	L 10	1.0	Epitaxy-COV
E 09	1.0	Standard thick-COV	L 11	0.1	Standard thick-COV
E 10	1.0	Standard thin	L 12	0.1	Standard thick-COV
E 11	0.1	Standard thick-COV	L 13	0.1	Standard thick
E 12	0.1	Standard thick-COV	L 14	0.1	Standard thick
E 13	0.1	Standard thick-COV	M 03	0.1	Standard thick-COV
E 14	0.1	Standard thick-COV	M 04	0.1	Standard thick-COV

F 03	0.1	Standard thick-COV	**M 05**	0.1	Standard thick-COV
F 04	0.1	Standard thick-COV	**M 06**	0.1	Standard thick-COV
F 05	0.1	Standard thick	**M 11**	0.1	Standard thick-COV
F 06	0.1	Standard thick	**M 12**	0.1	Standard thick-COV
F 11	0.1	Standard thick-COV	**M 13**	0.1	Standard thick
F 12	0.1	Standard thick-COV	**M 14**	0.1	Standard thick
F 13	0.1	Standard thick-COV	**N 03**	0.1	Standard thin
F 14	0.1	Standard thick-COV	**N 04**	0.1	Standard thin
G 03	0.1	Standard thin	**N 05**	0.1	Standard thin
G 04	0.1	Standard thin	**N 06**	0.1	Standard thin
G 05	0.1	Standard thin	**N 07**	1.0	Standard thin
G 06	0.1	Standard thin	**N 08**	1.0	Standard thick-COV
G 07	1.0	Standard thick-COV	**N 09**	1.0	Standard thick-COV
G 08	1.0	Standard thick-COV	**N 10**	1.0	Standard thick
G 09	1.0	Standard thick-COV	**N 11**	0.1	Standard thin
G 10	1.0	Standard thin	**N 12**	0.1	Standard thin
G 11	0.1	Standard thin	**N 13**	0.1	Standard thin
G 12	0.1	Standard thin	**N 14**	0.1	Standard thin
G 13	0.1	Standard thin	**O 03**	0.1	Standard thin
G 14	0.1	Standard thin	**O 04**	0.1	Standard thin
H 03	0.1	Standard thin	**O 05**	0.1	Standard thin
H 04	0.1	Standard thin	**O 06**	0.1	Standard thin
H 05	0.1	Standard thin	**O 11**	0.1	Standard thin
H 06	0.1	Standard thin	**O 12**	0.1	Standard thin
H 11	0.1	Standard thin	**O 13**	0.1	Standard thin
H 12	0.1	Standard thin	**O 14**	0.1	Standard thin
H 13	0.1	Standard thin	**P 07**	1.0	Standard thin
H 14	0.1	Standard thin	**P 08**	1.0	Standard thick-COV
I 01	5.0	Standard thick-COV	**P 09**	1.0	Standard thick-COV
I 05	5.0	Standard thick-COV	**P 10**	1.0	Standard thick-COV
I 08	5.0	Epitaxy-COV			

D. Epitaxy Results

Table D.1.: Results for wafer three.

Diode	Dead Layer position μ [nm]	Spread of Step Function σ [nm]
Epitaxy	2.90 ± 0.03	0.00 ± 0.02
Epitaxy-COV	5.50 ± 0.01	0.00 ± 0.01
Standard thin	107 ± 28	141 ± 46
Standard thick	47	0

Table D.2.: Results for wafer Seven.

Diode	Dead Layer position μ [nm]	Spread of Step Function σ [nm]
Epitaxy	5.4 ± 0.1	0.1 ± 0.1
Epitaxy-COV	9.02 ± 0.02	0.00 ± 0.01
Standard thin	93 ± 19	121 ± 33
Standard thick	45	0

Table D.3.: Results for wafer Twelve.

Diode	Dead Layer position μ [nm]	Spread of Step Function σ [nm]
Epitaxy	3.7 ± 0.6	0 ± 1
Epitaxy-COV	2.0 ± 0.5	0.00 ± 0.01
Standard thin	46 ± 8	96 ± 28
Standard thick	29	0

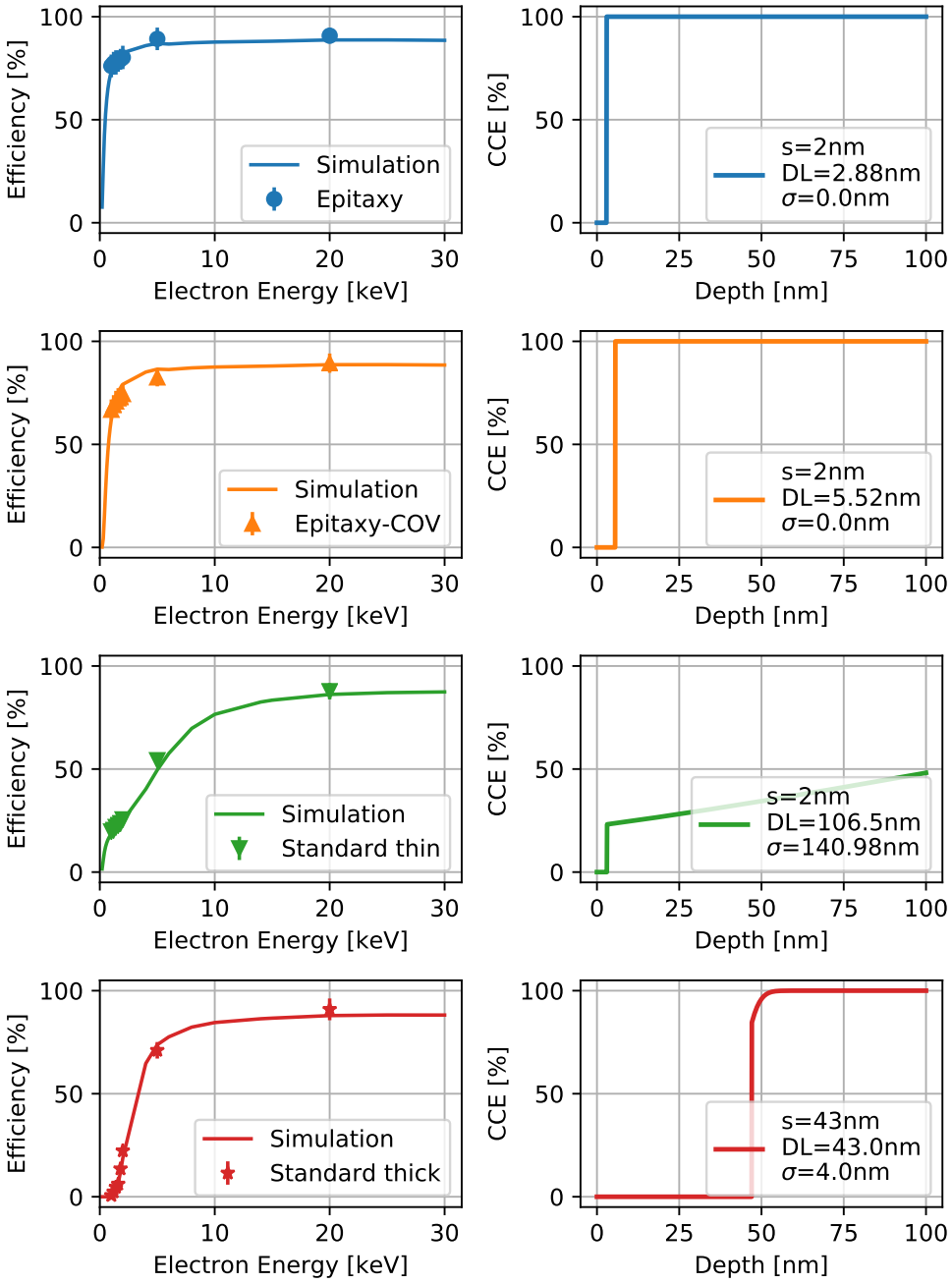

Figure D.1.: Charge collection efficiency and simulation results for wafer three.

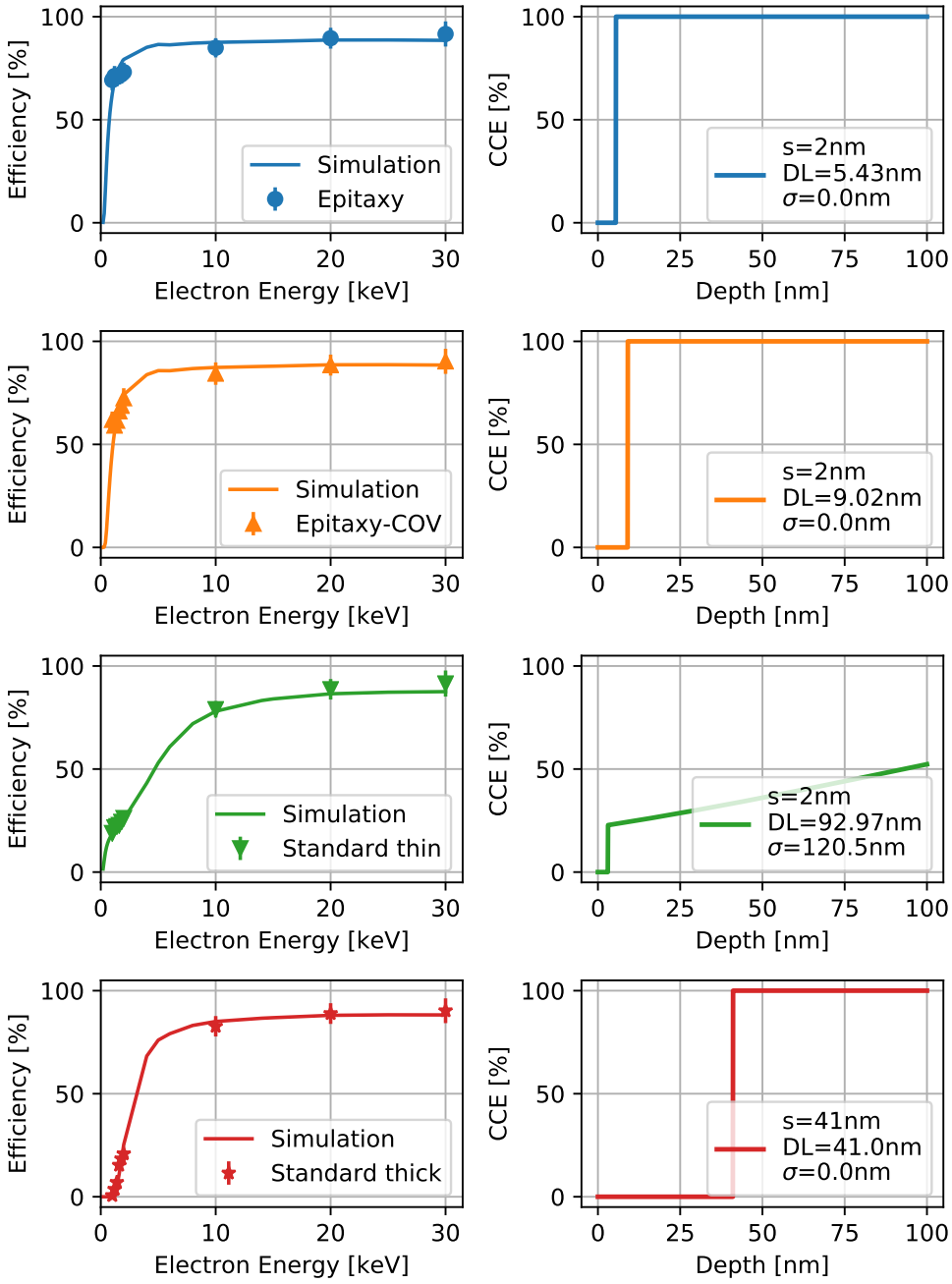

Figure D.2.: Charge collection efficiency and simulation results for wafer seven.

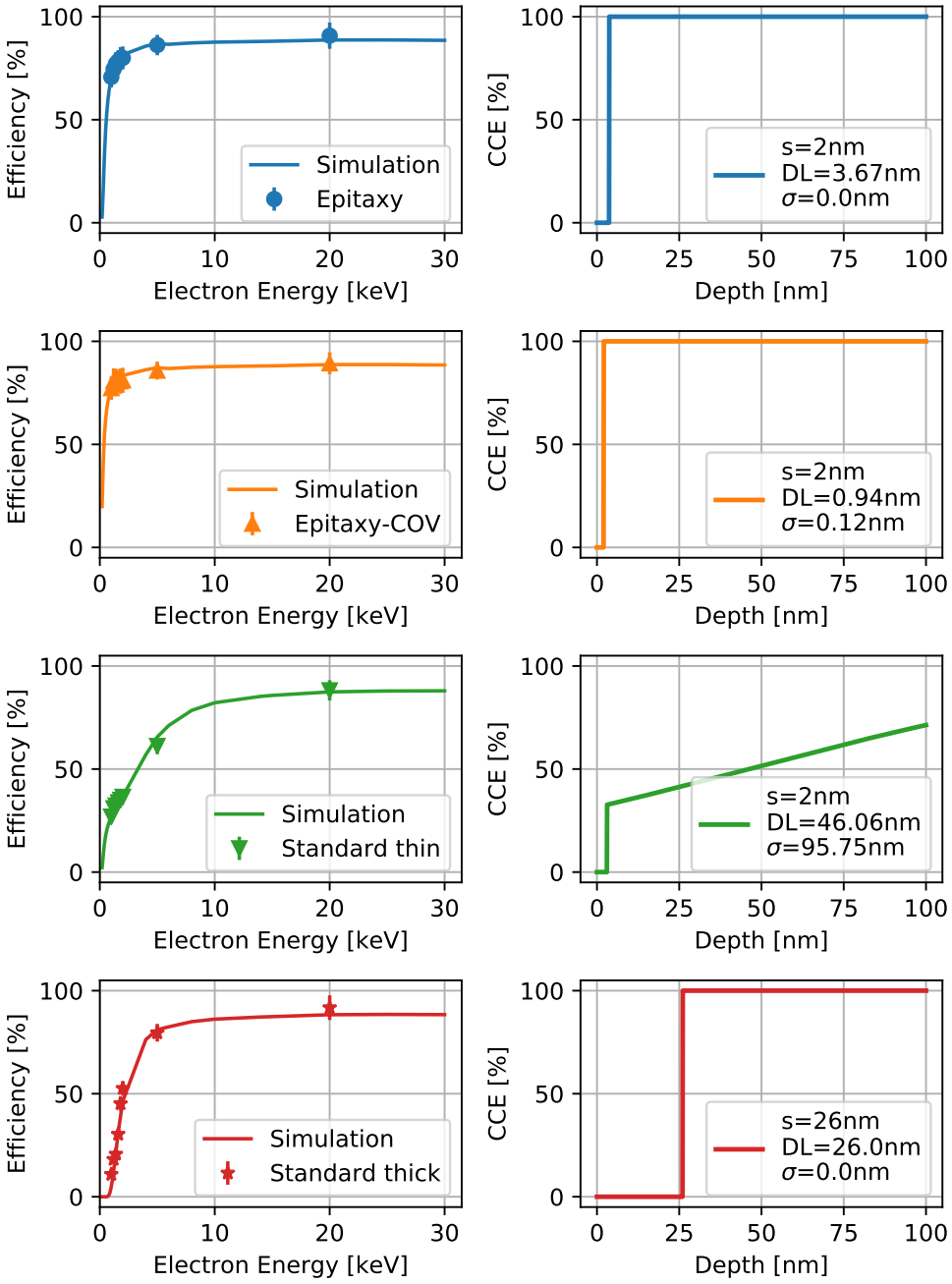

Figure D.3.: Charge collection efficiency and simulation results for wafer twelve.

E. Proton Grid

The proton grid is a small proton accelerator that was designed to analyze the dead layer of the TRISTAN detectors. Protons are much heavier than electrons and thus have a much smaller mean free path. So they would lose a much bigger fraction of their energy in a dead layer than electrons do, which would increase the energy shift between a tilted and an untilted measurement. Protons with negligible kinetic energy should be accelerated up to 30 keV and hit a detector mounted tiltable on the other end of the grid. The feasibility of the characterization of SDDs using a proton grid was shown in [20].

E.1. Setup

The setup of the proton grid is shown in figure E.1. It is 44 cm long and consists of 51 stainless steel disks each 1 mm thick. Each disk has a hole with a diameter of 14 mm in the center for the protons to fly through and a distance of 8 mm to the next disk. A connection between the disks is established through a resistor of 1 GΩ. High voltages of up to 30 keV are applied to the lowest disk, while the top plate is grounded, because of the high ohmic resistors only a small current in the order of mA is flowing through the system. To reduce the possibility of interferences between the high voltage and the detector, the detector is mounted on the grounded top plate. This plate is also tiltable up to 20° to enable measurements at different

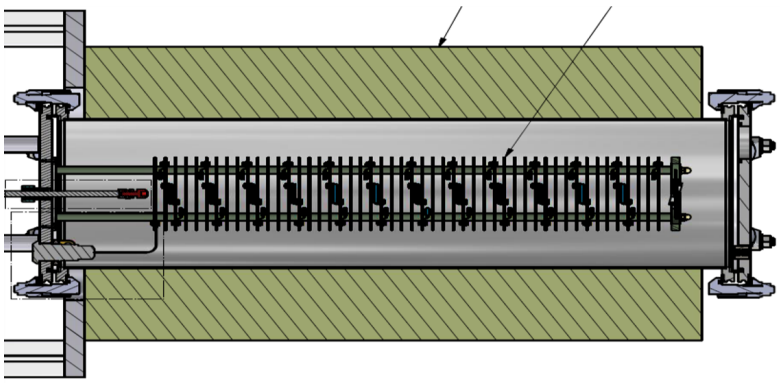

Figure E.1.: Design of the proton grid setup.

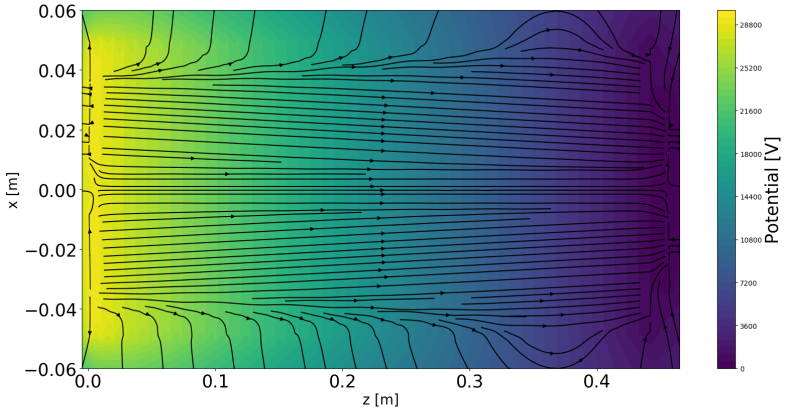

Figure E.2.: Simulation of the electric field inside the proton grid vacuum chamber.

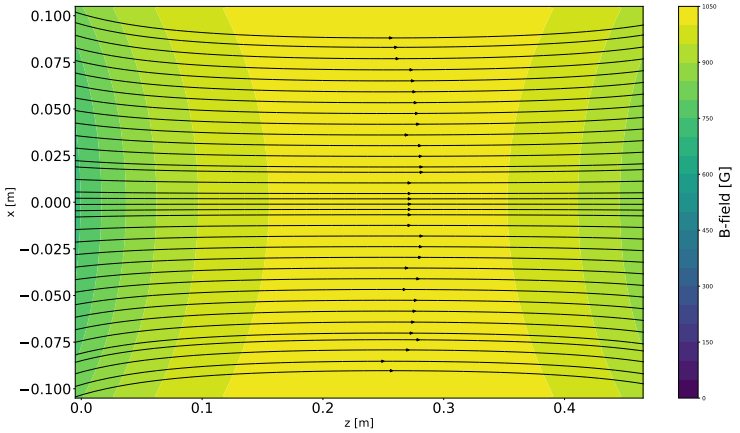

Figure E.3.: Simulation of the magnetic field inside the proton grid vacuum chamber.

angles. The proton source is located below the first disk. If a potential difference is applied to the plates, they create a homogeneous field between them and a convex field in the region of the holes, this can be seen in figure E.2. This field accelerates the protons towards the detector. In air the protons would be stopped within a few cm. Therefore, the whole grid is put inside a vacuum chamber. Around the chamber a magnetic coil is wound to create a magnetic field of 200 mT, which field lines are parallel to the ones of the electric field, as can be seen in figure E.3. If the momentum of a proton is not parallel to the field lines, the Lorentz force creates a cyclotron motion around the field lines. Therefore, fewer protons fly off course which would then be lost for the measurement.

The proton source consists of a open ^{241}Am radioactive source and a foil of stretched polyethylene terephthalate (PET) that is on top of the ^{241}Am. In the decay of ^{241}Am protons of about 5.4 MeV are created. The energy of those are too

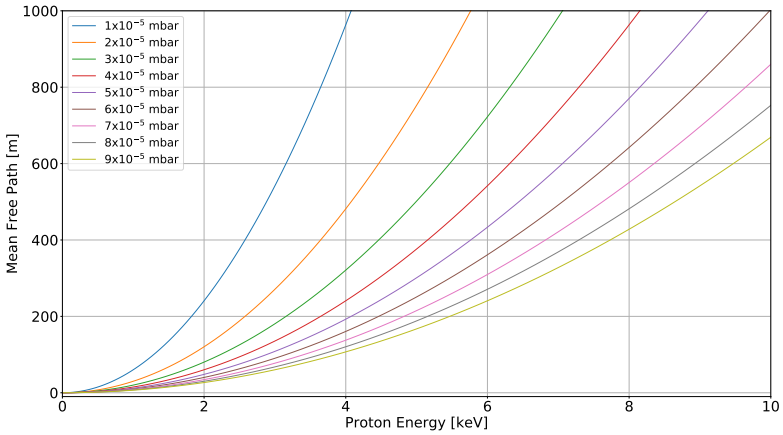

Figure E.4.: Calculation of the mean free path of protons in air at low pressures. The calculation was done using the Rutherford scattering probability on oxygen and nitrogen.

high to use them for characterization because by entering in the detector they would create so many charge carriers that it would saturate the detector instantly. These high energetic electrons are used to "kick-out" weakly bound hydrogen cores inside the PET.

E.2. Complications

During testing of the proton grid several complications occurred.

Vacuum: In order for protons to have a mean free path that is much longer than the length of the grid even for low energies the vacuum has to have a pressure below 10^{-4} mbar, see figure E.4. Otherwise low energy protons scatter on the residual gas and can then be lost for the measurement. In the empty chamber a vacuum of around 5×10^{-6} mbar was achievable with the turbomolecular pumps. However, with the proton grid inside the lowest pressure was 8×10^{-5} mbar after approximately 7 d of pumping. This is due to outgassing of the materials. One major contribution is the outgassing of the resistors, which already increased the achievable pressure by one order of magnitude.

Electric Field: The electric field is the main component of the proton grid. Applying voltages of up to 15 kV with a pressure of around 5×10^{-4} mbar was unproblematic. Above this flashovers occurred somewhere on the grid, it is not exactly known where they happen. These happened randomly and, at voltages

above 20 kV, damage the high voltage supply. For this reason only measurements with proton energies of up to 20 keV are feasible.

Magnetic Field: The design value of the magnetic field strength in the center of the coil is 200 mT. The real value the magnetic coil can create is only 86 mT. Given that the coil is not cooled, it is heating up to 80 °C in continuous operation. This also heats the proton grid inside, which increases outgassing and also could damage the resistors over a long period of time.

Another problem is the combined operation of high voltage and magnetic field. By applying a magnetic field, the flashovers of the high voltage happen already at a few kV. This could either be caused by penning traps that appear in the grid or because the ions of the residual gas are also guided by the magnetic field towards the grid disks. Because of the much lower magnetic field strength, no measurement was performed with a magnetic field.

Measurements: Several measurements were performed to test the functionality of the proton grid. One with ^{55}Fe, which is a photon emitter, with a proton source, and background measurements. The iron source was placed directly below the detector and no high voltage was applied to the grid. With this setup it was confirmed that the detector mounted on the grid was working properly. For the proton and background measurements the vacuum chamber was evacuated and voltages of 8, 10 and 20 kV were applied. The expected proton energies measured in the detector are around 3, 4 and 9 keV [20]. No difference between the background measurement and the one with a proton source were visible. This is most likely due to a loss of protons on the way because the guiding magnetic field was not operational.

E.3. Conclusion

A proton grid is a viable possibility to characterize the dead layer of a SDD [20]. The proton grid built for this experiment, however is not working as intended. For this reason the investigations with protons was discontinued. Reasons for the problems might be the size of the grid, which allows protons on a long way to be lost. The length also increases the size of the vacuum chamber and the magnetic coil. The large size of the chamber makes low vacuum pressures harder to establish. It is also more difficult to create a magnetic field in a larger volume. Therefore, an overall smaller design is favorable in terms of vacuum and magnetic field.

List of Figures

List of Tables

Bibliography

[1] T. Åberg and S. Flügge. *Korpuskeln und Strahlung in Materie 1.* Vol. = Encyclopedia of physics / hrsg. von S. Flügge ; Bd. 31. Handbuch der Physik. Berlin: Springer, 1982. ISBN: 0387113134.

[2] R. Adam, P. A. R. Ade, N. Aghanim, et al. "Planck 2015 results". In: *Astronomy & Astrophysics* 594 (2016), A1. ISSN: 0004-6361. DOI: \url{10.1051/0004-6361/201527101}.

[3] R. Adhikari, M. Agostini, N. A. Ky, et al. "A White Paper on keV Sterile Neutrino Dark Matter". In: *Journal of Cosmology and Astroparticle Physics* 2017.01 (2017), p. 025. ISSN: 1475-7516. DOI: \url{10.1088/1475-7516/2017/01/025}. URL: %5Curl%7Bhttp://arxiv.org/pdf/1602.04816v2%7D.

[4] N. Aghanim, Y. Akrami, M. Ashdown, et al. *Planck 2018 results. VI. Cosmological parameters.* 2018. arXiv: 1807.06209 [astro-ph.CO].

[5] M. Agostini, A. M. Bakalyarov, M. Balata, et al. "Improved Limit on Neutrinoless Double-β Decay of ^{76}Ge from GERDA Phase II". In: *Phys. Rev. Lett.* 120 (13 Mar. 2018), p. 132503. DOI: 10.1103/PhysRevLett.120.132503. URL: https://link.aps.org/doi/10.1103/PhysRevLett.120.132503.

[6] Q. R. Ahmad, R. C. Allen, T. C. Andersen, et al. "Direct Evidence for Neutrino Flavor Transformation from Neutral-Current Interactions in the Sudbury Neutrino Observatory". In: *Phys. Rev. Lett.* 89 (1 June 2002), p. 011301. DOI: 10.1103/PhysRevLett.89.011301. URL: https://link.aps.org/doi/10.1103/PhysRevLett.89.011301.

[7] M. Aker, K. Altenmüller, M. Arenz, et al. *Improved Upper Limit on the Neutrino Mass from a Direct Kinematic Method by KATRIN.* Nov. 2019. DOI: 10.1103/PhysRevLett.123.221802. URL: https://link.aps.org/doi/10.1103/PhysRevLett.123.221802.

[8] J. Allison, K. Amako, J. Apostolakis, et al. "Recent developments in Geant4". In: *Nuclear Instruments and Methods in Physics Research Section A: Accelerators, Spectrometers, Detectors and Associated Equipment* 835 (2016), pp. 186–225. ISSN: 0168-9002. DOI: 10.1016/j.nima.2016.06.125. URL: http://www.sciencedirect.com/science/article/pii/S0168900216306957.

[9] V. N. Aseev, A. I. Belesev, A. I. Berlev, et al. "Upper limit on the electron antineutrino mass from the Troitsk experiment". In: *Phys. Rev. D* 84 (11 Dec. 2011), p. 112003. DOI: 10.1103/PhysRevD.84.112003. URL: https://link.aps.org/doi/10.1103/PhysRevD.84.112003.

[10] M. Babutzka. "Design and development for the Rearsection of the KATRIN experiment". Karlsruhe, Karlsruher Institut für Technologie (KIT), Diss., 2014. Karlsruhe: Karlsruher Institut für Technologie, 2014. URL: %5Curl%7Bhttp://digbib.ubka.uni-karlsruhe.de/volltexte/1000045598%7D.

[11] B. Beckhoff. *Handbook of practical x-ray fluorescence analysis*. Berlin Heidelberg: Springer-Verlag GmbH, 2006. ISBN: 3-540-28603-9. DOI: 10.1007/978-3-540-36722-2. URL: http://site.ebrary.com/lib/alltitles/docDetail.action?docID=10176801.

[12] L. Bombelli, C. Fiorini, T. Frizzi, et al. ""CUBE", A low-noise CMOS preamplifier as alternative to JFET front-end for high-count rate spectroscopy". In: *2011 IEEE Nuclear Science Symposium Conference Record*. 2011, pp. 1972–1975. DOI: 10.1109/NSSMIC.2011.6154396.

[13] A. Boyarsky, O. Ruchayskiy, D. Iakubovskyi, et al. "An unidentified line in X-ray spectra of the Andromeda galaxy and Perseus galaxy cluster". In: *Physical Review Letters* 113.25 (2014). ISSN: 0031-9007. DOI: \url{10.1103/PhysRevLett.113.251301}. URL: %5Curl%7Bhttp://arxiv.org/pdf/1402.4119v2%7D.

[14] L. W. Bruch, R. D. Diehl, and J. A. Venables. "Progress in the measurement and modeling of physisorbed layers". In: *Rev. Mod. Phys.* 79.4 (2007), pp. 1381–1454. DOI: 10.1103/RevModPhys.79.1381. URL: %5Curl%7Bhttps://link.aps.org/doi/10.1103/RevModPhys.79.1381%7D.

[15] Z. Chacko, A. Dev, P. Du, et al. *Cosmological Limits on the Neutrino Mass and Lifetime*. 2019. arXiv: 1909.05275 [hep-ph].

[16] T. Eggert. "Die spektrale Antwort von Silizium-Röntgendetektoren". PhD thesis. München: Technische Universität München, 2004.

[17] P. Frigeri, L. Seravalli, G. Trevisi, et al. "3.12 - Molecular Beam Epitaxy: An Overview". In: *Comprehensive semiconductor science and technology*. Ed. by P. Bhattacharya, R. Fornari, and H. Kamimura. Amsterdam: Elsevier Science, 2011, pp. 480–522. ISBN: 978-0-444-53153-7. DOI: 10.1016/B978-0-44-453153-7.00099-7. URL: http://www.sciencedirect.com/science/article/pii/B9780444531537000997.

[18] Y. Fukuda, T. Hayakawa, E. Ichihara, et al. "Evidence for Oscillation of Atmospheric Neutrinos". In: *Phys. Rev. Lett.* 81 (8 Aug. 1998), pp. 1562–1567. DOI: 10.1103/PhysRevLett.81.1562. URL: https://link.aps.org/doi/10.1103/PhysRevLett.81.1562.

[19] S. N. Gninenko, D. S. Gorbunov, and M. E. Shaposhnikov. *Search for GeV-scale sterile neutrinos responsible for active neutrino oscillations and baryon asymmetry of the Universe*. 2013. URL: %5Curl%7Bhttp://arxiv.org/pdf/1301.5516v1%7D.

[20] D. Greenwald. "Characterization of the Proton Source in the Frictional Cooling Demonstration experiment". MA thesis. Technische Universität München, 2007.

[21] F. Hartmann. *Evolution of Silicon Sensor Technology in Particle Physics*. Second edition. Vol. 275. Springer Tracts in Modern Physics. Cham: Springer, 2017. ISBN: 9783319644349. DOI: 10.1007/978-3-319-64436-3.

[22] J. L. Hudgins. "Wide and narrow bandgap semiconductors for power electronics: A new valuation". In: *Journal of Electronic Materials* 32.6 (June 2003), pp. 471–477. ISSN: 1543-186X. DOI: 10.1007/s11664-003-0128-9. URL: https://doi.org/10.1007/s11664-003-0128-9.

[23] JEOL (Germany) GmbH. Last accessed: 06.11.2019. Gute Änger 30, 85256 Freising, Germany. URL: https://www.jeol.de/.

[24] S. Kasap. *PN Junction the Shockley model*. electronic. 2001.

[25] KATRIN Collaboration. *KATRIN design report 2004*. Tech. rep. 51.54.01; LK 01. Forschungszentrum, Karlsruhe, 2005. 245 pp. DOI: 10.5445/IR/270060419.

[26] J. Kemmer, F. Wiest, A. Pahlke, et al. "Epitaxy — a new technology for fabrication of advanced silicon radiation detectors". In: *Nuclear Instruments and Methods in Physics Research Section A: Accelerators, Spectrometers, Detectors and Associated Equipment* 544.3 (2005), pp. 612–619. ISSN: 0168-9002. DOI: \url{10.1016/j.nima.2005.02.013}.

[27] M. Korzeczek. "eV- & keV-sterile neutrino studies with KATRIN". MA thesis. Karlsruhe Institut für Technologie, 2016.

[28] C. Kraus, B. Bornschein, L. Bornschein, et al. "Final results from phase II of the Mainz neutrino mass searchin tritium β-decay". In: *The European Physical Journal C - Particles and Fields* 40.4 (Apr. 2005), pp. 447–468. ISSN: 1434-6052. DOI: 10.1140/epjc/s2005-02139-7. URL: https://doi.org/10.1140/epjc/s2005-02139-7.

[29] P. Lechner, C. Fiorini, R. Hartmann, et al. “Silicon drift detectors for high count rate X-ray spectroscopy at room temperature”. In: *Nuclear Instruments and Methods in Physics Research Section A: Accelerators, Spectrometers, Detectors and Associated Equipment* 458.1 (2001), pp. 281–287. ISSN: 0168-9002. DOI: {10.1016/S0168-9002(00)00872-X}. URL: %5Curl%7Bhttp://www.sciencedirect.com/science/article/pii/S016890020000872X%7D.

[30] P. Lechner. personal communication. Feb. 26, 2019.

[31] P. Lechner. “Zur Ionisationsstatistik in Silicium”. PhD thesis. Technische Universität München, 1998.

[32] M. C. Lépy, B. Duchemin, and J. Morel. “Comparison of experimental and theoretical L X — ray emission probabilities of 241Am, 239Pu and 240Pu”. In: *Nuclear Instruments and Methods in Physics Research Section A: Accelerators, Spectrometers, Detectors and Associated Equipment* 353.1 (1994), pp. 10–15. ISSN: 0168-9002. DOI: 10.1016/0168-9002(94)91591-1. URL: http://www.sciencedirect.com/science/article/pii/0168900294915911.

[33] J. W. Mayer. “Ion implantation in semiconductors”. In: *1973 International Electron Devices Meeting*. Dec. 1973, pp. 3–5. DOI: 10.1109/IEDM.1973.188633.

[34] S. Mertens, T. Lasserre, S. Groh, et al. “Sensitivity of Next-Generation Tritium Beta-Decay Experiments for keV-Scale Sterile Neutrinos”. In: *Journal of Cosmology and Astroparticle Physics* 2015.02 (2015), p. 020. ISSN: 1475-7516. DOI: \url{10.1088/1475-7516/2015/02/020}. URL: %5Curl%7Bhttp://arxiv.org/pdf/1409.0920v2%7D.

[35] S. Mertens, A. Alborini, K. Altenmüller, et al. “A novel detector system for KATRIN to search for keV-scale sterile neutrinos”. In: *Journal of Physics G: Nuclear and Particle Physics* 46.6 (2019), p. 065203. ISSN: 1367-2630. DOI: 10.1088/1361-6471/ab12fe.

[36] B. Ostrick. “Eine kondensierte 83m Kr-Kalibrationsquelle für das KATRIN-Experiment”. PhD thesis. 2008. URL: https://books.google.de/books?id=aAbnvgEACAAJ.

[37] F. Perotti and C. Fiorini. *Observed energy dependence of Fano factor in silicon at hard X-ray energies*. Elsevier B.V, 1999.

[38] A. Picard, H. Backe, J. Bonn, et al. “Precision measurement of the conversion electron spectrum of83mKr with a solenoid retarding spectrometer”. In: *Zeitschrift für Physik A Hadrons and Nuclei* 342.1 (1992), pp. 71–78. ISSN: 0939-7922. DOI: 10.1007/BF01294491.

[39] U. W. Pohl. *Epitaxy of Semiconductors: Introduction to Physical Principles*. Graduate Texts in Physics. Berlin and Heidelberg: Springer, 2013. ISBN: 9783642329692. DOI: 10.1007/978-3-642-32970-8. URL: http://gbv.eblib.com/patron/FullRecord.aspx?p=1082626.

[40] M. Popp. "Untersuchung und analytische Modellierung der Systemantwort von pn-CCD Detektoren". PhD thesis. 2000. URL: http://nbn-resolving.de/urn:nbn:de:bvb:19-4087.

[41] A. J. Ptak. "Principles of Molecular Beam Epitaxy". In: *Handbook of Crystal Growth*. Elsevier, 2015, pp. 161–192. ISBN: 9780444633040. DOI: 10.1016/B978-0-444-63304-0.00004-4.

[42] P. Rehak, E. Gatti, A. Longoni, et al. "Semiconductor drift chambers for position and energy measurements". In: *Nuclear Instruments and Methods in Physics Research Section A: Accelerators, Spectrometers, Detectors and Associated Equipment* 235.2 (1985), pp. 224–234. ISSN: 0168-9002. DOI: 10.1016/0168-9002(85)90557-1. URL: %5Curl%7Bhttp://www.sciencedirect.com/science/article/pii/0168900285905571%7D.

[43] P. Renschler. "KESS - A new Monte Carlo simulation code for low-energy electron interactions in silicon detectors". Karlsruhe, Karlsruher Institut für Technologie (KIT), Diss., 2011. Karlsruhe: KIT-Bibliothek, 2011. URL: http://digbib.ubka.uni-karlsruhe.de/volltexte/1000024959.

[44] R. Richter. personal communication. Nov. 12, 2019.

[45] S. Seltzer. *Tables of X-Ray Mass Attenuation Coefficients and Mass Energy-Absorption Coefficients, NIST Standard Reference Database 126*. 1995. DOI: 10.18434/T4D01F.

[46] D. Siegmann. Internal Documents of the TRISTAN Group. 2019.

[47] D. Siegmann. "Investigation of the Detector Response to Electrons of the TRISTAN Prototype Detectors". MA thesis. Technische Universität München, 2019.

[48] M. Slezák. Internal material of the KATRIN Group. 2019.

[49] H. Spieler. *Semiconductor detector systems*. Reprint. (twice). Vol. 12. Oxford science publications. Oxford: Oxford Univ. Press, 2009. ISBN: 9780198527848.

[50] Tektronix, Inc. *Manual*. URL: https://de.tek.com/keithley-low-level-sensitive-and-specialty-instruments/keithley-series-6400-picoammeters. last visited: 27.10.2019.

[51] F. Tuinstra and J. Lo Koenig. "Raman spectrum of graphite". In: *The Journal of Chemical Physics* 53.3 (1970), pp. 1126–1130.

[52] K. Urban. "Application of a TRISTAN Silicon Drift Detector as FBM in KATRIN". MA thesis. Technische Universität München, 2019. unpublished thesis.

[53] D. Vénos, J. Sentkerestiová, O. Dragoun, et al. "Properties of 83 mKr conversion electrons and their use in the KATRIN experiment". In: *Journal of Physics G: Nuclear and Particle Physics* 13.02 (2018), T02012–T02012. ISSN: 1367-2630. DOI: 10.1088/1748-0221/13/02/T02012.

[54] P. Virtanen, R. Gommers, T. E. Oliphant, et al. *SciPy 1.0–Fundamental Algorithms for Scientific Computing in Python*. URL: http://arxiv.org/pdf/1907.10121v1.

[55] XGLab S.R.L. Via Conte Rosso 23, I-20134 Milano (Italy).

[56] A. A. Yaroshevsky. "Abundances of chemical elements in the Earth's crust". In: *Geochemistry International* 44.1 (2006), pp. 48–55. ISSN: 0016-7029. DOI: 10.1134/S001670290601006X.

[57] M. Zbořil, S. Bauer, M. Beck, et al. "Ultra-stable implanted 83 Rb/ 83 m Kr electron sources for the energy scale monitoring in the KATRIN experiment". In: *Journal of Physics G: Nuclear and Particle Physics* 8.03 (2013), P03009–P03009. ISSN: 1367-2630. DOI: 10.1088/1748-0221/8/03/P03009.

[58] M. Zbořil. "Feste Elektronenquellen für die Energieskalaüberwachung im KATRIN-Experiment". Münster, Westfälische Wilhelms-Universität Münster, Diss., 2012. Münster: Universitäts- und Landesbibliothek der Westfälischen Wilhelms-Universität, 2012.

Acknowledgments

This work would not have been possible without the help and support of many people. I want to especially thank:

- Prof. Dr. Susanne Mertens for giving me the opportunity to write this thesis in her working group. I learned a lot in the past year.
- Tim Brunst for helping me with all my questions and problems that I had
- Thibaut Houdy for answering me patiently all the questions I had for him
- Matthias Maier for performing the Geant4 simulations need for my analysis
- Daniel Siegmann for helping me with the measurements and also the KESS simulations
- Florian Schopper and Peter Lechner at the HLL for providing the more than interesting epitaxy investigations
- Korbinian Urban und Christoph Köhler for being great office neighbors
- all other members of the working group for the great work environment

And also thank you to all my friends, without you I would not have enjoyed my years as a student as much as I did.

But the greatest thank you goes to my family who supported and encouraged me on every step of my way. Without you, I would not be here today.

Declaration of Authorship

I hereby declare that this master's thesis in the course Nuclear, Particle, and Astrophysics is my own work and I have documented all sources and material used.

Ich versichere, dass ich diese Masterarbeit im Fach Kern-, Teilchen-, und Astrophysik selbstständig verfasst und nur die angegebenen Quellen und Hilfsmittel verwendet habe.

Munich, 02.12.2019 Manuel Lebert